Shock and Vibration

International Conference on Advances in Mechanical Engineering and Mechanics 2010

Guest Editor: Sami El-Borgi

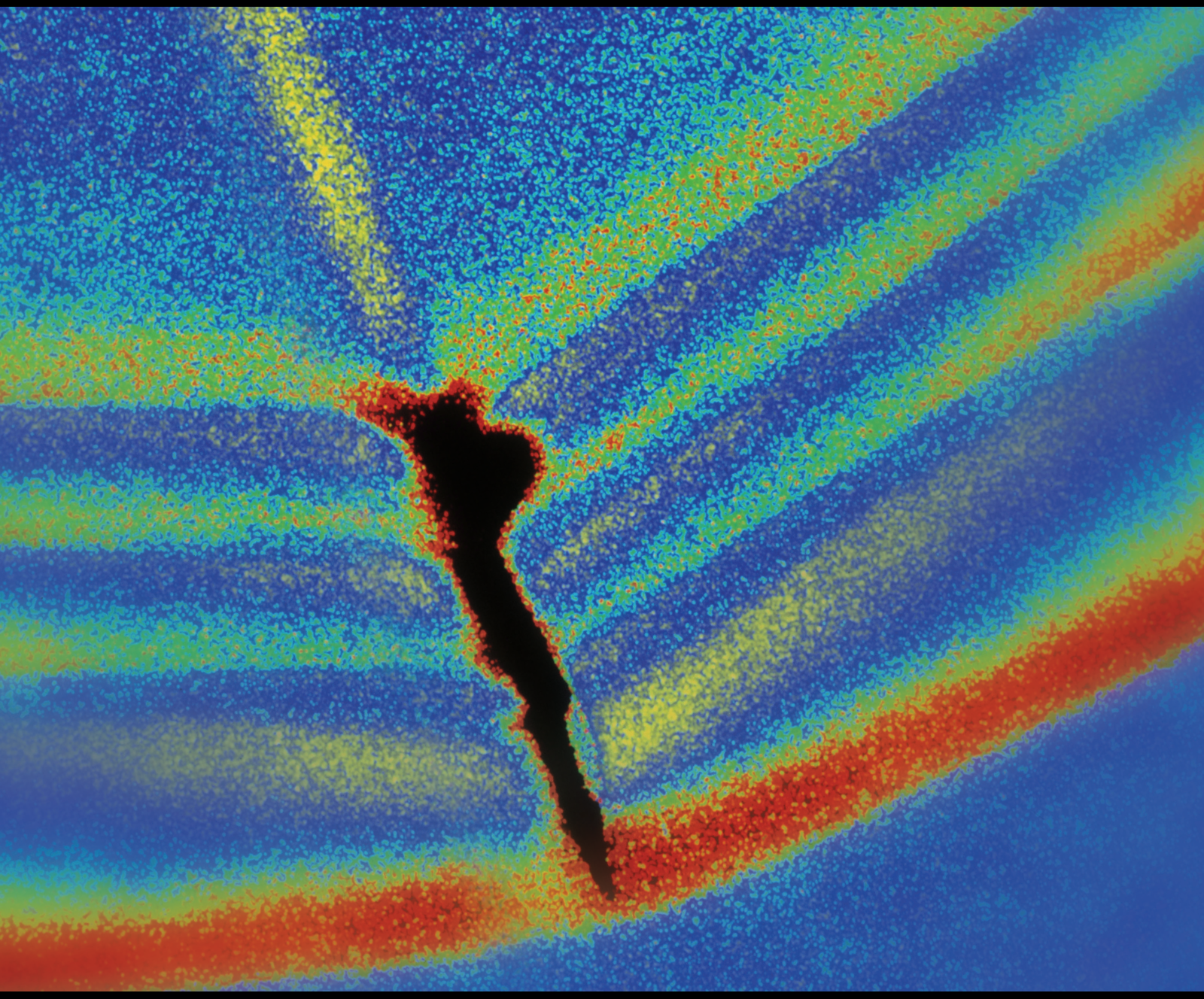

International Conference on Advances in Mechanical Engineering and Mechanics 2010

Shock and Vibration

International Conference on Advances in Mechanical Engineering and Mechanics 2010

Guest Editors: Sami El-Borgi

Contents

Hindawi Publishing Corporation
Shock and Vibration
Volume 2014, Article ID 857385, 2 pages
http://dx.doi.org/10.1155/2014/857385

Editorial

International Conference on Advances in Mechanical Engineering and Mechanics 2010

Sami El-Borgi[1,2]

[1] *Mechanical Engineering Program, Texas A&M University at Qatar, Doha, Qatar*
[2] *Applied Mechanics and Systems Research Laboratory, Tunisia Polytechnic School, University of Carthage, La Marsa, Tunisia*

Correspondence should be addressed to Sami El-Borgi; sami.el_borgi@qatar.tamu.edu

Received 3 October 2013; Accepted 3 October 2013; Published 8 May 2014

The present special issue of Shock and Vibration journal includes six papers presenting studies conducted in various fields of vibration. Papers were selected among those presented at the Fifth International Conference on Advances in Mechanical Engineering and Mechanics 2010 (ICAMEM 2010) held on December 18–20, 2010, in Hammamet, Tunisia. All papers were reviewed by distinguished reviewers according to the journal's procedures and standards. Among the vast number of papers that were presented at the conference, the following studies were selected for this special issue.

Samaali et al. study the response of a capacitive MEMS switch composed of two clamped-clamped flexible microbeams. An electrostatic force is applied between the microbeams to yield the switch to its ON and OFF states. The equations of motion of the system and the associated boundary conditions are derived and the static and dynamic problems are solved using the differential quadratic method. The obtained analytical results are validated using numerical finite element results. The transient behavior of the microswitch was then investigated, indicating a reduction in actuation voltage, switching time, and power consumption while maintaining a relatively good RF performance.

Jemai et al. develop a mathematical model that accurately simulates the dynamic behavior of active fiber composites (AFC). These composites are known for their flexibility and relatively high actuation capacity compared with traditional ceramic piezoelectric materials. The AFC's energy harvesting capabilities, however, are low. The model uses homogenization techniques to describe piezoelectric properties of the AFC. The developed model is incorporated into a vibration-based energy harvesting system consisting on a cantilever beam on top of which an AFC patch is attached. Analytical solutions of the dynamic behavior and the harvested voltage are proposed and validated with finite element simulations.

Gafsi et al. propose a new passive control strategy for the vibration confinement in a flexible nonlinear beam by considering an inverse eigenvalue problem. The strategy consists of determining the geometric parameters of a beam to yield a desired set of mode shapes and natural frequencies. The beam dynamics is described by a nonlinear partial differential equation that is linearized. The authors show that, using the linear model, the strategy of vibration confinement remains valid for the nonlinear beam. They also show that having higher amplitude on a larger frequency interval in conjunction with significant level of vibration confinement on a smaller region of the spatial domain presents an efficient design for energy harvesting.

El Ouni and Ben Kahla investigate numerically the active tendon control of a cable-stayed bridge in a construction phase. A linear finite element model of a small-scale mock-up of the bridge is first developed, coupled with a geometrically nonlinear model for the cable. Active damping is added to the structure by using pairs of collocated force actuator-displacement sensors located on each active cable and controlled by decentralized first order positive position feedback (PPF) or direct velocity feedback (DVF). A decentralized parallel PPF-DVF is proposed to obtain the best performance from the two compensators. The authors show that the proposed strategy can be used to control both deck and cable vibrations induced by parametric excitation.

Jiang et al. propose a methodology for fault diagnosis of rotating machinery based on vibration multisensor

information fusion. Three case studies are used to show the effectiveness of the proposed methodology, namely, diagnostic of faulty gear, rolling bearing, and identification of rotor crack. For each case study, the sensibilities of the features are analyzed. The obtained results indicate that the peak factor is the most sensitive feature for identifying gear defect, among the twelve time-domain features that are considered. The mean, amplitude squared, root mean square, root amplitude, and standard deviation are all suitable for identifying gear, rolling bearing, and rotor crack defect on a comparative basis.

In identifying the modal signature of structures based on output-only measurements, several algorithms have been developed over the years among which is the family of stochastic subspace identification techniques known for their robustness and convergence. For large-scale structures, the selection of the model order and the corresponding system poles is often challenging. To address this problem, the concept of the "stabilization diagram" is introduced. The problem with these diagrams is that the resulting spurious modes need to be eliminated. Mrabet et al. suggest a new stabilization criterion obtained through a novel numerical implementation of the stabilization diagram. The new implementation makes the alignment of the stabilization diagram more robust, so that only the spurious modes are removed. The authors apply the new stabilization diagram and the implemented identification technique to identify the modal signature of an aircraft structure.

Sami El-Borgi

Hindawi Publishing Corporation
Shock and Vibration
Volume 2014, Article ID 971597, 9 pages
http://dx.doi.org/10.1155/2014/971597

Research Article

Mathematical Modeling of an Active-Fiber Composite Energy Harvester with Interdigitated Electrodes

A. Jemai,[1] F. Najar,[1] M. Chafra,[1] and Z. Ounaies[2]

[1] *Applied Mechanics and Systems Research Laboratory, Tunisia Polytechnic School, University of Carthage, BP 743, 2078 La Marsa, Tunisia*
[2] *Department of Mechanical and Nuclear Engineering, The Pennsylvania State University, 157B Hammond Building, University Park, PA 16802, USA*

Correspondence should be addressed to F. Najar; fehmi.najar@gmail.com

Received 27 May 2013; Accepted 21 June 2013; Published 7 May 2014

Academic Editor: Mehdi Ahmadian

The use of active-fiber composites (AFC) instead of traditional ceramic piezoelectric materials is motivated by flexibility and relatively high actuation capacity. Nevertheless, their energy harvesting capabilities remain low. As a first step toward the enhancement of AFC's performances, a mathematical model that accurately simulates the dynamic behavior of the AFC is proposed. In fact, most of the modeling approaches found in the literature for AFC are based on finite element methods. In this work, we use homogenization techniques to mathematically describe piezoelectric properties taking into consideration the composite structure of the AFC. We model the interdigitated electrodes as a series of capacitances and current sources linked in parallel; then we integrate these properties into the structural model of the AFC. The proposed model is incorporated into a vibration based energy harvesting system consisting of a cantilever beam on top of which an AFC patch is attached. Finally, analytical solutions of the dynamic behavior and the harvested voltage are proposed and validated with finite element simulations.

1. Introduction

Recently advances in smart microsensors and microelectronics contributed to the development of devices with reduced size and low energy consumption. This development encouraged researchers to innovate in the field of energy sources in order to overcome the use of batteries. Given that the technological evolutions of batteries were relatively slow during the last decade, use of piezoelectric devices as energy harvesters (EHs) has progressively attracted attention of researchers. Indeed, many studies indicate the feasibility of using piezoelectric materials as power sources at different scales [1–3].

Nevertheless, monolithic piezoelectric materials, and specifically piezoelectric ceramics such as PZT, present several integration difficulties to structures characterized by curved shapes and large displacements [4]. Furthermore, due to the brittle nature of PZT, monolithic energy harvesters cannot take advantage of relatively large stroke vibrations due to their small allowable deformations. Thus, Bent et al. [5] developed a new piezoelectric composite known as active-fiber composite (AFC) which consists of PZT fibers with circular cross-section embedded into an epoxy matrix and sandwiched between two sets of interdigitated electrodes (IDE). A similar one, macrofiber composite (MFC), was also developed at NASA Langley Research Center, where PZT fiber has a square cross-section [6]. These particular designs, and thanks to the IDE, use the higher d_{33} mode for actuators [7] as well as energy harvesters [4].

When used as energy generators, piezocomposites with IDE are still far from fulfilling the power consumption requirements of most portable electronics, at present. In fact, several researches showed limitation for their use for energy harvesting applications [8, 9]. In order to improve the performance of piezocomposites used as EH or actuator, several studies were conducted to redesign AFC and MFC by studying their behavior through simulations. Unfortunately, most of the proposed models are based on FE analysis because

of the complexity of the piezocomposite structure and the presence of IDE which complicates the electric field solution [10, 11]. Few analytical models have been also reported on EHs using IDE. Two approaches are proposed in the literature. The first approach consists in studying a representative volume element (RVE) of the piezocomposite by benefiting from the periodicity of the material's microstructure. Den Otter [12] determined a polynomial analytic expression of the electric field and the capacitance in piezocomposite with IDEs. Later, Lloyd [13] determined an analytic solution of the electric field and potential distribution using complex analysis based on the Schwarz-Christoffel's method. Schaur and Jakoby [14] presented a more efficient and versatile semianalytical model, which yields approximate expressions for the capacitance of IDEs by integrating the electrode's thickness and the covering layer. The second approach consists in taking into account the whole microstructure of the piezocomposite. Erturk et al. [15] investigated the MFC configuration for EH by deriving a distributed-parameter electromechanical model. They assumed an empirical model of the electric field distribution in order to handle the nonuniform field. Using a quasistatic analysis, Mo et al. [16] developed an analytical model for an IDE energy harvester with monolithic piezoelectric material assuming constant and unidirectional electric field. Later, Knight et al. [17] developed an optimization of the IDE EH based on analytical modeling developed by Mo et al. [16].

In this paper, we seek a parameterized mathematical model, of an AFC microstructure, to be solved analytically in order to estimate the amount of electrical voltage that could be generated by the system when excited under harmonic transversal displacement.

2. Homogenization of Piezoelectric Fiber Composite

The first step toward the derivation of a mathematical model of the proposed AFC based energy harvester (EH) is to estimate the global effective physical properties of the unidirectional (1–3 periodic) piezoelectric fiber composite by homogenizing its internal microstructure in order to facilitate its integration into the equation of motion of the EH. The piezocomposite under study is formed by a transversely isotropic material (PZT-5A) embedded into an isotropic Epoxy matrix (see Table 1). Hence, the resulting composite is a transversely isotropic piezoelectric material too (Figure 1(a)).

Thus, the associated linear constitutive equations may be written as

$$\boldsymbol{\Sigma} = \mathbf{E}\boldsymbol{\Xi}, \tag{1}$$

where in matrix form and using Voigt notation

$$\begin{aligned} \boldsymbol{\Sigma}^t &= \left[\overline{\sigma}_1 \;\; \overline{\sigma}_2 \;\; \overline{\sigma}_3 \;\; \overline{\sigma}_4 \;\; \overline{\sigma}_5 \;\; \overline{\sigma}_6 \;\; \overline{D}_1 \;\; \overline{D}_2 \;\; \overline{D}_3\right], \\ \boldsymbol{\Xi}^t &= \left[\overline{\varepsilon}_1 \;\; \overline{\varepsilon}_2 \;\; \overline{\varepsilon}_3 \;\; \overline{\varepsilon}_4 \;\; \overline{\varepsilon}_5 \;\; \overline{\varepsilon}_6 \;\; -\overline{E}_1 \;\; -\overline{E}_2 \;\; -\overline{E}_3\right] \end{aligned} \tag{2}$$

and, for the IDE configuration, the electromechanical constants matrix is given by

$$\mathbf{E} = \begin{pmatrix} {C_{11}}^e & {C_{12}}^e & {C_{31}}^e & 0 & 0 & 0 & 0 & 0 & {e_{31}}^e \\ {C_{12}}^e & {C_{11}}^e & {C_{31}}^e & 0 & 0 & 0 & 0 & 0 & {e_{31}}^e \\ {C_{31}}^e & {C_{31}}^e & {C_{33}}^e & 0 & 0 & 0 & 0 & 0 & {e_{33}}^e \\ 0 & 0 & 0 & {C_{44}}^e & 0 & 0 & 0 & {e_{15}}^e & 0 \\ 0 & 0 & 0 & 0 & {C_{44}}^e & 0 & {e_{15}}^e & 0 & 0 \\ 0 & 0 & 0 & 0 & 0 & {C_{66}}^e & 0 & 0 & 0 \\ 0 & 0 & 0 & 0 & {e_{15}}^e & 0 & -{\epsilon_{11}}^e & 0 & 0 \\ 0 & 0 & 0 & {e_{15}}^e & 0 & 0 & 0 & -{\epsilon_{11}}^e & 0 \\ {e_{31}}^e & {e_{31}}^e & {e_{33}}^e & 0 & 0 & 0 & 0 & 0 & -{\epsilon_{33}}^e \end{pmatrix}, \tag{3}$$

where $\overline{\sigma}_i$, $\overline{D}_i$, $\overline{\varepsilon}_i$, and $\overline{E}_i$ denote average values of the homogenized material for stress, electric displacement, strain, and electric field components, respectively. ${C_{ij}}^e$, ${e_{ij}}^e$, and ${\epsilon_{ij}}^e$ denote the effective coefficients of elastic stiffness and piezoelectric and permittivity components at constant strain, respectively. The mean value of an effective physical property, bar notation, is defined as $\overline{f} = (1/V)\int_V f dV$.

Various approaches were proposed in the literature to calculate the homogenized parameters of a two-phase piezocomposite using analytical and/or numerical homogenization techniques [18, 19]. In this paper, we use both techniques to calculate the effective material coefficients of the piezocomposite. The obtained values are compared to each other for validation purposes. As an analytical approach, we propose the use of the Mori-Tanaka method (MTM). On the other hand, the finite element method (FEM), with the commercial package ANSYS, will be used as a numerical approach. In fact, several studies showed that these approaches are suitable for piezocomposites with short and long fibers [19, 20].

The use of the FEM as periodic homogenization technique consists of taking advantage of the periodicity of the physical properties of the piezocomposite by reducing the studied domain to a representative volume element (RVE) that should faithfully emulate the behavior of the entire piezocomposite. Here, the criterion for a good choice of the RVE is the equality in strain energy for the piezocomposite and homogenized structures. Figure 1(b) shows the finite element meshed model used in ANSYS for the RVE using a fiber volume fraction (FVF) of 50%. The 3D 8-node coupled-field solid finite element SOLID5 was used to mesh all volumes. Here, 2580 elements and 3216 nodes were used.

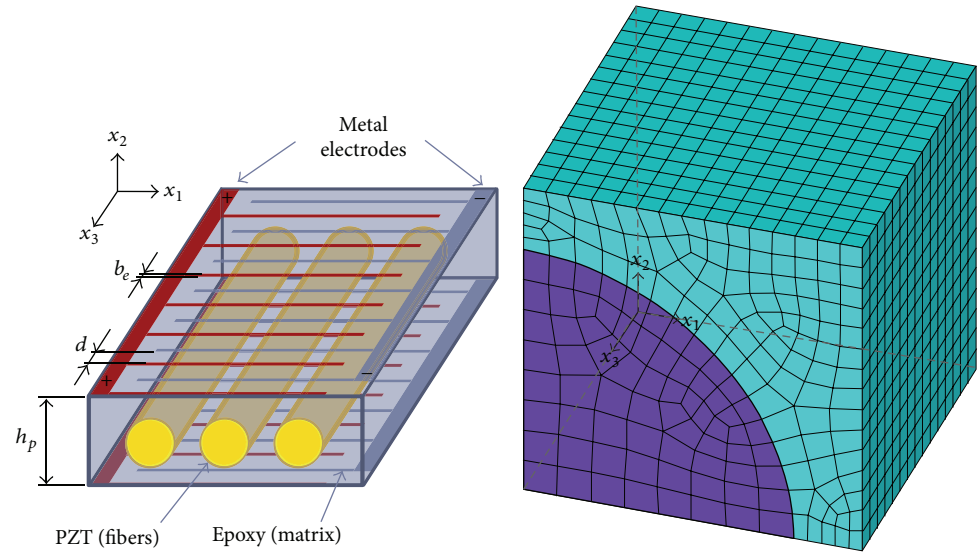

(a) Unidirectional (1–3 periodic) piezoelectric fiber composite

(b) 3D model of the RVE (50% of fiber)

Figure 1: Schematic of the active-fiber composite and its RVE.

Table 1: Material properties of the piezocomposite constituents: Fiber (PZT-5A) and Matrix (Epoxy) [23].

	C_{11} (GPa)	C_{12} (GPa)	C_{31} (GPa)	C_{33} (GPa)	C_{44} (GPa)	C_{66} (GPa)
PZT-5A	120.35	75.18	75.1	110.87	21.05	22.57
Epoxy	9.48	7.75	7.75	9.48	0.86	0.86
	e_{31} (C/m^2)	e_{33} (C/m^2)	e_{15} (C/m^2)	ϵ_{11} (10^{-9} F/m)	ϵ_{33} (10^{-9} F/m)	
PZT-5A	−5.35	15.78	12.3	9.16	8.30	
Epoxy	—	—	—	0.885	0.885	

Next, we calculate the effective electroelastic coefficients corresponding to tensile deformations of the chosen RVE, using ANSYS for different FVF [21]. To do so, the symmetry boundary conditions are firstly imposed on the planes $x_1 = 0$ and $x_2 = 0$. For a particular loading situation, only one value in the strain or electric field tensors is nonzero and all others become zero [19, 21].

In Figure 2, we plot the mechanical, electrical, and piezoelectric ratios between the effective values and the purely piezoelectric values, as a function of the FVF. We note that for high values of the FVF, the MTM is less relevant than FEM, because it assumes that the stress and strain fields inside the inclusions (fiber) are supposed to be constant, which is not the case of the FEM [19]. Thus, the FEM values corresponding to tensile deformations will be retained for the rest of this paper. However, since this FEM is not suitable to evaluate shear coefficients, where it results in a large overestimation [22], these coefficients (e_{15}, C_{44} and C_{66}) will be only determined by the MTM. In fact, while the high aspect ratio EH at hand is excited in the bending mode, structural shear deformations are not expected to be pronounced [15]. These latter will be used for 3D FEM of the EH.

3. Electric Field Considerations in the Homogenized AFC

In the case of homogenized AFC with IDEs, the corresponding electric field forms a set of curved lines, in the $(x_3 - x_2)$ plane, along the direction of the fiber. Previous studies have shown that the electric field direction within the RVE is inhomogeneous and anisotropic [11]. In our case, for simplification purposes, the homogenized material is considered to be uniformly poled in the x_3-direction [10]. This simplification is adequate for large electrodes distances, as shown later.

An appropriate electrical representative volume element (eRVE) is chosen for the electric field analysis, in which we take advantage of the symmetry inside the AFC and the associated IDE. The eRVE is composed of a monolithic homogenized material with 50% of FVF. The corresponding material properties are shown in Table 2 where the material properties corresponding to shear deformation are computed using the MTM. The electrodes were not modeled explicitly, but voltages were applied directly on nodes located at the surface where electrodes are patterned. The symmetry boundary conditions are imposed on the eRVE at the planes $x_1 = 0$ and

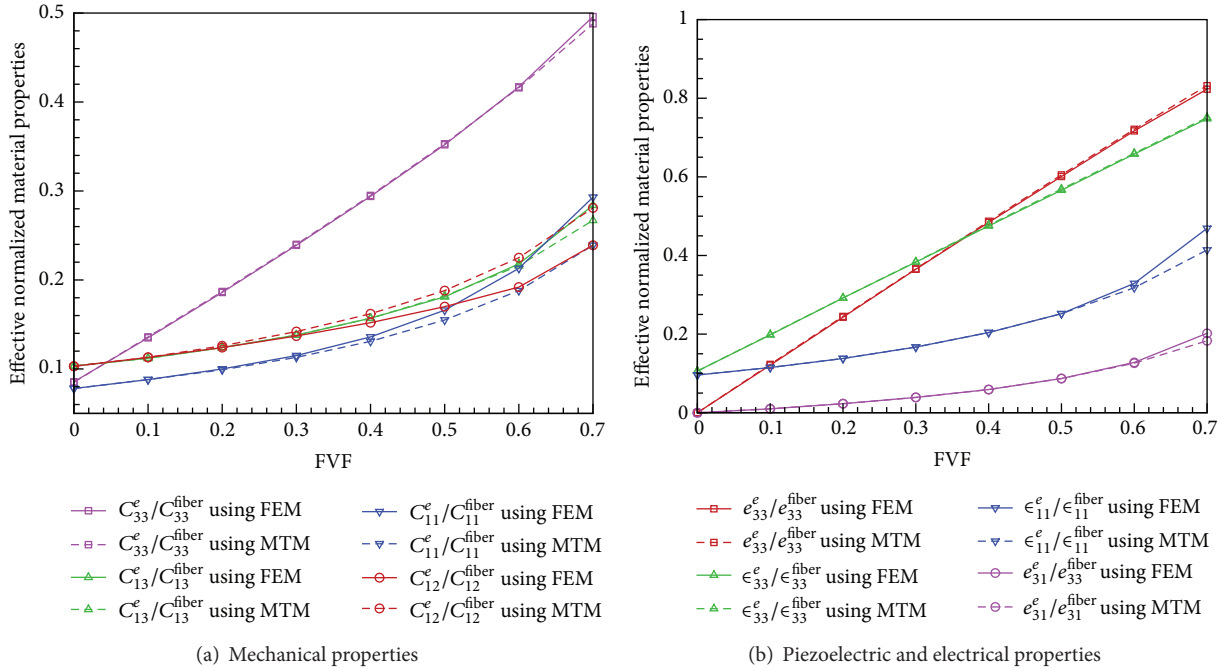

(a) Mechanical properties

(b) Piezoelectric and electrical properties

Figure 2: Material mechanical, piezoelectric, and electrical properties of the piezocomposite as a function of the fiber volume fraction.

Table 2: Material properties of the homogenized material with 50% of fiber.

C^e_{11} (GPa)	C^e_{12} (GPa)	C^e_{31} (GPa)	C^e_{33} (GPa)	C^e_{44} (GPa)	C^e_{66} (GPa)
19.97	12.77	13.59	39	2.42	3.8
e^e_{31} (C/m^2)	e^e_{33} (C/m^2)	e^e_{15} (C/m^2)	ϵ^e_{11} (10^{-9} F/m)	ϵ^e_{33} (10^{-9} F/m)	
−0.465	9.485	0.172	2.33	4.69	

$x_2 = 0$ (Figure 6) and coupled displacements are applied on plane $x_3 = 0$ of the eRVE. The eRVE is meshed using 64256 nodes and 56250 elements with a 3D coupled-field element SOLID5 (Figure 3(a)).

For modeling purposes, we consider that the electric field is significant and homogeneous in the x_3 direction only. To justify this hypothesis, we study the effect of electrode separation d for a range of electrode width b_e on the field-elongation coefficient α that characterizes the electric field shape's curvature in the x_3 direction

$$\alpha = \frac{\left|\overline{E}_3\right|}{\left|\overline{E}_2\right| + \left|\overline{E}_3\right|}. \tag{4}$$

In Figure 3(b), we can note that as the electrode separation is increased, α increases significantly. For large values of electrode separation d, the electric field becomes globally unidirectional and uniform along the x_3-axis. Thus, we can model the homogenized AFC as a piezoelectric material with transverse and parallel electrodes, in which the electrical field is uniform and aligned in the x_3-direction (Figure 5(a)). This component is formed by a series of constant electric fields connected through the electrodes separated by the distance d and electric potential V, that is,

$$E_3 = \frac{V}{d} h\left(x_3\right)\left(H\left(x_2\right) - H\left(x_2 - h_p\right)\right), \tag{5}$$

where $h(x_3)$ accounts for the spatial distribution of the electric field in the x_3-direction, and

$$h\left(x_3\right) = \sum_{i=1}^{(N-1)/2} \left\{2H\left(x_3 - (2i-1)\,d\right) - H\left(x_3 - 2id\right) - H\left(x_3 - (2i-2)\,d\right)\right\}. \tag{6}$$

Here N is the number of electrodes (odd number), H is the Heaviside step function, and $V(t)$ is the resulting potential difference between negative and positive electrodes.

4. Energy Harvester Model and Analytical Solution

We consider a bilayered cantilever beam in which one layer is made of aluminum and the other layer is made of an AFC piezocomposite patch partially covering the length of

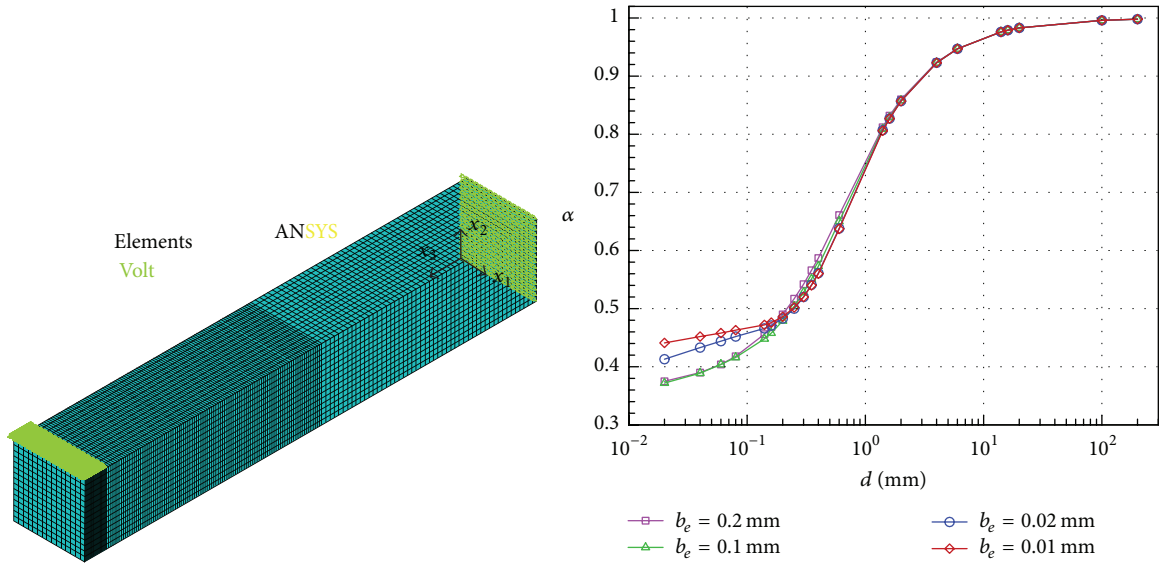

(a) Electrical representative elementary volume (eRVE)

(b) Field-elongation coefficient α variation as function of electrode's separating distance d for different values of electrode's width b_e

FIGURE 3: Electric field studies in the homogenized AFC.

the beam and placed near the clamped end. For modeling purposes, the piezocomposite is replaced by a homogenized material at 50% of FVF and crossed by N transversal IDEs perpendicular to the x_3-direction, which corresponds to the x-axis of the beam, as shown in Figure 4(a). The clamped end of the beam is excited using a transverse harmonic displacement $Y(t) = Y_0 \sin(\Omega t)$, where Ω is the driving frequency and $Y_0 = 0.1$ mm. In Table 3, we give the material and geometrical properties of the bilayered cantilever beam, where the subscript a refers to the aluminum layer and the subscript p refers to the piezoelectric layer.

The constitutive equations of an isotropic material (aluminum layer) and transversely isotropic (piezoelectric layer) material are, respectively, represented by

$$\sigma_{11}{}^{a} = E_a{}^{*} \varepsilon_{11} = \frac{E_a}{1 - \nu_a{}^{2}} \varepsilon_{11},$$
$$\sigma_{11}{}^{p} = E_p{}^{*} \varepsilon_{11} - \overline{e}^{e}_{33} E_1, \tag{7}$$

where $E_p{}^{*}$ is the effective Young's modulus and $\overline{e}^{e}_{33}$ is the piezoelectric constant at the plane-stress assumption.

To analytically model our system, we start by assuming a beam that undergoes out-of-plane bending motion only characterized by the following displacement vector:

$$\mathbf{R} = (v + Y)\,\mathbf{y} + y\ \mathbf{y}_1, \tag{8}$$

where $v(x,t)$ is the transverse displacement. $(\mathbf{x}, \mathbf{y}, \mathbf{z})$ is the inertial base frame, while the $(\mathbf{x_1}, \mathbf{y_1}, \mathbf{z})$ is the local frame attached to the beam's cross-section obtained by a rotation with respect to the z-axis. Assuming small displacements, neglecting the rotary inertia, and applying Hamilton's principle, we use the Euler-Bernoulli beam theory to write the equation of motion

$$\left[H_1 Ey_3 + H_2 E_a{}^{*} \frac{b}{3}\left(y_1^3 - y_0^3\right)\right] v^{(4)} + \left[H_1 \overline{e}^{e}_{33} \frac{V(t)}{2d} bh''(x)\left(y_2^2 - y_1^2\right)\right] + \left[H_1 m_1 + H_2 m_2\right]\left(\ddot{v} + \ddot{Y}\right) = 0, \tag{9}$$

where $m_1 = \rho_a b(y_0 - y_1) + \rho_p b(y_2 - y_1)$, $m_2 = \rho_a b h_a$, $Ey_3 = bE_a{}^{*} \int_{y_0}^{y_1} y^2 dy + bE_P{}^{*} \int_{y_1}^{y_2} y^2 dy$, $H_1 = H(x) - H(x - L_1)$, and $H_2 = H(x - L_1) - H(x - L)$. y_i denotes the different layers positions (see Figure 4(b)).

To develop a reduced-order model of the system, we use the Galerkin procedure and let the displacement $v(x,t)$ be expressed as follows:

$$v(x,t) = \sum_{r=1}^{\infty} \phi_r(x)\,\eta_r(t), \tag{10}$$

where $\phi_r(x)$ is the rth normalized mode shape of the free undamped eigenvalue problem associated with (9), when $L_1 = L$ and $\eta_r(t)$ is the modal displacement [24].

Equation (10) is substituted into the equation of motion (9) and multiplied by the mode shape function; we use the orthogonality conditions and integrate over the beam's length. The coupled electromechanical ordinary differential equation of the modal response of the EH is obtained as

$$M_r \ddot{\eta}_r(t) + C_r \dot{\eta}_r(t) + K_r \eta_r(t) + F_r = 0, \tag{11}$$

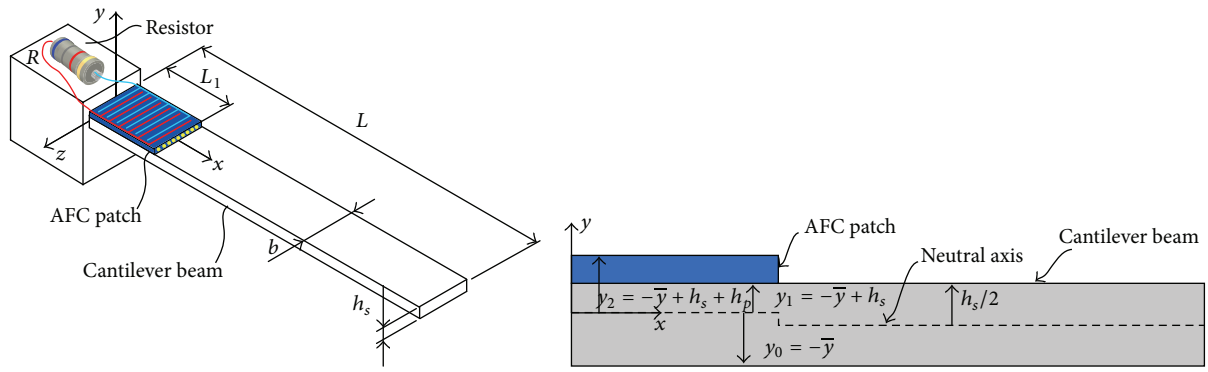

(a) Schematic of the bilayered cantilever beam

(b) Neutral axis position

Figure 4: Schematic of the energy harvester with its neutral axis position.

Table 3: Material and geometrical properties of the bi-layered cantilever beam.

L (mm)	L_1 (mm)	b (mm)	h_p (mm)	h_a (mm)	ρ_p (kg/m^3)	ρ_a (kg/m^3)	E_a (GPa)	ν_a
100	60	20	0.33	1	4475	2700	68	0.35

where the modal mass term is

$$M_r = \int_0^L \left[H_1 m_1 + H_2 m_2\right] {\phi_r}^2 (x)\, dx, \tag{12}$$

the modal damping coefficient is

$$C_r = 2\,\zeta_r \omega_r M_r, \tag{13}$$

where ω_r is the rth natural frequency and ζ_r is the modal damping ratio ($\zeta_1 = 0.017$), the modal mechanical stiffness term is

$$K_r = \int_0^L \left[H_1 E y_3 + H_2 {E_a}^* \frac{b}{3}\left({y_1}^3 - {y_0}^3\right)\right] {\beta_r}^4\, {\phi_r}^2 (x)\, dx, \tag{14}$$

where β_r is the rth frequency number given in [24], and the modal electromechanical force is expressed as

$$F_r = \int_0^L H_1 \overline{e}_{33}^e \frac{b}{2d}\left({y_2}^2 - y_1^2\right) h''(x)\, \phi_r(x)\, dx V(t) + \int_0^L \left[H_1 m_1 + H_2 m_2\right] \phi_r(x)\, dx \ddot{Y}(t). \tag{15}$$

For the electrical modeling of the homogenized AFC, we use the simplification adopted in this paper when the electrical field is parallel to the x-axis. Therefore, we can model the AFC as a series of capacitors and current sources connected in parallel (Figure 5(b)).

The output voltage $V(t)$, also shown in Figure 5(b), represents the harvested voltage from the proposed EH. This voltage is measured across the external resistor R representing the external load. Applying Gauss's law on the whole piezoelectric patch yields

$$\frac{d}{dt}\sum_{j=1}^{N-1} \int_{A_j} \mathbf{D}_j \cdot \mathbf{n}_j dA_j = \frac{V(t)}{R}, \tag{16}$$

where $\mathbf{D}_j$ is the electrical displacement vector between the electrodes, $\mathbf{n}_j$ is the electrodes normal vector, and the integration is performed over the electrode area A_j. Taking into account that the electrodes are parallel to the $(\mathbf{y}, \mathbf{z})$ plane and considering the homogenized piezoelectric constitutive equation, we obtain

$$\mathbf{D}_j \cdot \mathbf{n}_j = D_1 = \overline{e}_{33}^e \varepsilon_{11} - \overline{\epsilon}_{33}^e \frac{V(t)}{d}, \tag{17}$$

where $\overline{\epsilon}_{33}^e$ is the permittivity component at constant strain with the plane-stress assumption. Therefore, (15) is rewritten as

$$(N-1)\,\overline{\epsilon}_{33}^e \frac{b}{d}\left(y_1 - y_2\right)\dot{V}(t) + \sum_{j=1}^{N-1} \int_{(j-1)d}^{jd} \overline{e}_{33}^e \left({y_1}^2 - {y_2}^2\right) \frac{b}{2d} \dot{v}''(x,t)\, dx = \frac{V(t)}{R}. \tag{18}$$

Applying Kirchhoff laws to the equivalent electrical circuit and using Galerkin decomposition, we obtain the following equation:

$$C_P \dot{V}(t) + \frac{V(t)}{R} = i(t), \tag{19}$$

where the internal equivalent capacitance term is expressed as

$$C_P = (N-1)\,\overline{\epsilon}_{33}^e \frac{b}{d}\left(y_2 - y_1\right), \tag{20}$$

and the equivalent current source is expressed as

$$i(t) = \sum_{r=1}^{\infty} \left(\sum_{j=1}^{N-1} \overline{e}_{33}^e \left({y_1}^2 - {y_2}^2\right) \frac{b}{2d} \frac{d\phi_r(x)}{dx}\Big|_{x=(j-1)d}^{x=jd} \right) \dot{\eta}_r(t). \tag{21}$$

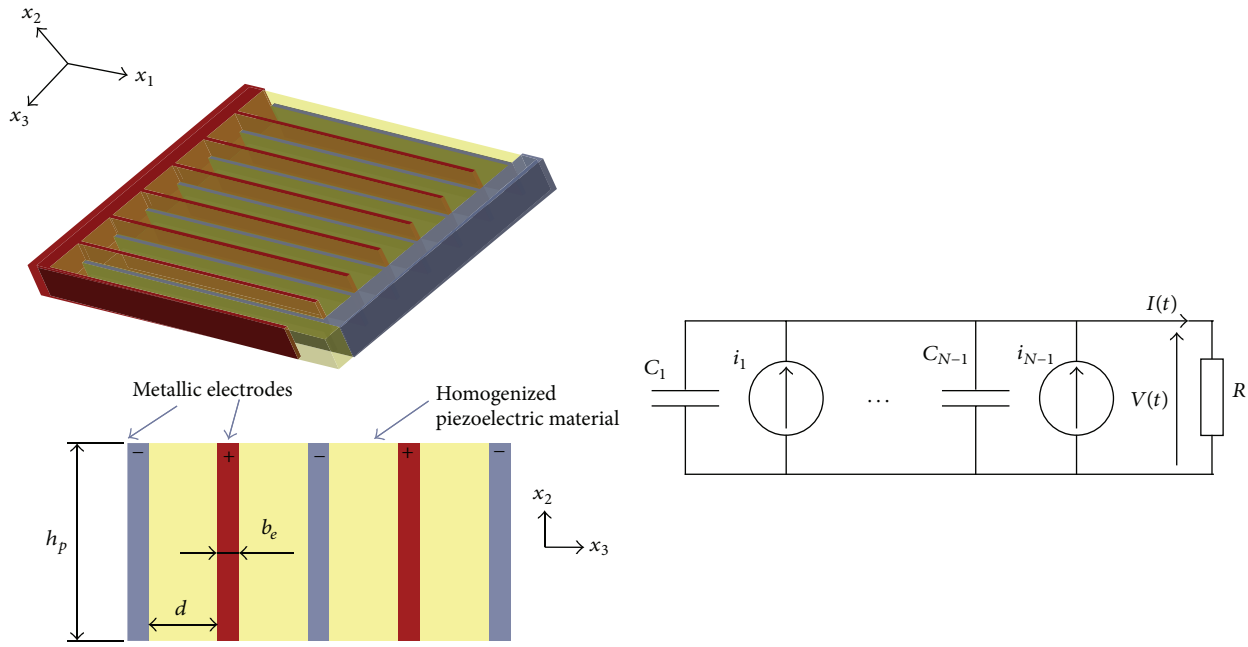

(a) Homogenized AFC patch

(b) Electrical model of the AFC

FIGURE 5: Modeling of the AFC patch.

Since the system is assumed to be linear, we assume that $\eta_r(t) = Im(\eta_r^0 e^{j\Omega t})$ and $V(t) = Im(V_0 e^{j\Omega t})$, where Im stands for the imaginary part, $j = \sqrt{-1}$ is the unit imaginary number, η_r^0 is the complex modal amplitude of the transverse displacement, and V_0 is the complex amplitude of the harmonic voltage across the resistive load. Solving the previous system analytically, we obtain the voltage V_0 amplitude as

$$V_0 = \frac{\sum_{r=1}^{\infty} \left(k_r m_r \Omega^2 Y_0 / \left(j\Omega C_r - M_r\Omega^2 + K_r\right)\right)}{C_p - \left(j/\Omega R\right) + \sum_{r=1}^{\infty} \left(k_r f_r / \left(j\Omega C_r - M_r\Omega^2 + K_r\right)\right)}. \quad (22)$$

Assuming that excitation frequencies from the environment are usually low, the fundamental mode response will be dominant and constitute our main concern in this study ($r = 1$).

5. Typical Results and FE Validation

5.1. FE Model. The FEM is used to validate the harvested voltage for different excitations near the fundamental frequency. To do so, a 3D FE model with 17 electrodes ($N = 17$ and $\alpha = 0.92$) is developed using ANSYS. Solid coupled field elements (SOLID5) are used for the piezoelectric behavior and circuit element (CIRCU94) for the piezoelectric-circuit analysis. A nil potential is applied at the nodes belonging to the negative electrodes. Also, we use equipotentiality condition for the positive electrodes' nodes. We then relate the resistive element R to the electrodes through two active nodes located on the surfaces of negative and positive electrodes of the EH. A base displacement Y_0 is applied to the clamped side of the beam at frequency Ω. The model, shown in Figure 6, has 22800 elements and 26313 nodes.

We start by calculating the mode shape and the natural frequencies of the system according to the FE model. The corresponding natural frequencies are shown in Table 4; they are compared to the ones obtained by the analytical model. As observed a mismatch of 10% is obtained. It is mainly due to the fact that the length of the AFC patch was taken to be equal to the aluminum beam in the analytical model.

5.2. Typical Results. Now, we study the response of the system to a harmonic excitation using the proposed analytical model, with one mode approximation in the Galerkin procedure, and compare the obtained results with those obtained using FE model at the same excitation conditions.

The results are given as a function of the normalized excitation frequency, obtained by dividing Ω by a factor so that the corresponding natural frequency is normalized to the FE short circuit natural frequency ω_{SC}, given in Table 4.

We plot in Figure 7(a) the frequency response curves of the maximum output amplitude voltage V_{max} for different values of load resistance R, when the number of electrodes is $N = 17$. In Figure 7(b), we vary the load resistance and look at the variation of V_{max} at the peak of the first resonant frequency; we denote this value by $V_{max}^{\omega_1}$. As shown in Figure 7, a good agreement is obtained between analytical and FE simulations demonstrating the effectiveness of the proposed model. However, the proposed model is limited to an IDE EH with relatively large electrode's distance and very small electrode's width. The IDE EH performances could be improved by selecting the correct design parameters. Hence,

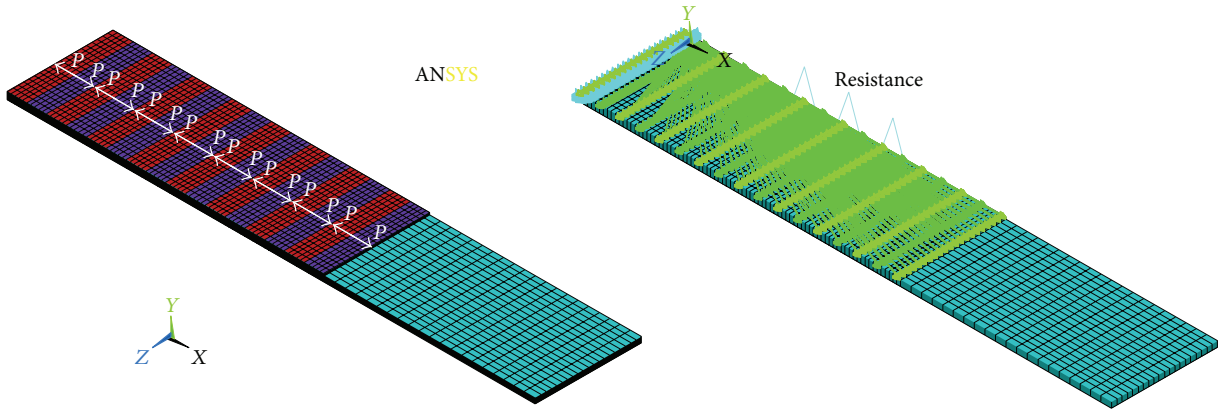

Figure 6: FE electromechanical model of the EH for $N = 17$ electrodes (P: poling direction).

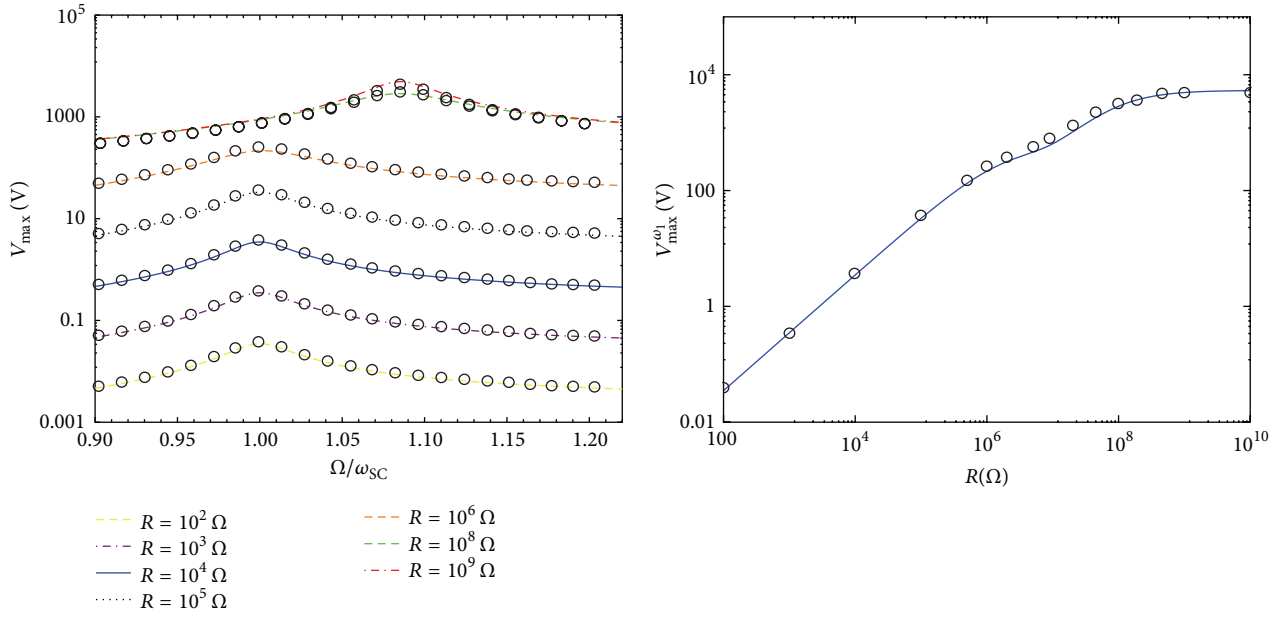

(a) Frequency response curves for V_{max} at different load resistances

(b) Variation of $V_{max}^{\omega_1}$ as a function of R

Figure 7: Analytical and FE harvested voltage at different excitation frequencies and load resistances: analytical prediction (continuous and dashed lines) and FE model (circles).

Table 4: Natural frequencies for open-circuit and short-circuit configurations when $N = 17$ electrodes.

	$\omega_1/2\Pi$ (FE)	$\omega_1/2\Pi$
Short-circuit frequency (Hz)	100.95	89.21
Open-circuit frequency (Hz)	109.62	101.41

the theoretically developed model can be used as basis for optimal design analysis.

6. Conclusion

In this paper, an analytical model of a vibrating structure, composed of an aluminum beam on top of which a piezoelectric composite patch, namely, AFC, has been attached, is derived and a closed-form solution is proposed. We use homogenization techniques to determine the effective properties of the piezoelectric composite, leading to a homogeneous model based on properties of the fiber and matrix constituents. We then used numerical simulations with ANSYS to extract the homogenized mechanical and electrical properties of the AFC. A simplified electrical field model is proposed in order to overcome the difficulty of resolving Gauss's equation for interdigitated-electrode configuration. We show that the proposed procedure could be applied to a complex piezoelectric microstructure in order to analytically derive and solve the equations of motion of such systems. We proposed closed-form solutions of the harvested electrical voltage. The proposed solutions were validated

using finite element analysis for the same homogenized material. We demonstrated that the proposed solution is in good agreement with the finite element one even for critical load resistances.

Conflict of Interests

The authors declare that there is no conflict of interests regarding the publication of this paper.

Acknowledgments

A. Jemai, F. Najar, and M. Chafra are grateful for the funding provided to their laboratory by the Tunisian Ministry of Higher Education and Scientific Research. This work was performed under the framework of the NSF International Institute for Multifunctional Materials for Energy Conversion (NSF IIMEC); all the authors would like to acknowledge the financial support by NSF Grant no. DMR-0844082.

References

[1] A. Erturk and D. J. Inman, "An experimentally validated bimorph cantilever model for piezoelectric energy harvesting from base excitations," *Smart Materials and Structures*, vol. 18, no. 2, 18 pages, 2009.

[2] A. Abdelke, A. H. Nayfeh, M. R. Hajj, and F. Najar, "Energy harvesting from a multifrequency response of a tuned bending-torsion system," *Smart Materials and Structures*, vol. 21, no. 7, Article ID 075029, 9 pages, 2012.

[3] J. H. Lim, C. H. Park, J. W. Kim, S. S. Jeong, M. H. Kim, and T. G. Park, "Generating characteristics of a cross-shaped piezoelectric generator depending on elastic body material and leg length," *Journal of Electroceramics*, vol. 30, no. 1-2, pp. 108–112, 2013.

[4] H. A. Sodano, J. Lloyd, and D. J. Inman, "An experimental comparison between several active composite actuators for power generation," *Smart Materials and Structures*, vol. 15, no. 5, pp. 1211–1216, 2006.

[5] A. A. Bent, N. W. Hagood, and J. P. Rodgers, "Anisotropic actuation with piezoelectric fiber composites," *Journal of Intelligent Material Systems and Structures*, vol. 6, no. 3, pp. 338–349, 1995.

[6] R. B. Williams, D. J. Inman, M. R. Schultz, M. W. Hyer, and W. K. Wilkie, "Nonlinear tensile and shear behavior of macro fiber composite actuators," *Journal of Composite Materials*, vol. 38, no. 10, pp. 855–869, 2004.

[7] Q.-M. Wang, X.-H. Du, B. Xu, and L. Eric Cross, "Electromechanical coupling and output efficiency of piezoelectric bending actuators," *IEEE Transactions on Ultrasonics, Ferroelectrics, and Frequency Control*, vol. 46, no. 3, pp. 638–646, 1999.

[8] H. A. Sodano, G. Park, D. J. Leo, and D. J. Inman, "Use of piezoelectric energy harvesting devices for charging batteries," in *Smart Structures and Materials 2003: Smart Sensor Technology and Measurement Systems*, vol. 5050 of *Proceedings of SPIE*, 2003.

[9] L. J. Nelson, "Smart piezoelectric fibre composites," *Materials Science and Technology*, vol. 18, no. 11, pp. 1245–1256, 2002.

[10] C. R. Bowen, L. J. Nelson, R. Stevens, M. G. Cain, and M. Stewart, "Optimisation of interdigitated electrodes for piezoelectric actuators and active fibre composites," *Journal of Electroceramics*, vol. 16, no. 4, pp. 263–269, 2006.

[11] O. J. Myers, M. Anjanappa, and C. B. Freidhoff, "Numerical modeling of a circularly interdigitated piezoelectric microactuator," *Journal of Microelectromechanical Systems*, vol. 19, no. 5, pp. 1098–1104, 2010.

[12] M. W. Den Otter, "Approximate expressions for the capacitance and electrostatic potential of interdigitated electrodes," *Sensors and Actuators A*, vol. 96, no. 2-3, pp. 140–144, 2002.

[13] J. M. Lloyd, *Electrical properties of macro-fiber composite actuators and sensors [M.S. thesis]*, Virginia Tech, 2004.

[14] S. Schaur and B. Jakoby, "An efficient method for modeling planar interdigitated electrodes for capacitive sensing," *IEEE Sensors*, vol. 13, pp. 1970–1973, 2011.

[15] A. Erturk, O. Bilgen, M. Fontenille, and D. J. Inman, "Piezoelectric energy harvesting from macro-fiber composites with an application to morphing-wing aircrafts," in *Proceedings of the 19th International Conference on Adaptive Structures and Technologies*, Ascona, Switzerland, October 2008.

[16] C. Mo, S. Kim, and W. W. Clark, "Theoretical analysis of energy harvesting performance for unimorph piezoelectric benders with interdigitated electrodes," *Smart Materials and Structures*, vol. 18, no. 5, Article ID 055017, 8 pages, 2009.

[17] R. R. Knight, C. Mo, and W. W. Clark, "MEMS interdigitated electrode pattern optimization for a unimorph piezoelectric beam," *Journal of Electroceramics*, vol. 26, no. 1–4, pp. 14–22, 2011.

[18] G. M. Odegard, "Constitutive modeling of piezoelectric polymer composites," *Acta Materialia*, vol. 52, no. 18, pp. 5315–5330, 2004.

[19] M. H. Malakooti and H. A. Sodano, "Multi-inclusion modeling of multiphase piezoelectric composites," *Composites B*, vol. 74, pp. 181–189, 2013.

[20] N. Fakri, L. Azrar, and L. El Bakkali, "Electroelastic behavior modeling of piezoelectric composite materials containing spatially oriented reinforcements," *International Journal of Solids and Structures*, vol. 40, no. 2, pp. 361–384, 2003.

[21] H. Berger, S. Kari, U. Gabbert et al., "Unit cell models of piezoelectric fiber composites for numerical and analytical calculation of effective properties," *Smart Materials and Structures*, vol. 15, no. 2, pp. 451–458, 2006.

[22] A. Deraemaeker, S. Benelechi, A. Benjeddou, and A. Preumont, "Analytical and numerical computation of homogenized prperties of MFCs: application to a composite boom with MFC actuators and sensors," in *Proceedings of the 3rd Thematic Conference on Smart Structures and Materials (ECCOMAS '07)*, Gdansk, Poland, 2007.

[23] E. Lenglet, A.-C. Hladky-Hennion, and J.-C. Debus, "Numerical homogenization techniques applied to piezoelectric composites," *Journal of the Acoustical Society of America*, vol. 113, no. 2, pp. 826–833, 2003.

[24] L. Meirovitch, *Fundamentals of Vibrations*, McGraw-Hill, New York, NY, USA, 2001.

Hindawi Publishing Corporation
Shock and Vibration
Volume 2014, Article ID 687340, 7 pages
http://dx.doi.org/10.1155/2014/687340

Research Article

Confinement of Vibrations in Variable-Geometry Nonlinear Flexible Beam

W. Gafsi,[1] F. Najar,[1] S. Choura,[2] and S. El-Borgi[3]

[1] *Applied Mechanics and Systems Research Laboratory, Tunisia Polytechnic School, BP 743, 2078 La Marsa, Tunisia*
[2] *National Engineering School of Sfax, BP 1137, 3038 Sfax, Tunisia*
[3] *Tunisia Polytechnic School, BP 743, 2078 La Marsa, Tunisia*

Correspondence should be addressed to F. Najar; fehmi.najar@gmail.com

Received 5 July 2012; Accepted 3 October 2013; Published 9 April 2014

Academic Editor: Mehdi Ahmadian

In this paper, we propose a novel strategy for controlling a flexible nonlinear beam with the confinement of vibrations. We focus principally on design issues related to the passive control of the beam by proper selection of its geometrical and physical parameters. Due to large deflections within the regions where the vibrations are to be confined, we admit a nonlinear model that describes with precision the beam dynamics. In order to design a set of physical and geometrical parameters of the beam, we first formulate an inverse eigenvalue problem. To this end, we linearize the beam model and determine the linearly assumed modes that guarantee vibration confinement in selected spatial zones and satisfy the boundary conditions of the beam to be controlled. The approximation of the physical and geometrical parameters is based on the orthogonality of the assumed linear mode shapes. To validate the strategy, we input the resulting parameters into the nonlinear integral-partial differential equation that describes the beam dynamics. The nonlinear frequency response curves of the beam are approximated using the differential quadrature method and the finite difference method. We confirm that using the linear model, the strategy of vibration confinement remains valid for the nonlinear beam.

1. Introduction

Vibration is one of the major problems that influence the performance of flexible structures. Vibration is a natural phenomenon that is unavoidable whatever its size may be, including conventional systems, such as aircraft wings, robot manipulators, blades in turning engines, crank mechanisms, and nonconventional systems that include large space structures, arm-type positioning mechanisms of magnetic disk drives, and microbeams in microelectromechanical systems. In certain cases, vibration excites unwanted resonances characterized by intolerable amplitudes. Because of the need for controlling structural vibrations and satisfying the increasing demand on security, accuracy, and long-life of these structures, researches focused on synthesizing control strategies, which are classified into three types: active [1, 2], passive [3, 4], and hybrid [5, 6]. Allaei [7] showed that vibration confinement is a superior control issue over the conventional control in isolating the sensitive parts of a structure. It has the potential to confine the vibrational energy, to reduce the control effort, and to optimize the required sensors and actuators. Choura et al. [8] proposed a design methodology for vibration confinement in nonhomogeneous rods. They established conditions for selecting the rod's material and geometrical properties by constructing positive Lyapunov functions whose derivative with respect to the space variable is required to be negative. Baccouch et al. [3] and Gafsi et al. [4] used the orthogonality conditions of mode shapes, for approximating the physical and geometrical parameters of an inhomogeneous beam for the purpose of confining the vibratory motion in prespecified parts of its spatial domain.

Structural regions, where vibrations are to be confined, experience large amplitudes [9]. These structures must be described by nonlinear models, since linear models fail to depict their dynamical behavior. Nonlinear models are characterized by natural nonlinear phenomena, such as multiple solutions, jumps, frequency entrainments, natural frequency shifts, and modal interactions resulting in energy exchanges among modes.

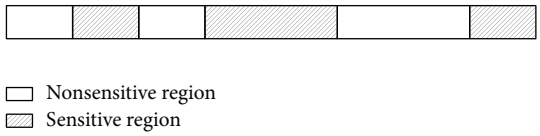

Figure 1: Flexible beam.

The aim of this paper is to develop a passive control strategy for the vibration confinement in a flexible nonlinear beam via the inverse eigenvalue problem. This strategy consists of determining the geometric and physical parameters of the structure to yield a desired set mode shapes and associated natural frequencies. Here, we consider a geometric nonlinearity due to large deflections of the beam.

2. Problem Formulation and Objectives

We consider a flexible beam composed of m regions that are sensitive to vibrations. These regions are characterized by the spatial subdomains D_{si} $(i = 1, 2, \ldots, m)$, as shown in Figure 1.

The principal objective of this study is to find sets of spatially varying geometric and physical parameters that reduce the amplitudes of vibration in its sensitive regions while confining the vibrational energy in the remainder of regions. In general, vibration confinement yields an increase of vibration amplitudes in the less sensitive parts of the beam, and thus, a nonlinear model must be considered. For this, we adopt the dynamic model for beams given by [10] based on the nonlinear 2D Euler-Bernoulli beam theory (Figure 2). They included three-dimensional stress effects (due to the out-of-plane and in-plane warpings) and geometric nonlinearities as well as anisotropy and initial curvatures, which result in linear elastic couplings. The dynamic behavior is described by

$$\begin{aligned}
&\rho A\ddot{\widehat{v}} + c\dot{\widehat{v}} - j_3\ddot{\widehat{v}}'' + \left(\widehat{E}\widehat{I}\widehat{v}''\right)'' \\
&\quad = \left[\widehat{E}\widehat{A}\left(\widehat{u}'\widehat{v}' - \widehat{u}'^2\widehat{v}' + \frac{1}{2}\widehat{v}'^3\right)\right]' \\
&\qquad + \left\{\left[\widehat{E}\widehat{I}\left(\widehat{u}'\widehat{v}'\right)'\right]'\left(1 - \widehat{u}'\right) + \left(\widehat{E}\widehat{I}\widehat{v}''\right)'\left(\widehat{u}' - \widehat{u}'^2 + \widehat{v}'^2\right)\right. \\
&\qquad\quad \left. - \left[\widehat{E}\widehat{I}\left(\widehat{u}'^2\widehat{v}' - \frac{1}{3}\widehat{v}'^3\right)'\right]'\right\}' + q_2, \\
&\widehat{\rho}\widehat{A}\ddot{\widehat{u}} - \left(\widehat{E}\widehat{A}\widehat{u}'\right)' = \left[\widehat{E}\widehat{A}\widehat{v}'^2\left(\frac{1}{2} - \widehat{u}'\right)\right]' \\
&\qquad + \left\{v'\left[\widehat{E}\widehat{I}\left(\widehat{v}' - \widehat{u}'\widehat{v}'\right)'\right]' - 2\widehat{u}'\widehat{v}'\left(\widehat{E}\widehat{I}v''\right)'\right\}',
\end{aligned} \tag{1}$$

where $\widehat{E}(\widehat{x})$ is the Young modulus, $\widehat{\rho}(\widehat{x})$ is the mass density, $\widehat{I}(\widehat{x})$ is the second moment of area, $\widehat{A}(\widehat{x})$ is the cross section area, $\widehat{c}$ is the damping coefficient, j_3 is the rotary inertia, and q_2 is the external excitation. The prime and dot denote,

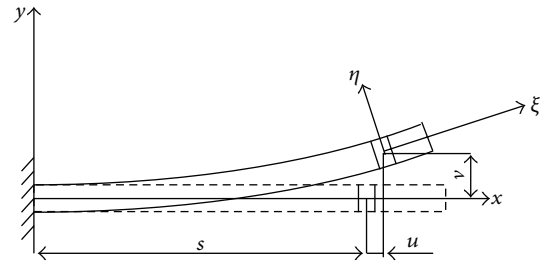

Figure 2: The nonlinear Euler-Bernoulli beam theory: undeformed coordinate system xy and the deformed coordinate system $\xi\eta$.

respectively, the spatial and time derivatives. We assume that the longitudinal deflection $\widehat{u}$ is mainly induced by the transverse deformation $\widehat{v}$ [10]; that is,

$$\widehat{u}'' = -\left(\frac{1}{2}\widehat{v}'^2\right)' + O\left(\widehat{v}^2\right). \tag{2}$$

Integrating (2) with respect to $\widehat{x}$, we obtain

$$\widehat{u}' = -\frac{1}{2}\widehat{v}'^2 + c_1(t), \tag{3}$$

where c_1 is determined by applying the boundary conditions associated with $\widehat{u}$.

3. Inverse Eigenvalue Problem

In this work, the basic idea of the proposed strategy for vibration confinement consists of altering the mode shapes and/or natural frequencies to maintain at lower levels the vibration amplitudes in the sensitive regions of the structure and allow the less sensitive regions to vibrate at relatively higher level amplitudes. Therefore, the main objective of this study is to devise a methodology for approximating a set of physical and geometrical parameters that produce vibration confinement in nonlinear structures. In this paper, we develop the methodology for controlling vibrations of beams described by the nonlinear equations (1). The strategy of vibration confinement applied to nonlinear beams consists of linearizing (1) and neglecting the axial deformation.

For convenience we define the following nondimensional variables and parameters:

$$\begin{aligned}
&E(\xi) = \frac{\widehat{E}(x)}{E_0}, \qquad \rho(\xi) = \frac{\widehat{\rho}(x)}{\rho_0}, \qquad I(\xi) = \frac{\widehat{I}(x)}{I_0}, \\
&A(\xi) = \frac{\widehat{A}(x)}{A_0}, \qquad \xi = \frac{x}{L}, \qquad u = \frac{\widehat{u}}{L}, \qquad v = \frac{\widehat{v}}{L}, \\
&\tau = \frac{t}{L^2}\sqrt{\frac{E_0 I_0}{\rho_0 A_0}}, \\
&p_1(\xi) = E(\xi) I(\xi), \qquad p_2(\xi) = \rho(\xi) A(\xi), \\
&p_3(\xi) = E(\xi) A(\xi),
\end{aligned} \tag{4}$$

where $E_0, \rho_0, I_0,$ and A_0 are the values of $\widehat{E}, \widehat{\rho}, \widehat{I},$ and $\widehat{A}$ at $x = 0$, respectively.

Therefore, the nondimensional linear model describing the beam flexure is

$$\rho A\ddot{v} + c\dot{v} + \left(EIv''\right)'' = q_2. \tag{5}$$

We now apply the strategy of vibration confinement for linear structures based on the orthogonality of linear mode shapes [4]. This strategy outputs a set of physical and geometrical parameters for the confinement of vibrations in desired regions of the structure to be controlled. Consequently, these parameters are substituted in (1) to examine the dynamical behavior of the nonlinear model that experience relatively large deflections due to confining the vibration energy around the less sensitive regions.

Without loss of generality, we consider the case of a spatially varying parameter beam clamped at both ends with vibration confinement in the middle. We consider the case of assumed modes that are constructed by premultiplying the confining function $\Gamma(\xi)$ by the modes $\Psi_i(\xi)$ $(i = 1, 2, \ldots, n)$ associated with the spatially invariant beam subjected to the same boundary conditions; that is,

$$\Psi_i(\xi) = \Gamma(\xi)\,\psi_i(\xi), \tag{6}$$

where $\psi_i(x) = C_1 \sin(\beta_i\xi) + C_2 \cos(\beta_i\xi) + C_3 \sinh(\beta_i\xi) + C_4 \cosh(\beta_i\xi)$ $(i = 1, 2, \ldots n)$. The constants C_j $(j = 1, 2, \ldots, 4)$ and β_i $(i = 1, 2, \ldots n)$ can be determined by using the boundary conditions. In order to confine the vibration in the middle of the beam, we consider, for instance, the confining function in the following Gaussian distribution $\Gamma(\xi) = e^{-\alpha\xi(1-\xi)}$, where L is the total length of the beam. This type of function gives the possibility to set the location and the amplitude of the peak of the required confinement. The interest here is to examine the effect of vibration confinement on the nonlinear behavior of the beam. In particular, we study the influence of the confinement parameter α on the frequency responses of the nonlinear beam. For this, we select a set of confinement parameters given by −2, −1, −0.5, 0, 0.5, 1, and 2. Figure 3 displays the first four assumed mode shapes of the beam for the different values of α.

We now apply the inverse eigenvalue problem to each of the values of α to determine the beam spatially varying geometry. To this end, $p_1(\xi)$ and $p_2(\xi)$ are written as linear combinations of simple polynomials [4]:

$$p_1(\xi) = a_0 + \sum_{k=1}^{p} a_k \xi^k, \qquad p_2(\xi) = b_0 + \sum_{l=1}^{q} b_l \xi^l. \tag{7}$$

To obtain accurate results, the inverse eigenvalue problem is numerically solved using the first 5 assumed modes $(n = 5)$ [4]. Figures 4 and 5 show the resulting nondimensional stiffness $p_1(\xi)$ and mass functions $p_2(\xi)$.

With reference to Nayfeh and Pai [10], the expression of $c_1(t)$ for the clamped-clamped beam is given by

$$c_1 = \frac{1}{2}\int_0^1 v'^2 d\xi. \tag{8}$$

Therefore,

$$u' = -\frac{1}{2}v'^2 + \frac{1}{2}\int_0^1 v'^2 d\xi. \tag{9}$$

Using (9), we reduce (1) into one equation in v; the equation of motion in nondimensional form is given by

$$\begin{aligned}
&p_2\ddot{v} + c\dot{v} - j_3\ddot{v}'' + \left(p_1 v''\right)'' \\
&\quad = \left[p_3 v'\left(\frac{1}{2}\int_0^1 v'^2 d\xi - \frac{1}{4}\left(\int_0^1 v'^2 d\xi - v'^2\right)^2\right)\right]' \\
&\qquad + \left\{\left[p_1\left(\frac{v'}{2}\left(\int_0^1 v'^2 d\xi - v'^2\right)\right)'\right]'\right. \\
&\qquad\quad \times\left(1 - \frac{1}{4}\left(\int_0^1 v'^2 d\xi - v'^2\right)\right) \\
&\qquad\quad + \left(p_1 v''\right)'\left(\frac{1}{2}\left(\int_0^1 v'^2 d\xi - v'^2\right)\right. \\
&\qquad\qquad\qquad \left.-\frac{1}{4}\left(\int_0^1 v'^2 d\xi - v'^2\right)^2 + v'^2\right) \\
&\qquad\quad \left.- \left[p_1\left(\frac{1}{4}\left(\int_0^1 v'^2 d\xi - v'^2\right)^2 v' - \frac{1}{3}v'^3\right)'\right]'\right\} \\
&\qquad + \frac{L^3}{E_0 I_0} q_2
\end{aligned} \tag{10}$$

with $q_2(\xi, \tau) = f_0 \cos(\Omega\tau)\delta(\xi - 1/2)$.

In order to examine the nonlinear behavior of the beam, we propose to discretize (10) using an efficient numerical technique for variable cross section beams [11, 12]. To this end, we use the differential quadrature method (DQM) to transform the integral-partial differential equation into a set of ordinary differential equations and the finite difference method (FDM) to compute a limit-cycle solution for the nonlinear beam model.

The DQM is used to solve the space dependent partial differential equation by transforming it into ordinary differential equations describing the motion of the beam with respect to time at n preselected grid points

$$\xi_i = \frac{1}{2}\left[1 - \cos\left(\frac{i-1}{n-1}\pi\right)\right]. \tag{11}$$

Following Najar et al. [11], the derivatives of the deflection with respect to space variable are expressed as a weighted linear sum of the deflection at all grid points; that is,

$$\left[\frac{\partial^r v(\xi, t)}{\partial \xi^r}\right]_{\xi=\xi_i} = \sum_{j=1}^{n} A_{i,j}^{(r)} v_j(t). \tag{12}$$

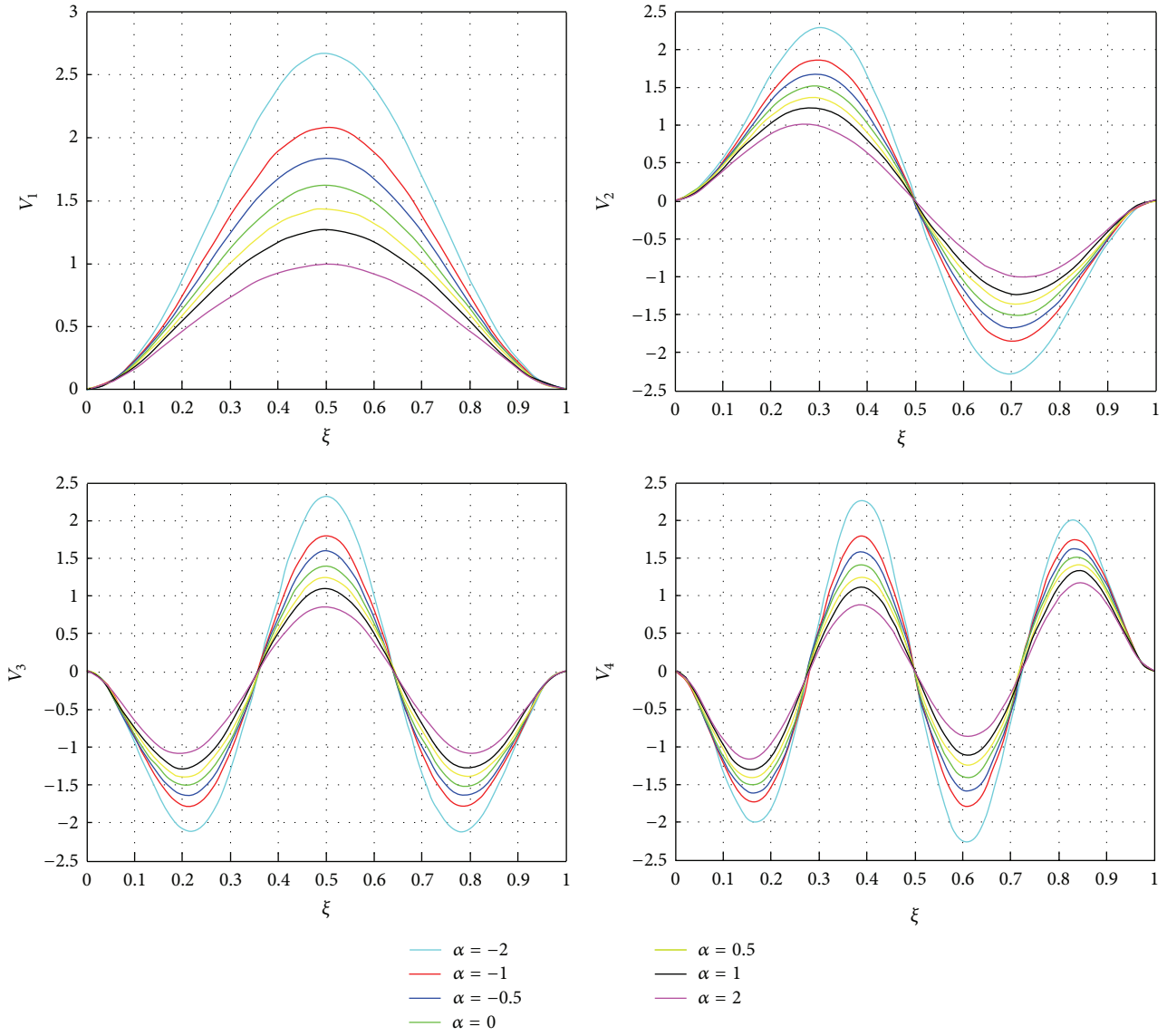

Figure 3: First four mode shapes of the linear clamped-clamped beam for different values of α.

The integral terms are discretized using the Newton-Cotes formula at the same grid points:

$$\int_0^1 v'^2 d\xi = -\int_0^1 vv'' d\xi = -\sum_{i=1}^{n}\sum_{j=1}^{n} C_i v_i A_{i,j}^{(2)} v_j$$
$$\text{where } C_i = \int_0^1 \left(\prod_{j=1;j\neq i}^{n} \frac{\xi - \xi_j}{\xi_i - \xi_j} \right) d\xi. \tag{13}$$

Using the boundary conditions, neglecting the rotary inertia, and keeping terms only to the third order, we end up with the following $n-4$ ODEs:

$$p_2(\xi)\ddot{v}_i + c\dot{v}_i + p_1''(\xi)\sum_{j=1}^{n} A_{i,j}^{(2)} v_j + 2p_1'(\xi)\sum_{j=1}^{n} A_{i,j}^{(3)} v_j + p_1(\xi)\sum_{j=1}^{n} A_{i,j}^{(4)} v_j$$
$$= -2p_1'(\xi)\left(\sum_{j=1}^{n} A_{i,j}^{(3)} v_j\right)\left(\sum_{j=1}^{n}\sum_{k=1}^{n} C_j A_{j,k}^{(2)} v_j v_k\right) + 2p_1(\xi)\left(\sum_{j=1}^{n} A_{i,j}^{(2)} v_j\right)^3 - \frac{1}{2}p_3'(\xi)\left(\sum_{j=1}^{n} A_{i,j}^{(1)} v_j\right)$$
$$\times\left(\sum_{j=1}^{n}\sum_{k=1}^{n} C_j A_{j,k}^{(2)} v_j v_k\right) + p_3(\xi)\left(\sum_{j=1}^{n} A_{i,j}^{(1)} v_j\right)^2 \sum_{j=1}^{n} A_{i,j}^{(2)} v_j - p_1''(\xi)\sum_{j=1}^{n} A_{i,j}^{(2)} v_j \left(\sum_{j=1}^{n}\sum_{k=1}^{n} C_j A_{j,k}^{(2)} v_j v_k\right)$$
$$+ p_1''(\xi)\left(\sum_{j=1}^{n} A_{i,j}^{(1)} v_j\right)^2 \sum_{j=1}^{n} A_{i,j}^{(2)} v_j$$

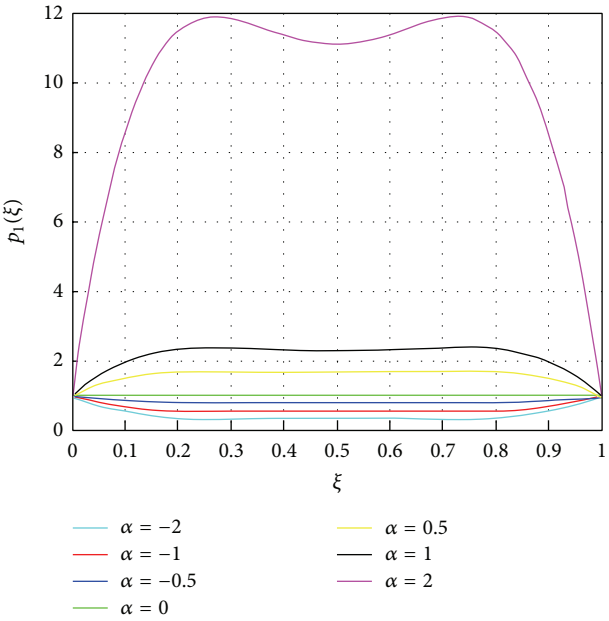

Figure 4: Variation of the beam stiffness for different values of α.

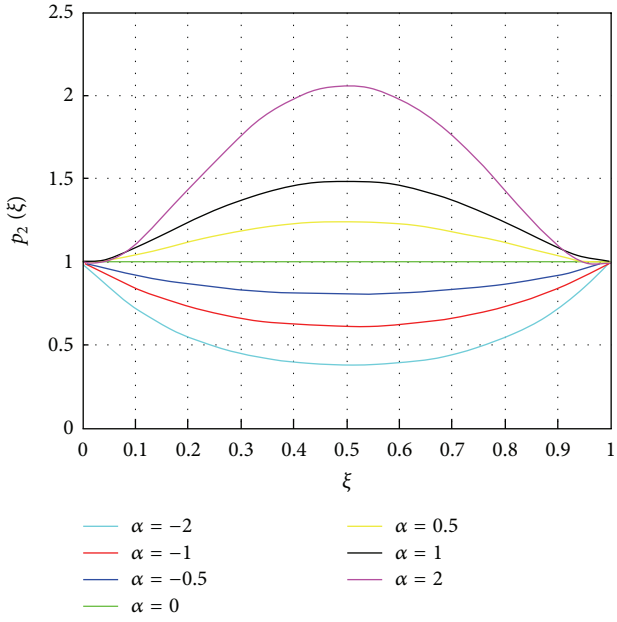

Figure 5: Variation of the beam mass for different values of α.

$$
\begin{aligned}
&-\frac{1}{2}p_3(\xi)\sum_{j=1}^{n}A_{i,j}^{(2)}v_j\left(\sum_{j=1}^{n}\sum_{k=1}^{n}C_jA_{j,k}^{(2)}v_jv_k\right)\\
&+p_1(\xi)\left(\sum_{j=1}^{n}A_{i,j}^{(1)}v_j\right)^2\left(\sum_{j=1}^{n}A_{i,j}^{(4)}v_j\right)\\
&-p_1(\xi)\sum_{j=1}^{n}\sum_{k=1}^{n}\sum_{l=1}^{n}C_jA_{j,k}^{(2)}A_{i,l}^{(4)}v_kv_jv_l\\
&+8p_1(\xi)\sum_{j=1}^{n}\sum_{k=1}^{n}\sum_{l=1}^{n}A_{i,j}^{(1)}A_{i,l}^{(2)}A_{i,k}^{(3)}v_jv_kv_l\\
&+6p_1'(\xi)\left(\sum_{j=1}^{n}A_{i,j}^{(1)}v_j\right)\left(\sum_{j=1}^{n}A_{i,j}^{(2)}v_j\right)^2\\
&+2p_1'(\xi)\left(\sum_{j=1}^{n}A_{i,j}^{(1)}v_j\right)^2\left(\sum_{j=1}^{n}A_{i,j}^{(3)}v_j\right)+q_2\\
&\qquad i=3,\ldots,n-2.
\end{aligned}
\tag{14}
$$

To obtain the limit-cycle solutions associated with the ODE system (14), we have to solve the set of equations obtained by the DQM. Using the symmetry of the problem, we end up with $(n-3)/2$ ODEs describing the motion of the system. The limit-cycle solutions are obtained by assuming that the periodic orbits have the same frequency (Ω) than the excitation. The time is normalized to 1 then discretized along one period to 100 time steps. The FDM is now applied to discretize the time. In addition we enforce the condition that the first and last solution along the orbit are equal; this will satisfy the periodicity condition of the limit-cycle solution. The final algebraic nonlinear system is solved using a Newton-Raphson technique [12].

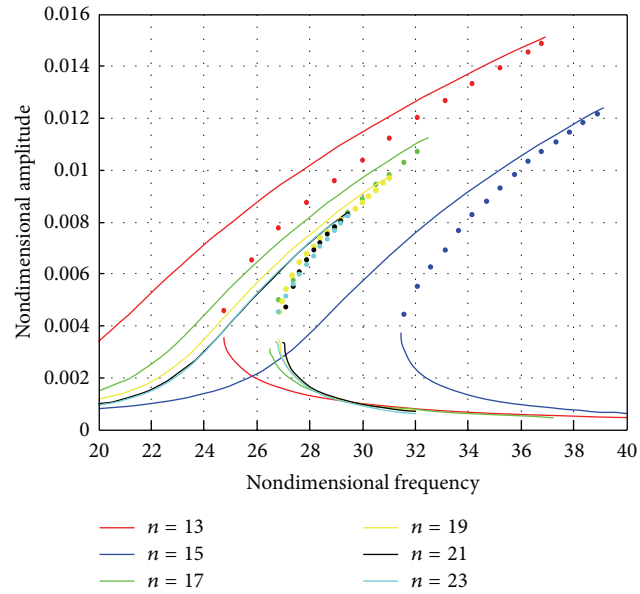

Figure 6: Frequency response convergence of a nonlinear beam $\alpha = -2$.

Before proceeding with simulating the frequency response of the nonlinear beam for different α, we test the convergence of the DQM-FDM discretization scheme. For this, we take $\alpha = -2$, $f_0 = 1000$, and $c = 60$. The resulting frequency response curves with different DQM grid points and fixed FDM grid points are shown in Figure 6. We note that the frequency response curves for $n = 19, 21, 23$ are comparable. For computational reasons, the number of 19

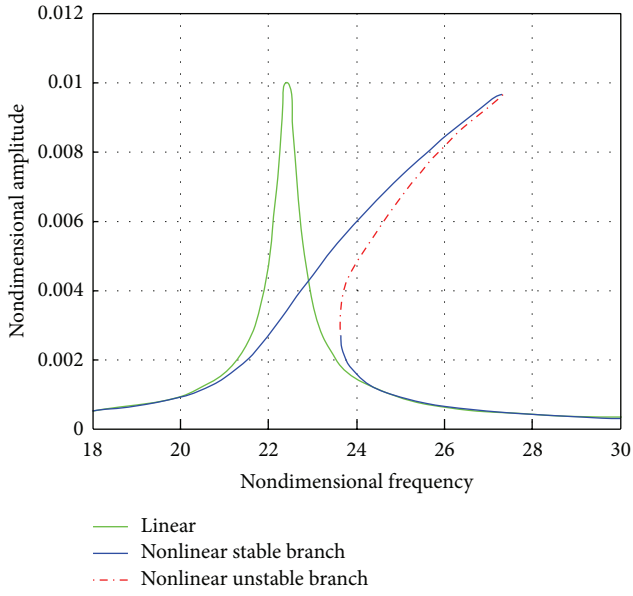

Figure 7: Frequency response of a nonlinear uniform beam $\alpha = 0$.

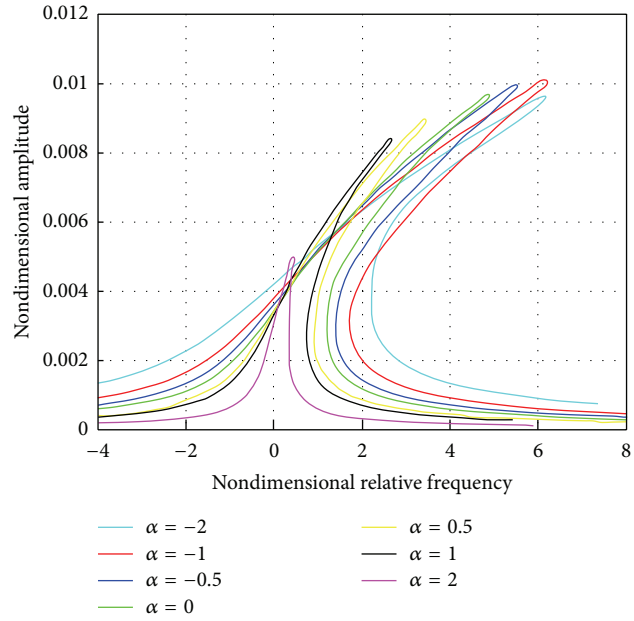

Figure 8: Comparison between the frequency responses for different values of α.

grid points is adopted for the rest of the simulations. For $n = 19$, the vibration amplitude is small when the forcing frequency is away from the first resonant frequency ($\omega_1 = 24.658$) of the linear spatially varying beam. However, when the forcing frequency comes closer to ($\omega_1 = 24.658$), relatively higher amplitudes occur while the frequency curve tilts to the right, indicating a hardening behavior of the beam.

We now investigate the influence of α on the nonlinear behavior of the spatially varying beam. Structural nonlinearities become significant when the spatially varying beam experiences large deflections. This nonlinearity is likely to introduce multitude of phenomena, such as parametric resonance, multivalued responses and jumps, and secondary resonances [13]. Figure 7 displays the frequency response curves associated with the linear and nonlinear models of a uniform beam ($\alpha = 0$). We observe that both models depict similar amplitudes of vibration away from the fundamental frequency ($\omega_1 = 22.431$). As the frequency approaches ($\omega_1 = 22.431$) either from left or right, the frequency response curves veer from each other. The nonlinear model introduces two jumps in the frequency response curves at two cyclic-fold bifurcation points leading to hysteresis. Figure 8 displays the maximum deflection of the midpoint $v_{\max}$ for different values of α as the excitation frequency Ω is varied near the corresponding fundamental frequencies (24.568, 23.058, 22.757, 22.431, 24.193, 25.145, and 40.937).

In order to compare the resulting frequency response curves at different values of α, we maintain the forcing frequency interval length at 12. We present all frequency response curves by shifting their linear natural frequencies to zero. We note that, as α is more negative, the maximum amplitude increases and the frequency response curve widens in the neighborhood of the first linear natural frequency and bends more to the right. To quantify these observations,

Table 1: Variation of the inverse fundamental frequency ω_0 and the bifurcation points Ω_{b1} and Ω_{b2} with respect to α.

α	ω_0	Ω_{b1}	Ω_{b2}	$\Delta\Omega_b$	Max amplitude
−2.0	24.658	26.84	31.01	4.17	0.009
−1.0	23.058	24.8	29.18	4.38	0.01
−0.5	22.757	24.2	28.27	4.07	0.01
0.0	22.431	23.66	27.3	3.64	0.00975
+0.5	24.193	25.2	27.7	2.5	0.009
+1.0	25.145	25.85	27.88	2.03	0.0084
+2.0	40.937	41.25	41.35	0.1	0.0052

Table 1 provides for each value of α the frequencies Ω_{b1} and Ω_{b2} corresponding to the two bifurcation points, their differences, and the maximum amplitude.

We conclude that the vibrations are more confined for more negative values of α, which lead to more concentrated mode shapes in the middle. For lower values of the force amplitude f_0, the linear and nonlinear frequency responses are nearly similar (comparable amplitudes and the nonlinear frequency curve bends slightly to the right).

4. Conclusions

In this study, we addressed the issue of vibration confinement in a nonlinear flexible beam. In particular, we considered the design of geometrical parameters of a beam whose dynamics is described by a nonlinear integral-partial differential equation. The design of these parameters was based on the linear dynamics associated with the nonlinear beam, and thus, the design of linear structures developed by Gafsi et al. [4] was adopted to approximate the geometry of the beam. The resulting parameters were then inputted into the nonlinear

integral-partial differential equation. In order to approximate the nonlinear frequency response curves of the beam as function of the confinement parameter, we discretized the nonlinear equation in space and time using DQM and FDM, respectively. In all simulations, we considered vibration confinement in the middle of the nonlinear beam. We confirmed that the strategy of vibration confinement and suppression remains valid for the nonlinear beam. We also concluded that having higher amplitudes on a larger frequency interval in conjunction with significant level of vibration confinement on a smaller region of the spatial domain presents a viable design for energy harvesting.

Conflict of Interests

The authors declare that there is no conflict of interests regarding the publication of this paper.

References

[1] A. Cavallo, C. May, A. Minardo, C. Natale, P. Pagliarulo, and S. Pirozzi, "Active vibration control by a smart auxiliary mass damper equipped with a fiber Bragg grating sensor," *Sensors and Actuators, A: Physical*, vol. 153, no. 2, pp. 180–186, 2009.

[2] S. Panda and M. C. Ray, "Active control of geometrically nonlinear vibrations of functionally graded laminated composite plates using piezoelectric fiber reinforced composites," *Journal of Sound and Vibration*, vol. 325, no. 1-2, pp. 186–205, 2009.

[3] M. Baccouch, S. Choura, S. El-Borgi, and A. H. Nayfeh, "Selection of physical and geometrical properties for the confinement of vibrations in nonhomogeneous beams," *Journal of Aerospace Engineering*, vol. 19, no. 3, Article ID 004603QAS, pp. 158–168, 2006.

[4] W. Gafsi, S. Choura, and A. Nayfeh, "Assignment of geometrical and physical parameters for the confinement of vibrations in flexible structures," *Journal of Aerospace Engineering*, vol. 22, no. 4, pp. 403–414, 2009.

[5] O. C. M. Choura, S. El-Borgi, and H. A. Nayfeh, "Hybrid control of seismically excited structures by vibration confinement," in *Proceedings of the 13th World Conference on Earthquake Engineering Vancouver*, pp. 1–6, Canada, August 2004.

[6] T. Liu, H. Hua, and Z. Zhang, "Robust control of plate vibration via active constrained layer damping," *Thin-Walled Structures*, vol. 42, no. 3, pp. 427–448, 2004.

[7] D. Allaei, "Performance comparison between vibration control by confinement and conventional control techniques," in *Proceedings of the ASME 16th Biennial Conference on Mechanical Vibration and Noise*, pp. 14–17, Sacramento, Calif, USA, 1997.

[8] S. Choura, S. El-Borgi, and A. H. Nayfeh, "Axial vibration confinement in nonhomogenous rods," *Shock and Vibration*, vol. 12, no. 3, pp. 177–195, 2005.

[9] W. Gafsi, *Passive Control of Flexible Structures by Confinement of Vibrations [Ph.D. thesis]*, ENIS, 2010.

[10] A. H. Nayfeh and P. F. Pai, *Linear and Nonlinear Structural Mechanics*, Wiley, New York, NY, USA, 2004.

[11] F. Najar, S. Choura, S. El-Borgi, E. M. Abdel-Rahman, and A. H. Nayfeh, "Modeling and design of variable-geometry electrostatic microactuators," *Journal of Micromechanics and Microengineering*, vol. 15, no. 3, pp. 419–429, 2005.

[12] F. Najar, S. Choura, E. M. Abdel-Rahman, S. El-Borgi, and A. Nayfeh, "Dynamic analysis of variable-geometry electrostatic microactuators," *Journal of Micromechanics and Microengineering*, vol. 16, no. 11, article 028, pp. 2449–2457, 2006.

[13] E. M. Abdel-Rahman, M. I. Younis, and A. H. Nayfeh, "Finite-amplitude motions of beam resonators and their stability," *Journal of Computational and Theoretical Nanoscience*, vol. 1, no. 4, pp. 385–391, 2004.

Hindawi Publishing Corporation
Shock and Vibration
Volume 2014, Article ID 937541, 10 pages
http://dx.doi.org/10.1155/2014/937541

Research Article

Numerical Study of the Active Tendon Control of a Cable-Stayed Bridge in a Construction Phase

M. H. El Ouni[1,2] and N. Ben Kahla[1,2]

[1] *Applied Mechanics and Systems Research Laboratory (AMSRL), Tunisia Polytechnic School, University of Carthage, 2078 La Marsa, Tunisia*
[2] *Higher Institute of Applied Sciences and Technologies of Sousse, University of Sousse, Taffala, Ibn Khaldoun, 4003 Sousse, Tunisia*

Correspondence should be addressed to N. Ben Kahla; nabil.benkahla@enig.rnu.tn

Received 5 July 2012; Accepted 2 March 2013; Published 9 April 2014

Academic Editor: Sami El-Borgi

This paper investigates numerically the active tendon control of a cable-stayed bridge in a construction phase. A linear Finite Element model of small scale mock-up of the bridge is first presented. Active damping is added to the structure by using pairs of collocated force actuator-displacement sensors located on each active cable and decentralized first order positive position feedback (PPF) or direct velocity feedback (DVF). A comparison between these two compensators showed that each one has good performance for some modes and performs inadequately with the other modes. A decentralized parallel PPF-DVF is proposed to get the better of the two compensators. The proposed strategy is then compared to the one using decentralized integral force feedback (IFF) and showed better performance. The Finite Element model of the bridge is coupled with a nonlinear cable taking into account sag effect, general support movements, and quadratic and cubic nonlinear couplings between in-plane and out-of-plane motions. Finally, the proposed strategy is used to control both deck and cable vibrations induced by parametric excitation. Both cable and deck vibrations are attractively damped.

1. Introduction

In the past few decades, design and construction of civil structures showed a very deep evolution because of the technological progress in materials and devices. Cable-stayed bridges increased considerably their center span from 182.6 m (Stromsund Bridge in Sweden) to 1104 m (Russky Bridge in Russia). These structures are getting more slender, light, and flexible which makes them sensitive to vibrations induced by wind, traffic, waves, or even earthquakes. Consequently, vibration control has become a major issue in civil engineering.

Vibrations in cable-stayed bridges may be reduced using passive [1–4], semiactive [5–12], and active methods [13]. Active control uses a set of actuators and sensors connected by feedback or feed forward loops. Among the proposed devices to control vibrations of cable-stayed bridges are the active mass dampers [14], active aerodynamic appendages [15], and active tendons. Several strategies have been proposed for the active tendon control of the global modes of bridges, as well as for the in-plane and out-of-plane cable vibrations. Yang and Giannopolous [16] were the first to propose active tendon control to reduce vibration induced by strong wind gusts. They studied the feedback control of a simple continuous beam model suspended by four stay cables using four active tendons equipped with servohydraulic actuators. With respect to the motion of the bridge deck detected by the sensors installed at the anchorage of each cable, the actuators actively change the cable tension and apply time-varying forces to the deck in order to reduce the vibrations. Fujino and Susumpow [17] carried out an experimental study on active control of planar cable vibration by axial support motion. Using a cable-supported cantilever beam model, Warnitchai et al. [18] performed an analytical and experimental study on active tendon control of cable-stayed bridges. They demonstrated that the vertical global

mode of the bridge can be damped with a linear feedback of the girder velocity on the active tendon displacement and that the in-plane local cable vibration can be controlled efficiently by sag induced forces. Kobayashi et al. [19] studied the tendon control of cable-stayed bridges by setting active cables parallel to stay cables. They conducted an experimental study on a 1/100 scale half-span model of a 410 m center span cable-stayed bridge to demonstrate the effectiveness of their control strategy using a tendon control force proportional to the velocity of the girder.

All the studies on active tendon control presented above used noncollocated pairs of actuator sensor which may destabilize the structure for certain gain values and may also cause spillover instability. Achkire and Preumont [20] solved this problem using a collocated displacement actuator-force sensor configuration. They considered the active vibration control of cable-stayed bridges with an active tendon controlling the axial displacement of the cable anchor point. By using a piezoelectric actuator collocated with a force sensor measuring the cable tension, integral force feedback (IFF) is applied to offer an active damping control. An experimental setup consisting of a cable in connection with a spring-mass system was tested to evaluate control efficiency. Bossens and Preumont [21] proposed a simplified linear theory to predict the closed-loop poles with a root locus technique and reported an experimental study of two cable-stayed bridge models using active tendon control. The first one is a small size mock-up (3 m-length) representative of a cable-stayed bridge in a construction phase. The second mock-up is a 30 m length cable-stayed cantilever structure, equipped with hydraulic actuators. The experimental results showed that the active tendon control brought a substantial reduction in the deck and cable vibration amplitudes. Using the same control strategy (decentralized collocated IFF), El Ouni et al. [22, 23] studied numerically and experimentally the effect of active tendon control on the principal parametric resonance of a stay cable using a small scale mock-up of a cable-stayed bridge [24]. They showed that the threshold excitation amplitude of the deck, needed to trigger the parametric excitation, increases by an increase of the active damping in the structure. Other active control laws can be also used in a similar way as the IFF, such us first order positive position feedback (PPF) proposed by Baz et al. [25] and direct velocity feedback (DVF) proposed by Balas [26].

This paper investigates numerically the active tendon control of a small scale mock-up of a cable-stayed bridge in a construction phase. Active damping is added to the structure by using pairs of collocated force actuator-displacement sensors located on each active cable. This configuration is first examined with decentralized PPF and DVF. Then, a parallel PPF-DVF is proposed to get the better of the two compensators and compared to the one using decentralized IFF. A Finite Element model of the bridge is coupled with a nonlinear cable which takes into account sag effect, general support movements, and quadratic and cubic nonlinear couplings between in-plane and out-of-plane motions. Finally, the proposed strategy is used to control both deck and cable vibrations induced by parametric excitations.

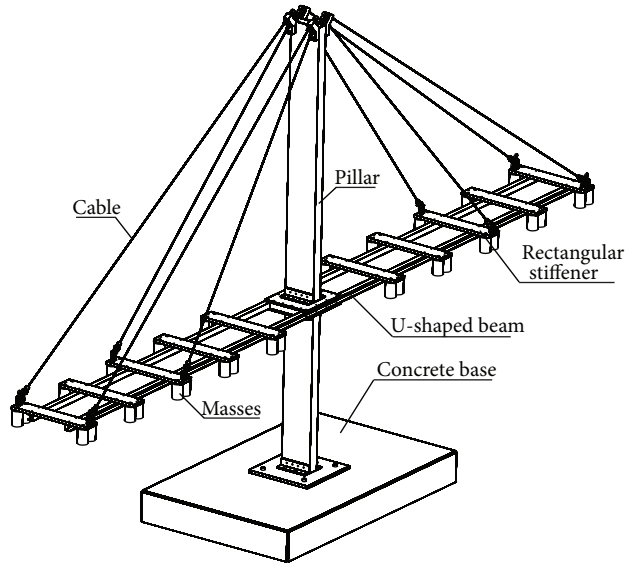

Figure 1: Description of the main components of the bridge.

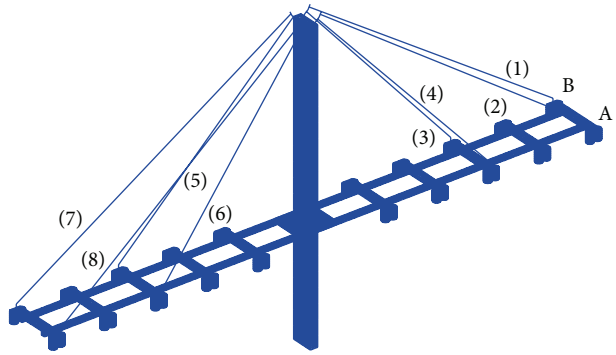

Figure 2: FE model of the bridge created by Matlab/SDT.

2. The 3D Finite Element Model

A model of a smart cable-stayed bridge was developed in Active Structure Laboratory at ULB [24]. This mock-up represents a small scale model of the bridge in a construction phase. The bridge is made of a central steel pillar resting on a concrete block and a deck supported by 8 stainless steel cables. The deck is made of two U-shaped aluminum beams, steel rectangular stiffeners, and forty additional masses (see Figure 1). The height of the pillar is 1.6 m; the total length and width of the deck are, respectively, 3 and 0.32 m. The Matlab/SDTools software has been used to build a 3D Finite Element (FE) model of the bridge (see Figure 2). Shell elements are used to model the pillar, the U-shaped beams, and the stiffeners. The additional masses are modeled by 3D elements and the cables are represented by linear bars. A clamped support condition at the lower end of the pillar is adopted. Thus, the final bridge model is composed of 29172 nodes and 23743 elements and has 112980 degrees of freedom. The natural damping of all modes of the structure is equal to 1%. For more details about the bridge demonstrator, the FE

model, and the numerical and experimental modal analysis see [23, 24].

3. Active Tendon Control Using Decentralized PPF and DVF

The global equation of motion of the linear cable-stayed bridge equipped with pairs of a force actuator and a displacement sensor in the chosen active cables (n) can be written as follows:

$$M\ddot{x} + C\dot{x} + Kx = B\,{}^{n}F_{\text{cont}} + F_{\text{excit}}, \quad (1)$$

where M, C, and K are, respectively, the mass, damping, and the stiffness of the bridge. $\ddot{x}$, $\dot{x}$, and x are, respectively, the acceleration, velocity, and displacement vectors. B is the influence matrix relating the local coordinate systems of the active tendons to the global coordinates. F_{excit} is the excitation force vector. ${}^{n}F_{\text{cont}}$ are the control forces.

The control forces of the decentralized DVF [27] are

$${}^{n}F_{\text{cont}} = {}^{n}H_1(s)\left({}^{n}x_i - {}^{n}x_j\right) = -{}^{n}g_1 s\left({}^{n}x_i - {}^{n}x_j\right), \quad (2)$$

where ${}^{n}H_1(s)$ is the feedback control law of the DVF, s is the *Laplace* variable, ${}^{n}g_1$ are the controller gains, and $({}^{n}x_i - {}^{n}x_j)$ are the relative displacements of the extremities (i and j) of the cables projected on the chord lines.

The control forces of the decentralized first order PPF [27] are

$${}^{n}F_{\text{cont}} = {}^{n}H_2(s)\left({}^{n}x_i - {}^{n}x_j\right) = \frac{{}^{n}g_2}{1+\tau s}\left({}^{n}x_i - {}^{n}x_j\right), \quad (3)$$

where ${}^{n}H_2(s)$ is the feedback controller law of the PPF, ${}^{n}g_2$ are the controller gains, and τ is a design parameter which decides the damping ratio, defines the position of the pole of the first order PPF on the real axis, and fixes the stability margin.

The main idea in developing a decentralized parallel PPF-DVF strategy is as follows: can we get the better of the two compensators in order to control the maximum of modes?

The control forces of the proposed decentralized parallel PPF-DVF strategy are

$$\begin{aligned} {}^{n}F_{\text{cont}} &= {}^{n}H_3(s)\left({}^{n}x_i - {}^{n}x_j\right) \\ &= \left[-{}^{n}g_1 s + \frac{{}^{n}g_2}{1+\tau\, s}\right]\left({}^{n}x_i - {}^{n}x_j\right), \end{aligned} \quad (4)$$

where ${}^{n}H_3(s)$ is the feedback controller law of the proposed concept and the controller gains ${}^{n}g_1$ and ${}^{n}g_2$ can be tuned to get optimal damping on the target modes. The block diagram of the proposed control system is given in Figure 3.

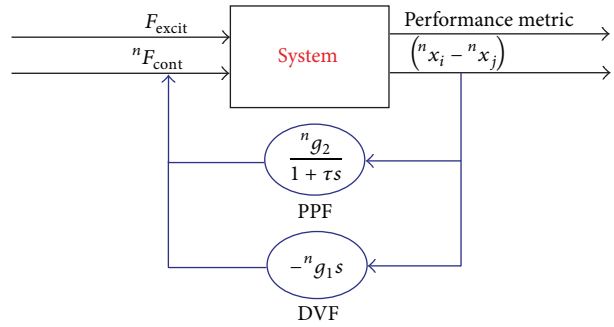

Figure 3: Block diagram of the proposed control system.

4. Comparison between Different Control Strategies

Figure 4(a) shows the root locus of the DVF added through the four small tendons. This control law is unconditionally stable for all gain values, since all loops are contained in the left side of the imaginary axis. Figure 4(b) shows the root locus of the first order PPF added through the four small tendons. The PPF is conditionally stable and has the same poles and zeros as in the DVF case, because the two controllers use the same actuator and sensor configuration. When the pole travelling on the real axis reaches the origin (the stability limit), the controller becomes unstable. In fact, when the pole reaches the stability limit the negative stiffness of the controller should exceed the static stiffness of the system, which leads to the static collapse of the bridge. For some modes, only the initial part of the loop is available, because of the stability condition. Note also that in the PPF case, the loops do not leave the open loop poles orthogonal to the imaginary axis as in the DVF case (as a result of the negative stiffness which softens the system), which suggests that the control effort may be larger [27].

Figure 4(c) shows the root locus of the proposed strategy. It is also conditionally stable but the loops of the high frequencies are wider than those of the PPF and similarly for the low frequencies which seem wider than those of the DVF. The major advantage of the proposed strategy is that the size of the loops can be tuned not only through τ but also through ${}^{n}g_1$ and ${}^{n}g_2$.

The maximum damping ratio for decentralized DVF, PPF, and parallel PPF-DVF is determined for the first 17 modes using the root locus technique and is plotted in Figure 5 as a function of mode number. The PPF seems more efficient for modes 1, 3, 5, 6, and 9. The DVF is more efficient for modes 8, 10, 11, 13, 14, and 15. The parallel PPF-DVF has important damping for many modes. With all the control strategies, weak controllability is observed for modes 2, 4, 12, 16, and 17. Figure 6 shows the FRF between the white noise excitation (F_{excit}) through the cable number 2 and the vertical displacement of the girder (U_z) in point A with different control strategies. Using the parallel PPF-DVF, the negative stiffness effect of the PPF is reduced and an average FRF is obtained between the FRF with PPF and the one with DVF.

5. Comparison between Parallel PPF-DVF and IFF

The decentralized IFF [21] uses a collocated pairs of displacement actuator-force sensor in each active cable. The IFF

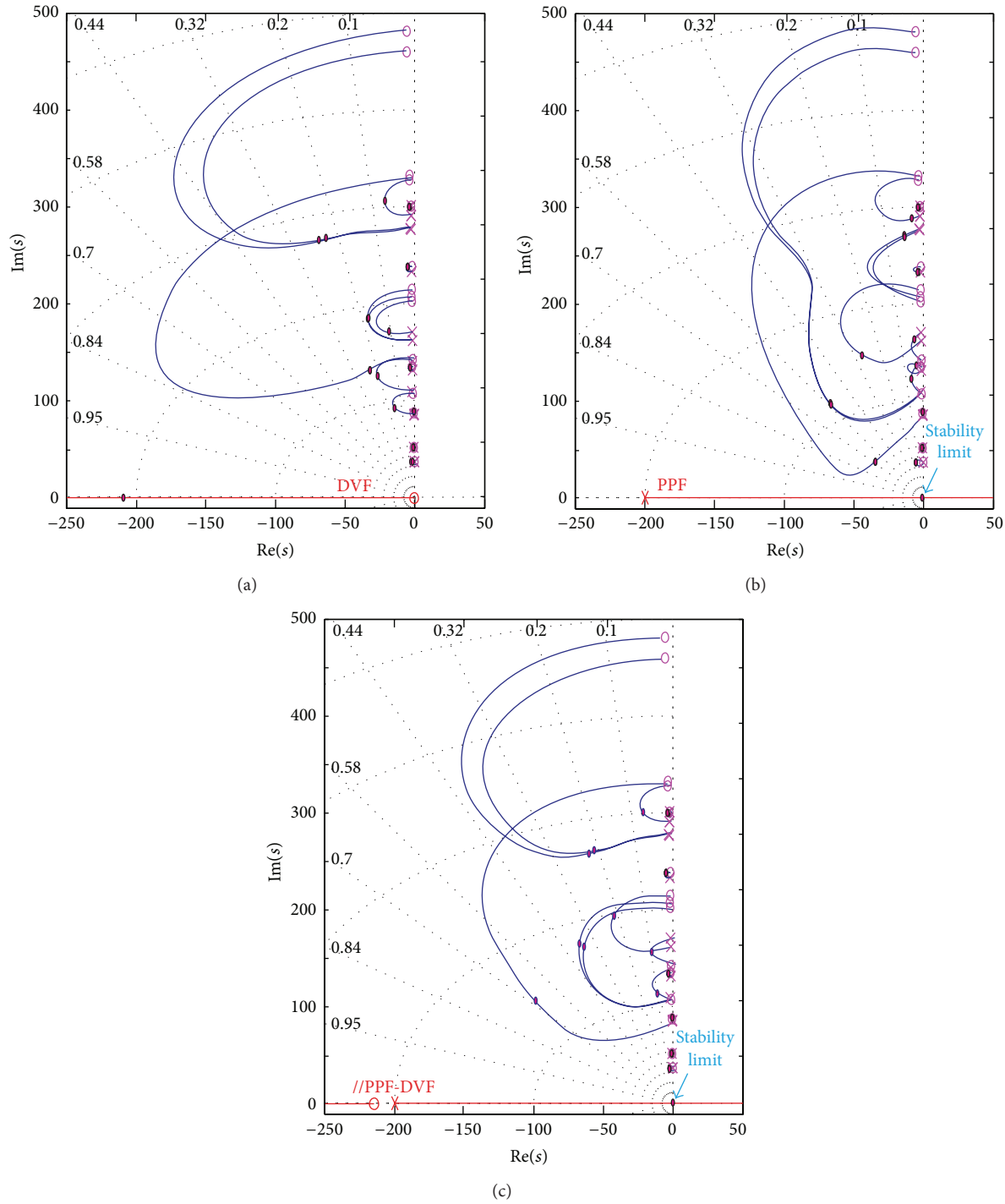

FIGURE 4: Root locus of the DVF (a), the first order PPF (b), and the parallel PPF-DVF (c) added through four small tendons.

is unconditionally stable but suffers from negative stiffness problem which may be solved by adding a 2nd order high pass filter (2 Hz) in series with the IFF [21]. The maximum damping ratio for decentralized IFF and parallel PPF-DVF are compared for the first 17 modes (see Figure 7). Both strategies successfully provide the cable-stayed bridge with active damping but the parallel PPF-DVF shows better performance for all modes except mode number 7. The proposed strategy is conditionally stable and also has a problem of negative stiffness which must be treated carefully for real applications. The FRF between the force of excitation (F_{excit}) and the vertical displacement of the deck (U_z) in point A is

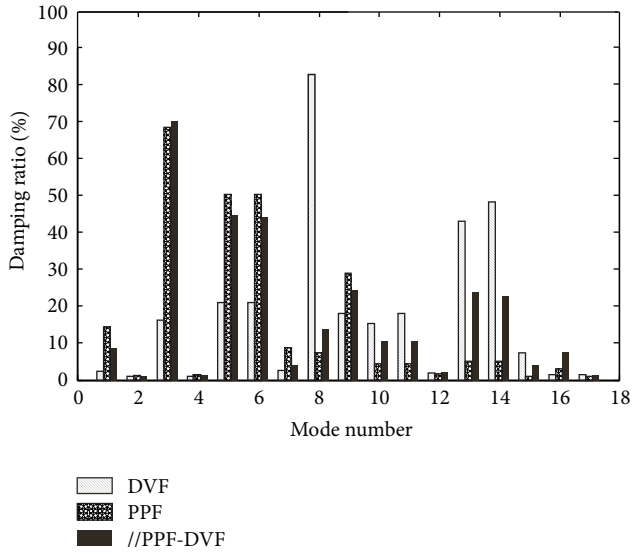

Figure 5: Maximum damping ratio as a function of mode number for different active control strategies.

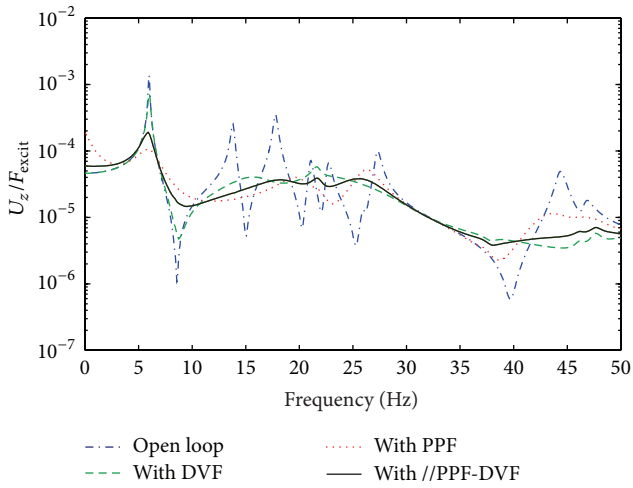

Figure 6: FRF between the force of excitation (Fexcit) and the vertical displacement of the deck (U_z) in point A, for different active control strategies.

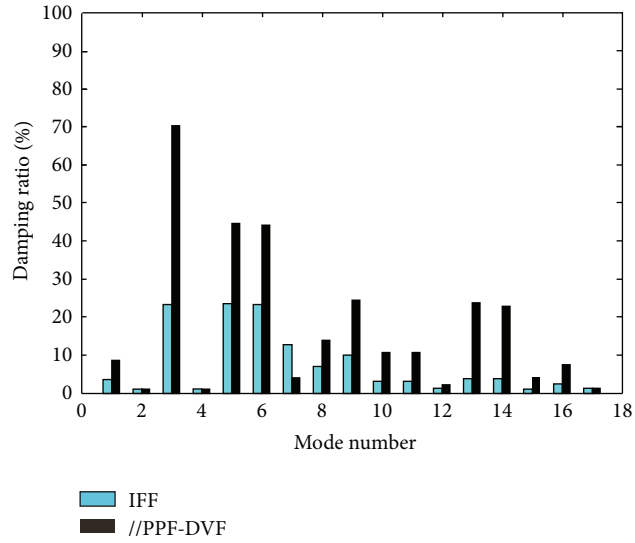

Figure 7: Maximum damping ratio as a function of mode number for IFF and parallel PPF-DVF concepts.

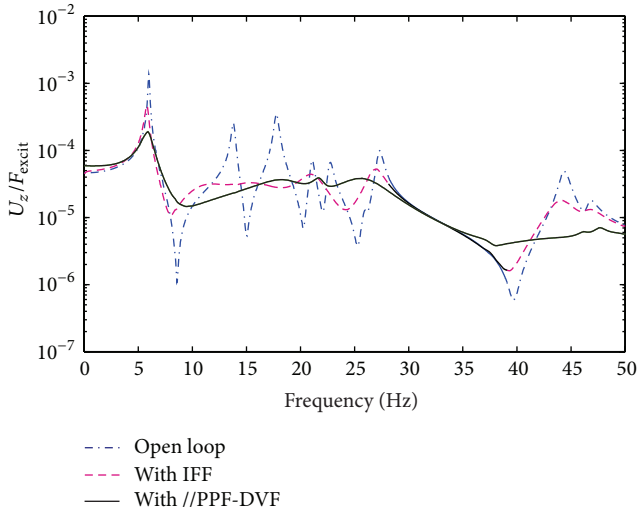

Figure 8: FRF between the force of excitation (Fexcit) and the vertical displacement of the deck (U_z) in point A for IFF and parallel PPF-DVF concepts.

plotted in Figure 8 for the two strategies with a maximum damping on mode number 1.

6. Active Tendon Control of a Nonlinear Cable-Stayed Bridge under Parametric Excitation

6.1. Nonlinear Modelling of an Inclined Small Sag Cable. The nonlinear model of the inclined cable takes into account general support movement, sag effect, and quadratic and cubic nonlinear couplings between in-plane and out-of-plane motions. The cable model is presented in Figure 9. The local coordinate system is chosen such that the x-axis is defined along the chord line and y-axis in the horizontal plane. The z-axis is then taken perpendicular to the chord line, in the gravity plane. The cable displacements are separated into three parts: the static, the quasi-static, and the dynamic contributions (for more details see [28]).

6.1.1. Out-of-Plane Cable Motion. The transverse out-of-plane displacements of the cable are described by the following equation of motion governing the generalized coordinates y_n of the nth out-of-plane mode of vibration:

$$\frac{1}{2}ml\left\{\ddot{y}_n + 2\xi_{yn}\omega_{y_n}\dot{y}_n + \frac{n^2\pi^2}{ml^2}\left(T_0 + T_q + T_d\right)y_n\right\} = F_{y_n} - \frac{ml}{n\pi}\left(\ddot{v}_a + (-1)^{n+1}\ddot{v}_b\right), \quad (5)$$

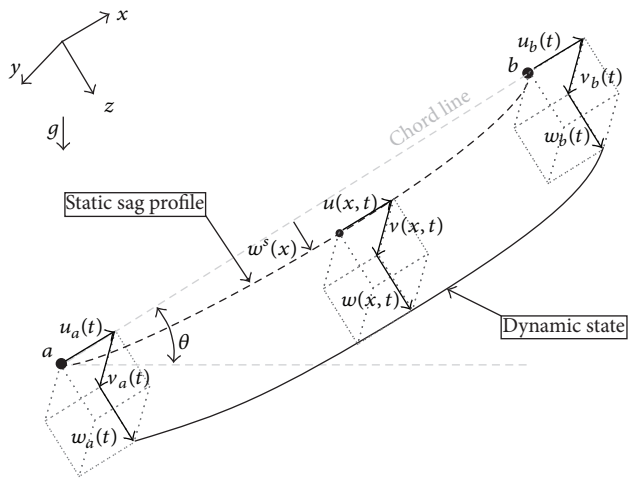

Figure 9: 3D model of an inclined cable with general support movements.

where m is the mass per unit length; is the chord length of the cable; ξ_{y_n}, ω_{y_n}, and F_{y_n} are, respectively, the modal damping, the frequency, and the modal component of the external forces applied to the cable, associated with the generalized coordinates y_n of the cable mode n; T_0, T_q, and T_d are, respectively, the static tension in the cable at its equilibrium, the tension increment induced by the support movement, and the tension increment induced by the dynamic motion of the cable; T_d is responsible for the quadratic and cubic nonlinear couplings between in-plane and out-of-plane motions; $\ddot{v}_a$ and $\ddot{v}_b$ are, respectively, the transverse acceleration of the anchorage points a and b according to the y-axis.

The expressions of T_q and T_d are given in the Appendix.

6.1.2. In-Plane Cable Motion. The in-plane displacements of the cable (perpendicular to its chord line) is described by the following equation of motion governing the generalized coordinates z_n of the nth in-plane mode of vibration and accounting for the gravity effect ($\gamma = \rho g \cos\theta$):

$$\begin{aligned}
&\frac{1}{2}ml\left\{\ddot{z}_n + 2\xi_{z_n}\omega_{z_n}\dot{z}_n + \frac{n^2\pi^2}{ml^2}\left(T_0 + T_q + T_d\right)z_n\right\} \\
&\quad = F_{z_n} - \frac{ml}{n\pi}\left(\ddot{w}_a + (-1)^{n+1}\ddot{w}_b\right) \\
&\qquad + \frac{ml^2E_q\gamma}{(\sigma^s)^2}\frac{\left(1+(-1)^{n+1}\right)}{(n\pi)^3}\left(\ddot{u}_b - \ddot{u}_a\right) \\
&\qquad - \frac{\gamma Al}{T_0}\frac{\left(1+(-1)^{n+1}\right)}{n\pi}T_d,
\end{aligned} \tag{6}$$

where E_q is the effective modulus of elasticity (see Appendix), γ is the component of distributed weight along the cable, ρ is the cable density, g is the gravity, θ is the angle of the chord line with respect to the horizontal, A is the cross section of the cable and σ^s is the static stress, ξ_{z_n}, ω_{z_n}, and F_{z_n} are, respectively, the modal damping, the frequency, and the modal component of the external forces applied to the cable, associated with the generalized coordinates z_n of the cable mode n. $\ddot{w}_a$ and $\ddot{w}_b$ are, respectively, the in-plane acceleration of the anchorage points a and b according to the z-axis. $\ddot{u}_a$ and $\ddot{u}_b$ are, respectively, the longitudinal acceleration of the anchorage points a and b according to the y-axis.

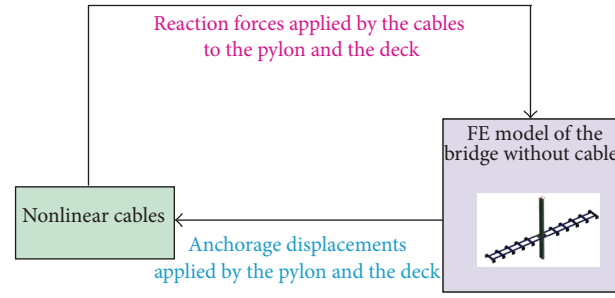

Figure 10: Principle of coupling between the FE model of the bridge and the nonlinear cables.

6.2. Coupling between the Nonlinear Cables and the FE Model of the Bridge. As an alternative to a general nonlinear Finite Element approach which would be extremely time consuming, we had developed, using SDTools [29] and Matlab/Simulink, software which combines a Finite Element model of the linear structure with a nonlinear analytical model of the cables accounting for general support movement and cubic and quadratic couplings between in-plane and out-of-plane motions of the cable. Figure 10 shows the principle of coupling between the FE model of the bridge and the nonlinear cables: the structure motion imposes displacements to the cables supports and the reactions of the cables supports act like external forces to the structure. Using SDTools, it can be achieved numerically by creating pairs of collocated force actuator-displacement sensors in the anchorage points and coupling the cables to the rest of the structure through Simulink (for more details about the coupling see [23]).

Taking into account the nonlinear dynamics of the n_c cables and active damping, the global equation of motion of the cable-stayed bridge can be expressed in modal coordinates as follows:

$$\begin{aligned}
&\mu_i\left\{\ddot{e}_i + 2\xi_i\omega_i\dot{e}_i + \omega_i^2 e_i\right\} \\
&\quad = F_i + \phi_i^T B^n F_{\text{cont}} \\
&\qquad - \phi_i^T\sum_k^{n_c}\left[\left(L_a^{kT}, L_b^{kT}\right)\left(F_{u_a}^k \;\; F_{v_a}^k \;\; F_{w_a}^k \;\; F_{u_b}^k \;\; F_{v_b}^k \;\; F_{w_b}^k\right)^T\right],
\end{aligned} \tag{7}$$

where μ_i, ξ_i, ω_i, and F_i are, respectively, the modal mass, the modal damping, the frequency, and the modal component of the external forces applied to the bridge without cables, associated with the generalized coordinates e_i of the bridge mode i. ϕ_i represents the mode shapes of the bridge without cables. L_a^{kT} and L_b^{kT} are the transformation matrices allowing the transformation from the global coordinates of the bridge to the local coordinates of the cable k. $F_{u_a}^k$, $F_{v_a}^k$, $F_{w_a}^k$, $F_{u_b}^k$, $F_{v_b}^k$,

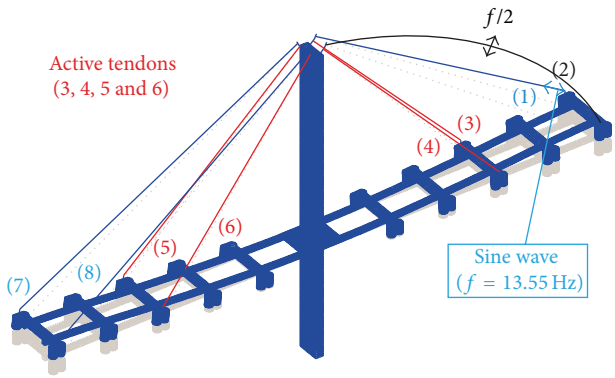

FIGURE 11: Description of the numerical experience.

and $F^k_{w_b}$ are the reaction forces on the anchorage points (a and b) written in the local coordinates of the cable k (see Appendix). ${}^nF_{\text{cont}}$ are the control forces of the n active cables and are given in (4).

The equations of motions of the cables and the bridge are solved simultaneously and interactively using the fourth and fifth order Dormand-Prince Runge-Kutta method.

6.3. Parametric Excitation. In cable-stayed bridges, the presence of many low frequencies in the deck or tower and in the stay cables may give rise to parametric excitation. The coupling between a local cable and a global structure makes the bridge sensitive to very small motion of the deck or tower which may cause dynamic instabilities and very large oscillations of the stay cables (see Figure 11). This may occur when the frequency of the anchorage motion is close to the fundamental frequency or twice the first natural frequency of the cable.

In order to produce a principal (first order) parametric excitation corresponding to a fundamental natural frequency of the in-plane mode (6.77 Hz) equal to the half of the frequency of the first symmetric flexural mode shape of the bridge (13.55 Hz), the tension of cable number 2 is tuned. Active damping is added through the four short active cables using decentralized parallel PPF-DVF strategy. Then, the global flexural mode had been harmonically excited by a frequency equal to 13.55 Hz and force amplitude of 2 N through the actuator of cable number 1. Finally, the in-plane midspan motion of cable number 2 and the deck vibration in the anchorage point A in the vertical direction had been recorded. Figure 11 describes the principle of the numerical experience. In order to produce a fundamental (second order) parametric excitation, the same numerical experience described above is repeated but the cable tension is tuned to obtain a fundamental natural frequency of the in-plane mode equal to the frequency of the first symmetric flexural mode shape of the bridge. The evolution in time of the in-plane motion of cable number 2 at midspan ($L/2$) and the deck vibration in the anchorage point A in the vertical direction, under principal and fundamental parametric excitations, are plotted in Figures 12(a) and 13(a) for both cases, with and without active control. The amplitude of the deck is well damped and the parametric resonance is cancelled. Figures 12(b) and 13(b) show the trajectory of the cable at midspan before control triggering and then during the first 10 seconds after switching on the control and finally during the last 10 seconds. The cable is attractively damped for both in-plane and out-of-plane motions.

7. Conclusions

The active tendon control of a cable-stayed bridge in a construction phase had been investigated numerically. Active damping is added to the structure by using pairs of collocated force actuator-displacement sensor located on each active cable and decentralized first order positive position feedback (PPF) or direct velocity feedback (DVF). A comparison between these two compensators showed that each one has good performance for some modes and performs inadequately with the other modes. A parallel PPF-DVF is proposed to get the better of the two compensators. The proposed strategy is then compared to the one using decentralized integral force feedback and showed better performance. Finally, the proposed strategy is applied to a nonlinear model of a cable-stayed bridge in order to control both deck and cable vibrations induced by parametric excitation. Both cable and deck vibrations are attractively damped. As a future work, a modal analysis of the cable-stayed bridge will be carried out during all the construction phases. The proposed control strategy will be improved to be adaptive to different phases of construction and semiactive tendon control of the cable-stayed bridge using MR dampers will also be investigated.

Appendix

The Irvine parameter is

$$\lambda^2 = \left(\frac{\rho l g \cos\theta}{\sigma^s}\right)^2 \frac{E}{\sigma^s}, \tag{A.1}$$

where ρ is the cable density, g is the gravity, θ is the angle of the chord line with respect to the horizontal, E is the modulus of elasticity, and σ^s is the static stress.

The effective modulus of elasticity is

$$E_q = \frac{1}{1 + (\lambda^2/12)} E. \tag{A.2}$$

The tension increment induced by the support movement is

$$T_q = T_q^{(1)} + T_q^{(2)}, \tag{A.3}$$

where

$$T_q^{(1)} = E_q A \frac{u_b - u_a}{l},$$

$$T_q^{(2)} = EA\left(1 + \frac{E_q}{\sigma^s}\frac{\lambda^2}{12 + \lambda^2}\right)\frac{(u_b - u_a)^2}{2l^2} + EA\frac{(v_b - v_a)^2}{2l^2} + EA\left(1 + \frac{\lambda^2\sigma^s}{12E}\right)\frac{(w_b - w_a)^2}{2l^2}, \tag{A.4}$$

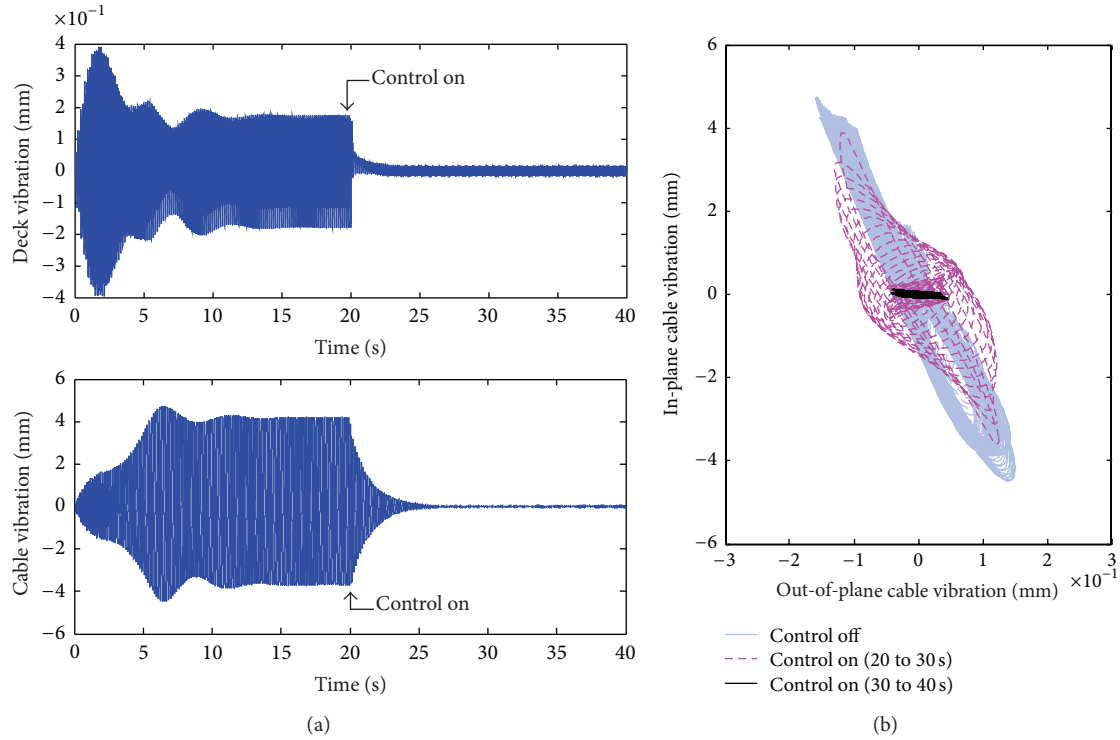

FIGURE 12: (a) Evolution in time of the vertical deck vibration and the in-plane cable vibration at $L/2$ (control on at 20 s); (b) cable trajectory at $L/2$ before and after control (case of principal parametric excitation).

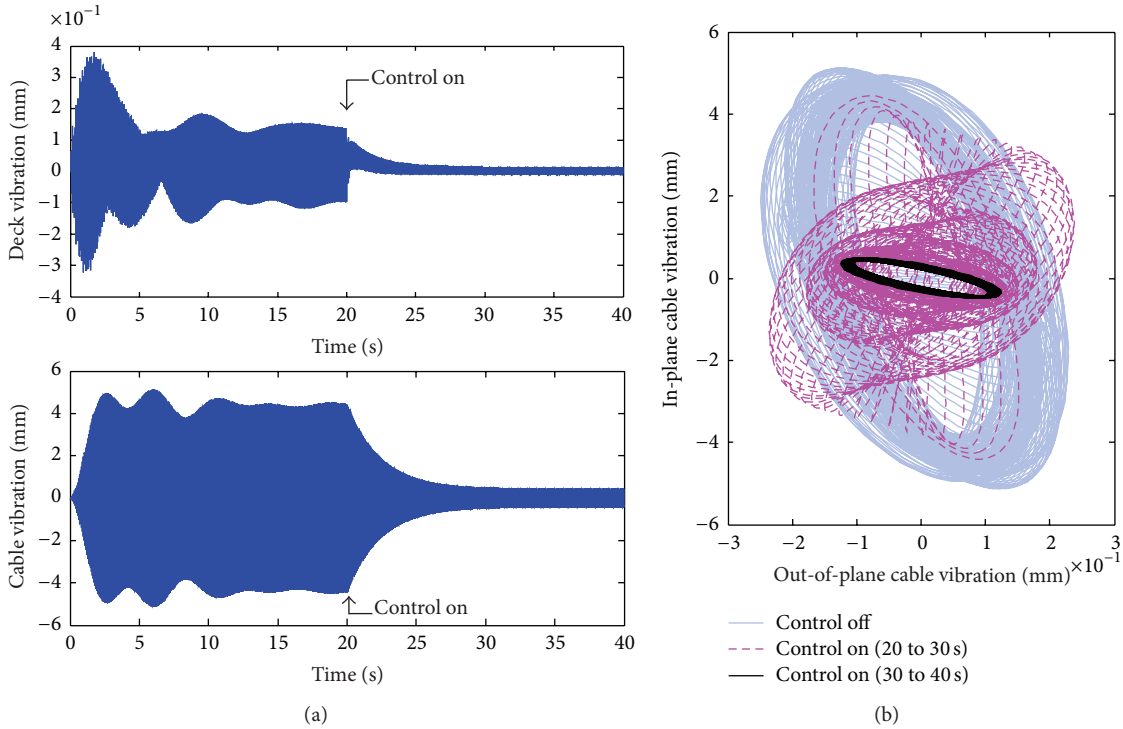

FIGURE 13: (a) Evolution in time of the vertical deck vibration and the in-plane cable vibration at $L/2$ (control on at 20 s); (b) cable trajectory at $L/2$ before and after control (case of fundamental parametric excitation).

where u_a, u_b, v_a, v_b, w_a, and w_b are the movements imposed to anchorage points.

The tension increment induced by the dynamic motion of the cable is

$$T_d = T_d^{(1)} + T_d^{(2)}, \tag{A.5}$$

where

$$\begin{aligned} T_d^{(1)} &= \frac{EA^2\gamma}{T_0}\sum_n\left[\frac{z_n}{n\pi}\left(1+(-1)^{n+1}\right)\right], \\ T_d^{(2)} &= \frac{EA}{2}\sum_n\left(y_n^2\frac{n^2\pi^2}{2l^2}\right)+\frac{EA}{2}\sum_n\left(z_n^2\frac{n^2\pi^2}{2l^2}\right) \\ &\quad -\frac{E_q}{(\sigma^s)^2}\frac{EA\gamma}{l}\frac{u_b-u_a}{l}\sum_n\left[\frac{z_n}{n\pi}\left(1+(-1)^{n+1}\right)\right]. \end{aligned} \tag{A.6}$$

The reaction forces on the cable anchorage points a and b are expressed as follow:

$$\begin{aligned} F_{u_a} &= \frac{1}{2}ml\left\{c_1\left(\ddot{u}_b-\ddot{u}_a\right)+\ddot{u}_b+c_2\left(\ddot{w}_b-\ddot{w}_a\right)\right. \\ &\qquad \left.+c_3\ddot{w}_a+c_4\sum_n\frac{1+(-1)^{n+1}}{(n\pi)^3}\ddot{z}_n\right\} \\ &\quad +\left(T_0+T_q+T_d\right) \\ &\quad \times\left\{c_5+c_6\sum_n\frac{1+(-1)^{n+1}}{(n\pi)}z_n+c_7\left(u_b-u_a\right)\right\}, \\ F_{u_b} &= \frac{1}{2}ml\left\{-c_1\left(\ddot{u}_b-\ddot{u}_a\right)+\ddot{u}_b+c_8\left(\ddot{w}_b-\ddot{w}_a\right)\right. \\ &\qquad \left.-c_3\ddot{w}_a-c_4\sum_n\frac{1+(-1)^{n+1}}{(n\pi)^3}\ddot{z}_n\right\} \\ &\quad -\left(T_0+T_q+T_d\right) \\ &\quad \times\left\{c_5+c_6\sum_n\frac{1+(-1)^{n+1}}{(n\pi)}z_n+c_7\left(u_b-u_a\right)\right\}, \\ F_{v_a} &= \frac{1}{2}ml\left\{-\frac{2}{3}\left(\ddot{v}_b-\ddot{v}_a\right)+\ddot{v}_b+2\sum_n\frac{1}{n\pi}\ddot{y}_n\right\} \\ &\quad -\left(T_0+T_q+T_d\right)\frac{v_b-v_a}{l}, \\ F_{v_b} &= \frac{1}{2}ml\left\{\frac{2}{3}\left(\ddot{v}_b-\ddot{v}_a\right)+\ddot{v}_a+2\sum_n\frac{(-1)^{n+1}}{n\pi}\ddot{y}_n\right\} \\ &\quad +\left(T_0+T_q+T_d\right)\frac{v_b-v_a}{l}, \end{aligned}$$

$$\begin{aligned} F_{w_a} &= \frac{1}{2}ml\left\{c_9\left(\ddot{w}_b-\ddot{w}_a\right)+\ddot{w}_b-c_{10}\left(\ddot{u}_b-\ddot{u}_a\right)\right. \\ &\qquad \left.+c_{11}\ddot{u}_a+2\sum_n\frac{1}{n\pi}\ddot{z}_n\right\} \\ &\quad +c_{12}\left(T_0+T_q+T_d\right)\left(w_b-w_a\right), \\ F_{w_b} &= \frac{1}{2}ml\left\{-c_9\left(\ddot{w}_b-\ddot{w}_a\right)+\ddot{w}_a+c_8\left(\ddot{u}_b-\ddot{u}_a\right)\right. \\ &\qquad \left.-c_{11}\ddot{u}_a+2\sum_n\frac{(-1)^{n+1}}{n\pi}\ddot{z}_n\right\} \\ &\quad -c_{12}\left(T_0+T_q+T_d\right)\left(w_b-w_a\right), \end{aligned} \tag{A.7}$$

where

$$\begin{aligned} c_1 &= -2\left(\frac{1}{1+(\lambda^2/12)}\right)^2\left(\frac{1}{3}+\frac{\lambda^2}{18}+\frac{\lambda^4}{432}+\frac{\lambda^2}{120}\frac{E}{\sigma^s}\right), \\ c_2 &= \frac{\lambda}{12+\lambda^2}\sqrt{\frac{\sigma^s}{E}}\left(-\frac{\lambda^2}{12}-1+\frac{E}{\sigma^s}\right), \\ c_3 &= \frac{2\lambda}{12+\lambda^2}\sqrt{\frac{E}{\sigma^s}}, \\ c_4 &= \frac{2\gamma lE_q}{(\sigma^s)^2}, \\ c_5 &= -\frac{1}{1+(\lambda^2/12)}, \\ c_6 &= \frac{\gamma A^2E_q}{T_0{}^2}, \\ c_7 &= -\frac{1}{l}\left(\frac{\lambda^2}{12+\lambda^2}\frac{E}{\sigma^s}+1\right), \\ c_8 &= -\frac{\lambda}{12+\lambda^2}\sqrt{\frac{\sigma^s}{E}}\left(\frac{E}{\sigma^s}+\frac{\lambda^2}{12}+1\right), \\ c_9 &= -\frac{2}{3}-\frac{\lambda^2\sigma^s}{60E}, \\ c_{10} &= \frac{\lambda}{12+\lambda^2}\sqrt{\frac{\sigma^s}{E}}\left(-\frac{E}{\sigma^s}+\frac{\lambda^2}{12}+1\right), \\ c_{11} &= -\frac{\lambda}{6}\sqrt{\frac{\sigma^s}{E}}, \\ c_{12} &= -\frac{1}{l}\left(1+\frac{\lambda^2\sigma^s}{12E}\right). \end{aligned} \tag{A.8}$$

Conflict of Interests

The authors declare that there is no conflict of interests regarding the publication of this paper.

Acknowledgments

The authors would like to acknowledge the support and advice of Professor André Preumont and Professor Arnaud Deraemaeker from Free University of Brussels (ULB), Belgium. The smart bridge demonstrator has been developed in the framework of the S3T Eurocores S3HM project, funded by the FNRS and the FP6-RTN-Smart Structures project funded by the European Commission.

References

[1] H. M. Ali and A. M. Abdel-Ghaffar, "Seismic energy dissipation for cable-stayed bridges using passive devices," *Earthquake Engineering and Structural Dynamics*, vol. 23, no. 8, pp. 877–893, 1994.

[2] M. Abdel-Rohman and H. Askar, "Control by passive TMD of wind-induced nonlinear vibrations in cable stayed bridges," *Journal of Vibration and Control*, vol. 2, no. 2, pp. 251–267, 1996.

[3] F. Casciati, G. P. Cimellaro, and M. Domaneschi, "Seismic reliability of a cable-stayed bridge retrofitted with hysteretic devices," *Computers and Structures*, vol. 86, no. 17-18, pp. 1769–1781, 2008.

[4] A. M. Sharabash and B. O. Andrawes, "Application of shape memory alloy dampers in the seismic control of cable-stayed bridges," *Engineering Structures*, vol. 31, no. 2, pp. 607–616, 2009.

[5] W. L. He, A. K. Agrawal, and K. Mahmoud, "Control of seismically excited cable-stayed bridge using resetting semiactive stiffness dampers," *Journal of Bridge Engineering*, vol. 6, no. 6, pp. 376–384, 2001.

[6] H. Iemura and M. H. Pradono, "Passive and semi-active response control of a cable-stayed bridge," *Earthquake Engineering and Structural Dynamics*, vol. 9, pp. 189–204, 2002.

[7] J. M. Caicedo, S. J. Dyke, S. J. Moon, L. A. Bergman, G. Turan, and S. Hague, "Phase II benchmark control problem for seismic response of cable-stayed bridges," *Journal of Structural Control*, vol. 10, no. 3-4, pp. 137–168, 2003.

[8] S. J. Moon, L. A. Bergman, and P. G. Voulgaris, "Sliding mode control of cable-stayed bridge subjected to seismic excitation," *Journal of Engineering Mechanics*, vol. 129, no. 1, pp. 71–78, 2003.

[9] A. K. Agrawal, J. N. Yang, and W. L. He, "Applications of some semiactive control systems to benchmark cable-stayed bridge," *Journal of Structural Engineering*, vol. 129, no. 7, pp. 884–894, 2003.

[10] H. Kim and H. Adeli, "Wavelet-hybrid feedback linear mean squared algorithm for robust control of cable-stayed bridges," *Journal of Bridge Engineering*, vol. 10, no. 2, pp. 116–123, 2005.

[11] S. Y. Ok, D. S. Kim, K. S. Park, and H. M. Koh, "Semi-active fuzzy control of cable-stayed bridges using magneto-rheological dampers," *Engineering Structures*, vol. 29, no. 5, pp. 776–788, 2007.

[12] M. El-Katt, R. Shaker, and Y. Kassem, "Optimum control system for seismic and aerodynamic flutter response of cable-stayed bridge using magnetorheological dampers," *Advanced Materials Research*, vol. 163–167, pp. 4269–4279, 2011.

[13] V. Gattulli and A. Paolone, "Planar motion of a cable-supported beam with feedback controlled actions," *Journal of Intelligent Material Systems and Structures*, vol. 8, no. 9, pp. 767–774, 1997.

[14] S. Qi, W. Lu, P. Chen, L. Ming, D. Ding, and J. He, "Study on cable-stayed bridge flutter active control by a single group of ADM," in *Proceedings of the 1st International Conference on Computing Control and Industrial Engineering (CCIE '10)*, pp. 426–430, Wuhan, China, June 2010.

[15] K. Wilde and Y. Fujino, "Aerodynamic control of bridge deck flutter by active surfaces," *Journal of Engineering Mechanics*, vol. 124, no. 7, pp. 718–727, 1998.

[16] J. N. Yang and F. Giannopolous, "Active control and stability of cable-stayed bridge," *ASCE Journal of Engineering Mechanics and Division*, vol. 105, no. 4, pp. 677–694, 1979.

[17] Y. Fujino and T. Susumpow, "Experimental study on active control of in-plane cable vibration by axial support motion," *Earthquake Engineering and Structural Dynamics*, vol. 23, no. 12, pp. 1283–1297, 1994.

[18] P. Warnitchai, Y. Fujino, B. M. Pacheco, and R. Agret, "An experimental study on active tendon control of cable-stayed bridges," *Earthquake Engineering and Structural Dynamics*, vol. 22, no. 2, pp. 93–111, 1993.

[19] H. Kobayashi, M. Hosomi, and K. Koba, "Tendon control for cable-stayed bridge vibration," in *Proceedings of the 1st World Conference on Structural Control*, pp. 23–29, Los Angeles, Calif, USA, 1994.

[20] Y. Achkire and A. Preumont, "Active tendon control of cable-stayed bridges," *Earthquake Engineering and Structural Dynamics*, vol. 25, no. 6, pp. 585–597, 1996.

[21] F. Bossens and A. Preumont, "Active tendon control of cable-stayed bridges: a large scale demonstrator," *Earthquake Engineering and Structural Dynamics*, vol. 30, no. 7, pp. 961–979, 2001.

[22] M. H. El Ouni, A. Deraemaeker, A. Preumont, N. Ben Kahla, and M. Abdelghani, "An experimental and numerical study of the effect of active damping on the parametric excitation," in *Proceedings of the 3rd International Congress Design and Modeling of Mechanical Systems*, Hammamet, Tunisia, 2009.

[23] M. H. El Ouni, N. Ben Kahla, and A. Preumont, "Numerical and experimental dynamic analysis and control of a cable stayed bridge under parametric excitation," *Engineering Structures*, vol. 45, pp. 244–256, 2012.

[24] A. Deraemaeker, M. H. El Ouni, I. Romanescu, and A. Preumont, "The Smart Bridge demonstrator: description of the experimental setup," in *Proceedings of the International Conference on Noise and Vibration Engineering*, Leuven, Belguim, 2008.

[25] A. Baz, S. Poh, and J. Fedor, "Independent modal space control with positive position feedback," *Journal of Dynamic Systems, Measurement and Control*, vol. 114, no. 1, pp. 96–112, 1992.

[26] M. Balas, "Direct velocity feedback control of large space structures," *Journal of Guidance, Control, and Dynamics*, vol. 2, no. 3, pp. 252–253, 1979.

[27] A. Preumont and K. Seto Wiley, Chichester, UK.

[28] F. Bossens, *Amortissement actif des structures câblées: de la théorie à l'implémentation [Ph.D. thesis]*, Université Libre de Bruxelles, 2001.

[29] http://www.sdtools.com.

Hindawi Publishing Corporation
Shock and Vibration
Volume 2014, Article ID 418178, 8 pages
http://dx.doi.org/10.1155/2014/418178

Research Article

Fault Diagnosis of Rotating Machinery Based on Multisensor Information Fusion Using SVM and Time-Domain Features

Ling-li Jiang,[1,2] Hua-kui Yin,[1] Xue-jun Li,[2] and Si-wen Tang[1]

[1] *Engineering Research Center of Advanced Mining Equipment, Ministry of Education, Hunan University of Science and Technology, Xiangtan 411201, China*
[2] *Hunan Provincial Key Laboratory of Health Maintenance for Mechanical Equipment, Hunan University of Science and Technology, Xiangtan 411201, China*

Correspondence should be addressed to Ling-li Jiang; linlyjiang@163.com

Received 5 August 2012; Accepted 27 November 2012; Published 8 April 2014

Academic Editor: Valder Steffen

Multisensor information fusion, when applied to fault diagnosis, the time-space scope, and the quantity of information are expanded compared to what could be acquired by a single sensor, so the diagnostic object can be described more comprehensively. This paper presents a methodology of fault diagnosis in rotating machinery using multisensor information fusion that all the features are calculated using vibration data in time domain to constitute fusional vector and the support vector machine (SVM) is used for classification. The effectiveness of the presented methodology is tested by three case studies: diagnostic of faulty gear, rolling bearing, and identification of rotor crack. For each case study, the sensibilities of the features are analyzed. The results indicate that the peak factor is the most sensitive feature in the twelve time-domain features for identifying gear defect, and the mean, amplitude square, root mean square, root amplitude, and standard deviation are all sensitive for identifying gear, rolling bearing, and rotor crack defect comparatively.

1. Introduction

Typical rotating machinery systems such as water turbine, steam turbine, wind turbine, and rotary kiln are critical core equipment support of the important industries of the national economy [1, 2]. The safety, reliability, efficiency, and performance of rotating machinery are major concerns in industry, so, the task of condition monitoring and fault diagnosis of rotating machinery is significant [3]. The common mechanical defects of rotating machinery are divided into three categories: (1) rotor body defects, such as unbalance, misalignment, rubbing, and rotor crack; (2) rotor support-bearing defects, such as inner race, outer race or ball defect of rolling bearing, and oil whirl or oil whip of sliding bearing; (3) transmission gear defects, such as chipped tooth defect or missing tooth defect. In-process monitoring and diagnostics of rotating machinery require reasoning about defect and process states from sensor readings. Often the relationship between the sensor readings and the process states is complex and nondeterministic. For a complex system, a single sensor is incapable of collecting enough data for accurate condition monitoring and fault diagnosis. Multiple sensors are needed in order to do a better job. When multiple sensors are used, data collected from different sensors may contain different partial information about the same machine condition. The diagnostic object can be described more comprehensively [4–6]. Compared with single sensor, the time-space scope and the quantity of information are expanded. The diagnostic accuracy and reliability can be improved. Multisensor information fusion can be categorized into three levels [7, 8]: data-level fusion, feature-level fusion, and decision-level fusion.

At data-level fusion, all sensor data from a measured object are combined directly and features are then calculated from the fused data. Fusion of data at this level contains most information and can deliver good results. However, the sensors used in this level must be commensurate. That means

the measurement has to be the same or has similar physical quantities or phenomena. During the most popular data-level fusion methodology, such as weighted fusion [9], the weighted value of multisensor signals is difficult to determine. As a consequence, data-level applications are limited in real environment. At feature-level fusion, the features are calculated from each sensor according to the type of raw data. Then, these noncommensurate sensors features are combined at the feature level. All features are combined in turn into a bigger single feature set, which are then used in a special classification model such as artificial neural network (ANN), support vector machine (SVM), and cluster algorithm for decisions [10]. The feature-level fusion is a compromise form of data-level fusion and decision-level fusion. Its data alignment requirements are not strict as the data-level fusion that heterogeneous sensors are allowed, and its information loss is less serious than the decision-level fusion but still achieved a better information compression. As a consequence, feature-level applications are flexible and popular. At decision-level fusion, the processes of features calculation and pattern recognition are applied in sequence for single-source data obtained from each sensor. The decision vectors are then fused using decision-level fusion techniques such as voting strategy, Bayesian method, behavior-knowledge space, and Dempster-Shafer theory [11]. Relatively speaking, there is maximum amount of information loss at decision-level.

This paper proposes a feature-level fusion method for rotating machinery fault diagnosis. Generally, heterogeneous information fusion is executed at feature-level fusion for mechanical condition monitoring and fault diagnosis in the present literature. For example, Barad et al. put forward the development of an ANN based model for condition monitoring of a power turbine that blends parameters belonging to performance, vibration, and lubrication [8]; Loutas et al. combined use of vibration, acoustic emission, and oil debris monitoring of rotating machinery [6]. The condition of mechanical system may be described in more detail by using heterogeneous information fusion, but this process needs multiclass sensors and its matching data acquisition systems, which would lead to higher monitoring costs and inconvenient operation of data acquisition in the real environment. ANN and SVM are the most popular classification models to execute decision at feature-level fusion [12, 13]. The main difference between ANN and SVM is in their risk minimization. SVM is based on structural risk minimization principle, whereas ANN is based on traditional empirical risk minimization principle. The difference in risk minimization leads to a better generalization performance for SVM than that of ANN [14, 15]. SVM is powerful for solving the problem with small sampling, nonlinear and high dimension in machinery condition classification. In this paper, the proposed feature-level fusion method belongs to homologous information fusion that the raw data all come from vibration sensors, so only a vibration testing system is needed for raw signal collected, which makes the process simpler. In this method, time-domain features are calculated from each vibration signal to compose a multidimensional feature set, and the SVM is selected as the classification model to process information fusion. In order to verify the effectiveness of the proposed method, fault diagnostic cases are tested, which include fault diagnosis of rolling bearing (identifying normal, inner race defect, outer race defect, and ball defect), fault diagnosis of gear (identifying normal, chipped tooth, and missing tooth), and fault diagnosis of rotor crack (identifying normal, crack depth of 3 mm, and crack depth of 5 mm). For each case study, the sensibilities of the features are analyzed.

2. Theory

2.1. Support Vector Machine (SVM). The SVM is a machine learning method based on the statistical learning theory and structural risk minimization principle. Given two category sample sets (x_i, y_i) $(x_i \in R^d; y_i \in \{-1, +1\}; i = 1, 2, \ldots, n)$, n is the number of samples. The optimal hyperplane separating the data can be obtained as a solution to the following optimization problem [15, 16]:

$$\begin{aligned} \text{Min} \quad & \frac{1}{2}\|\varpi\|^2 + C\sum_{i=1}^{n}\xi_i \\ \text{s.t.} \quad & y_i\left[(\varpi \cdot x_i) + b\right] \geq 1 - \xi_i \quad (\xi_i \geq 0), \end{aligned} \tag{1}$$

where ω is weight vector, b is scalar, ξ_i is slack variable, and C is error penalty.

The dual quadratic optimization description can be obtained by converting the problem with Kuhn-Tucker condition into the equivalent Lagrangian dual problem:

$$\begin{aligned} \text{Max} \quad & \sum_{i=0}^{n}\alpha_i - \frac{1}{2}\sum_{i=1}^{n}\sum_{j=1}^{n}\alpha_i\alpha_j y_i y_j \left(x_i \cdot x_j\right) \\ \text{s.t.} \quad & \sum_{i=1}^{n}\alpha_i y_i = 0 \quad (0 \leq \alpha_i \leq C), \end{aligned} \tag{2}$$

where α_i is Lagrange coefficient, which must meet the following equation:

$$\alpha_i\left\{y_i\left[(\varpi \cdot x_i) + b\right] - 1 + \xi_i\right\} = 0. \tag{3}$$

The support vector is the sample which satisfies the equation $y_i[(\omega \cdot x_i) + b] = 1 - \xi_i$ at the time of the nonzero α_i. It reveals that the samples at the edge of distribution are essential for classification. This leads to the optimal classification decision function:

$$f(x) = \text{sgn}\left\{\sum_{i=1}^{l}\alpha_i^* y_i\left(x_i \cdot x\right) + b^*\right\}, \tag{4}$$

where l is the number of support vectors.

In linear inseparable condition, the samples (x_i, y_i) $(x_i \in R^d; y_i \in \{-1, +1\}; i = 1, 2, \ldots, n)$ in input space are mapped into high dimensional space H where the optimal classification surface can be established through the nonlinear mapping $\Phi : R^d \rightarrow H$. The nonlinear mapping Φ is usually difficult to be solved while kernel functions $K(x_i, x_j)$

meeting Mercer conditions can be used to solve this problem dexterously. The kernel function is described as follows:

$$K\left(x_i, x_j\right) = \left\langle \Phi\left(x_i\right) \cdot \Phi\left(x_j\right) \right\rangle. \quad (5)$$

The optimal classification decision function of linear inseparable samples is obtained using (5) into (4):

$$\begin{aligned} f(x) &= \operatorname{sgn}\left\{ \sum_{i=1}^{l} \alpha_i^* y_i \left\langle \Phi\left(x_i\right) \cdot \Phi\left(x_j\right) \right\rangle + b^* \right\} \\ &= \operatorname{sgn}\left\{ \sum_{i=1}^{l} \alpha_i^* y_i K\left(x_i, x_j\right) + b^* \right\}. \end{aligned} \quad (6)$$

The common kernel functions include linear kernel function, poly kernel function, radial basis function (RBF) kernel function, and sigmoid kernel function.

The traditional SVM was originally designed for binary classification problems. However, many practical problems in fault diagnosis field are multiclassification. Now some effective multiclass support vector machines were proposed which include "one-against-one," "one-against-all," directed acyclic graph (DAG), and so on [15]. Hsu et al. have given a comparison of these methods and pointed out that the "one-against-one" method is more suitable for practical use than other methods [17, 18].

2.2. Time-Domain Features. When the running conditions of the rotating machinery deviate from the normal condition, the time-domain statistical features of the vibration signal will be different from the normal condition. Furthermore, the time-domain statistical features will be also different under different defect models. Therefore, the time-domain statistics contain abundant defect information, and they can be used as sensitive character applied to fault diagnosis of rotating machinery. The time-domain statistical features used in this study are shown in Table 1.

2.3. Multisensors Information Fusion Model. The model of multisensor information fusion is used in this study and shown in Figure 1. The same character of different sensors is extracted to constitute a multidimensional vector and the SVM is used for pattern recognition. Twelve different time-domain features are analyzed one by one.

Table 1: The statistic features in time domain.

Code name	Feature	Equation
f_1	Mean ($\overline{x}$)	$\overline{x} = \frac{1}{n}\sum \lvert x_i \rvert$
f_2	Peak (x_p)	$x_p = \max(\lvert x_i \rvert)$
f_3	Amplitude square (x_e)	$x_e = \sum_{i=1}^{n} x_i^2$
f_4	Root mean square (x_{rms})	$x_{\text{rms}} = \left(\frac{1}{n} \sum_{i=1}^{n} x_i^2 \right)^{1/2}$
f_5	Root amplitude (x_r)	$x_r = \left(\frac{1}{n} \sum_{i=1}^{n} \lvert x_i \rvert^{1/2} \right)^2$
f_6	Standard deviation (x_{std})	$x_{\text{std}} = \left(\frac{1}{n-1} \sum_{i=1}^{n} (x_i - \overline{x})^2 \right)^{1/2}$
f_7	Skewness (x_{ske})	$x_{\text{ske}} = \frac{\sum_{i=1}^{n} (x_i - \overline{x})^3}{(n-1)\, x_{\text{std}}^3}$
f_8	Kurtosis (x_{kur})	$x_{\text{kur}} = \frac{\sum_{i=1}^{n} (x_i - \overline{x})^4}{(n-1) x_{\text{std}}^4}$
f_9	Waveform factor (SF)	$\text{SF} = \frac{x_{\text{rms}}}{\overline{x}}$
f_{10}	Peak factor (CF)	$\text{CF} = \frac{x_p}{x_{\text{rms}}}$
f_{11}	Pulse factor (IF)	$\text{IF} = \frac{x_p}{\overline{x}}$
f_{12}	Margin factor (CIF)	$\text{CIF} = \frac{x_p}{x_r}$

x_i in the table is discrete time series signal.

3. Case Studies

3.1. Data Acquisition. Experiments were performed on the machinery fault simulator (MFS) from SpectraQuest, Inc., shown in Figure 2. It can simulate most of faults that commonly occur in rotating machinery, such as rotor body defects, bearing defects, and gearbox defects. The shaft rotating speed was obtained by a laser speedometer. Acceleration signals were collected using the Dewetron 16 channels data acquisition system and IMI 608A11 accelerometers.

In the vibration testing experiments for roller bearing fault diagnosis, the simulator is composed of a motor, a coupling, a testing roller bearing fitted on the left of the shaft near the motor, a working roller bearing on the other side, a bearing load, and a shaft. The MFS provides a rolling bearing fault kit consisting of one normal, one inner race defect, one outer race defect, one with ball defect, and one combination of defects for performing experiments and studying bearing fault diagnosis. The acquisition frequency rate is 10 kHz. The sensors layout is depicted schematically in Figure 2(a) that a total of 8 sensors from t_1 to t_8 are used.

In the vibration testing experiments for gear fault diagnosis, the drive from the motor transmits to the gearbox through bearing-rotor system and belt. The gearbox consists of a two-stage parallel shaft with rolling bearings, helical gears, and a magnetic brake. The simplified diagram of gearbox transmission is shown in Figure 3, where z_1 is the testing gear. The MFS provides a gear fault kit consisting of one normal, one chipped tooth, and one missing tooth for performing experiments and studying gear fault diagnosis. The acquisition frequency rate is 20 kHz. The sensors layout is depicted schematically in Figure 2(b) that a total of 8 sensors from s_1 to s_8 are used.

In the vibration testing experiments for rotor crack fault diagnosis, the rotor-bearing system is driven by the motor. In

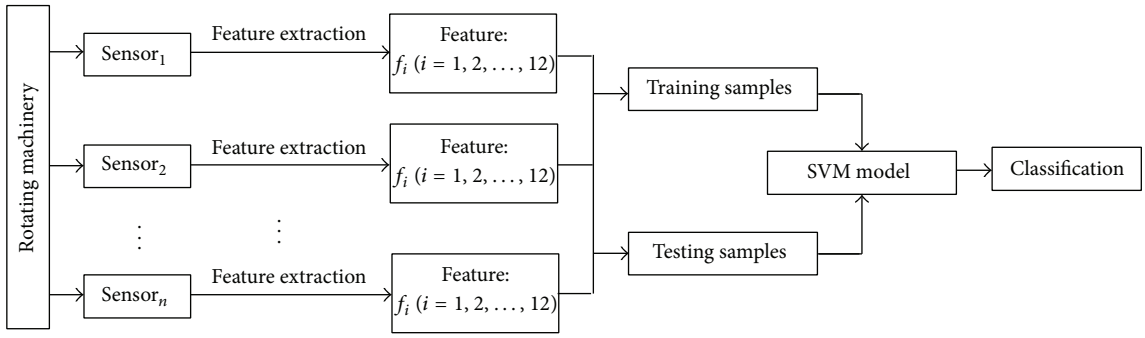

Figure 1: The multisensor information fusion process model.

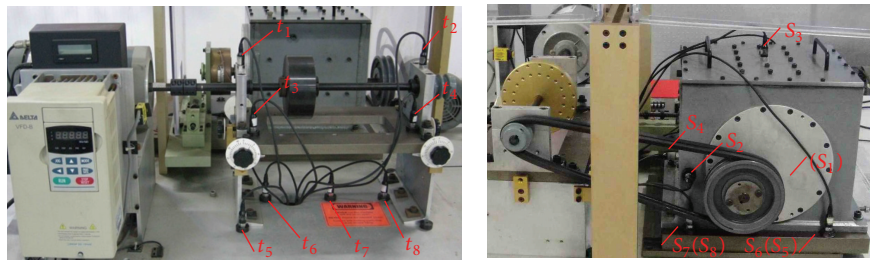

(a) The front view (b) The side view

Figure 2: The machinery fault simulator.

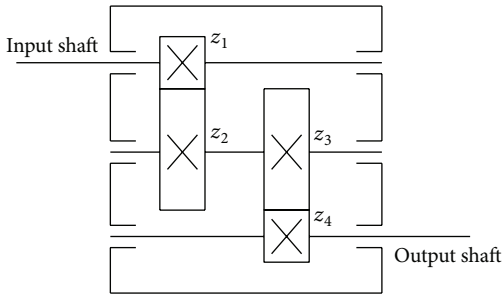

Figure 3: The simplified diagram of gearbox transmission.

order to simulate the expanding of crack, crack faults were introduced to the test rotor by using the electrodischarge machining. The defect with crack width of 0.12 mm and crack depth of 3 mm represents slight defect, and that with crack width of 0.12 mm and crack depth of 5 mm represents serious defect. The acquisition frequency rate is 10 kHz. The sensors layout is depicted schematically in Figure 2(a) that a total of 4 sensors from t_1 to t_4 are used.

3.2. Fault Diagnostic Case of Gear. Vibration signals of gear with three fault models including normal, chipped tooth, and missing tooth are taken for analysis. A certain time-domain feature is calculated from eight sensors (s_1 to s_8) to constitute an eight-dimensional vector as a fault sample. One hundred and ten fault samples from each model, a total of three hundred and thirty samples, are used to constitute the fault sample sets. Sixty fault samples from each model, a total of one hundred and eighty samples, are selected randomly as training samples and the others are used as testing samples. Twelve time-domain statistics are analyzed one by one.

LibSVM-mat-2.9 is chosen for SVM calculation. LibSVM is developed by Lin Chih-Jen from Taiwan [19]. It is a simple and easy-to-use SVMs tool for classification. RBF kernel function is chosen as kernel function shown as follows:

$$K\left(x_i, x_j\right) = \exp\left(-g\left\|x_i - x_j\right\|^2\right), \quad g > 0. \tag{7}$$

The cross-validation combination with network search method is used to search the best parameters: the error penalty C of SVM and g of RFB. One-against-one multiclassification is chosen for pattern recognition. The diagnostic results of gear by using different time-domain features are listed in Table 2.

It can be found from Table 2 that the highest diagnostic accuracy is 93.33% by using the peak factor as feature to constitute fusional vector for gear fault diagnosis. Sensitivity of the features can be indicated by diagnostic accuracy when using the same classifier SVM, so, the peak factor is the most sensitive feature in the twelve time-domain features for identifying gear defect, followed by the amplitude square, root amplitude, mean, root mean square, standard deviation, and peak. The diagnostic accuracy is all above 80% by using these features. The skewness, kurtosis, waveform factor, and margin factor are less sensitive comparatively. The diagnostic accuracy is all under 70% by using these features.

Table 2: Diagnostic results of gear by using different features for fusion.

Feature	The best parameter		Diagnostic accuracy (%)			
	C	g	Normal	Chipped tooth	Missing tooth	All testing samples
Mean	$2^{6.5}$	2^{15}	98	82	84	88.00
Peak	2^{1}	2^{8}	98	86	66	83.33
Amplitude square	2^{12}	2^{0}	98	82	88	89.33
Root mean square	2^{14}	2^{3}	98	78	86	87.33
Root amplitude	$2^{11.5}$	$2^{11.5}$	100	88	76	88.00
Standard deviation	$2^{7.5}$	$2^{9.5}$	98	78	86	87.33
Skewness	2^{8}	2^{-1}	98	30	58	62.00
Kurtosis	$2^{2.5}$	2^{-3}	94	68	40	67.33
Waveform factor	$2^{-1.5}$	2^{9}	92	42	30	55.33
Peak factor	$2^{0.5}$	2^{-1}	94	92	94	93.33
Pulse factor	$2^{-0.5}$	2^{-2}	96	64	60	73.33
Margin factor	2^{0}	2^{-3}	96	57	55	69.33

Table 3: Diagnostic results of gear by using different single sensors.

Sensor	The best parameter		Diagnostic accuracy (%)			
	C	g	Normal	Chipped tooth	Missing tooth	All testing samples
s_1	$2^{5.5}$	2^{8}	40	28	86	51.33
s_2	$2^{3.5}$	$2^{13.5}$	22	94	100	72.00
s_3	2^{1}	2^{4}	84	82	76	80.67
s_4	2^{3}	$2^{8.5}$	54	80	94	76.00
s_5	2^{15}	$2^{0.5}$	64	90	100	84.67
s_6	$2^{13.5}$	$2^{6.5}$	92	96	56	81.33
s_7	$2^{11.5}$	$2^{7.5}$	90	96	64	83.33
s_8	2^{15}	2^{4}	78	86	58	74.00

It also can be found from Table 2 that the accuracy of normal testing samples is all above 90% by using any feature. During the analysis, we also found that the samples of defect with chipped tooth and defect with missing tooth are easy to be misclassified with each other, but defect samples are seldom mistakenly regarded as normal samples, so it can be deduced that normal and defect gear are always easy to distinguish.

In order to compare with single sensor for gear fault diagnosis, take eight features from a single sensor to constitute an eight-dimensional vector as a fault sample. The eight features are the peak factor, amplitude square, root amplitude, mean, root mean square, standard deviation, peak, and pulse factor, which are the first eight sensitive features for identifying gear defect selected on the basis of the above analysis result. In order to avoid the orders of magnitude difference of different features, normalized eigenvector is processed before inputting SVM. In fact, during the proposed multisensors information analysis, the fault sample is constituted by the same feature from multisensors, so the orders of magnitude difference are nonexistent and normalized eigenvector is not needed. The sensors s_1 to s_8 are analyzed one by one. The diagnostic results of gear by using different single sensors are listed in Table 3.

Comparing with Tables 2 and 3, it can be found that there is higher diagnostic accuracy by using multisensors information fusion method than using single sensor method as a whole.

3.3. Fault Diagnostic Case of Rolling Bearing. Vibration signals of rolling bearing with four fault models including normal, inner race defect, outer race defect, and ball defect are taken for analysis. A certain time-domain feature is calculated from eight sensors (t_1 to t_8) to constitute an eight-dimensional vector as a fault sample. One hundred and ten fault samples from each model, a total of four hundred and forty samples, are used to constitute the fault sample sets. Fifty fault samples from each model, a total of two hundred samples, are selected randomly as training samples and the others are used as testing samples. Twelve time-domain statistics are analyzed one by one.

LibSVM-mat-2.9 is chosen for SVM calculation. Gaussian kernel function is chosen as kernel function. The cross-validation combination with network search method is used

Table 4: Diagnostic results of rolling bearing by using different features for fusion.

Feature	The best parameter		Diagnostic accuracy (%)				
	C	g	Normal	Inner race defect	Outer race defect	Ball defect	All testing samples
Mean	2^{-3}	2^{15}	100	100	100	100	100
Peak	2^{3}	2^{7}	94.29	94.29	100	100	97.14
Amplitude square	2^{-3}	2^{5}	100	100	100	100	100
Root mean square	$2^{4.5}$	2^{15}	100	100	100	100	100
Root amplitude	2^{-2}	2^{15}	100	100	100	100	100
Standard deviation	$2^{4.5}$	2^{15}	100	100	100	100	100
Skewness	2^{2}	2^{4}	65.71	84.29	62.86	80	73.21
Kurtosis	2^{6}	2^{-2}	90.00	72.86	82.86	97.14	85.71
Waveform factor	2^{2}	2^{9}	81.43	70.00	80.00	98.57	82.50
Peak factor	2^{3}	2^{-3}	64.29	64.29	78.57	95.71	75.71
Pulse factor	2^{2}	2^{-3}	71.43	64.29	81.43	95.71	78.21
Margin factor	2^{5}	$2^{-4.5}$	71.43	68.57	80	95.71	78.93

Table 5: Diagnostic results of rolling bearing by using different single sensors.

Sensor	The best parameter		Diagnostic accuracy (%)				
	C	g	Normal	Inner race defect	Outer race defect	Ball defect	All testing samples
t_1	$2^{14.5}$	$2^{-1.5}$	85.56	88.89	100	98.89	93.33
t_2	2^{11}	$2^{5.5}$	58.89	58.89	100	100	79.44
t_3	$2^{3.5}$	2^{4}	96.67	78.89	100	98.89	93.67
t_4	$2^{14.5}$	$2^{0.5}$	100	85.56	83.33	98.89	91.94
t_5	2^{2}	$2^{7.5}$	100	96.67	100	100	99.17
t_6	2^{2}	$2^{7.5}$	97.7	96.67	100	91.11	96.39
t_7	2^{11}	$2^{3.5}$	98.89	90	100	88.89	94.44
t_8	2^{10}	$2^{-1.5}$	61.11	51.11	53.33	87.78	63.33

to search the parameters C and g. One-against-one multiclassification is chosen for pattern recognition. The diagnostic results of rolling bearing by using different time-domain features are listed in Table 4.

It can be found from Table 4 that the mean, amplitude square, root mean square, root amplitude, and standard deviation are the first five sensitive features for identifying rolling bearing defect. The diagnostic accuracy is all 100% by using these features. Comparing with Tables 4 and 2, it can be found that there is a higher diagnostic accuracy for rolling bearing fault diagnosis than for gear fault diagnosis by using the proposed information fusion method as a whole. The main cause is that the way from the defect position of rolling bearing to the sensor installation position is shorter and simpler than the way from the defect position of gear.

In order to compare with single sensor for rolling bearing fault diagnosis, take eight features from a single sensor to constitute an eight-dimensional vector as a fault sample. The eight features are the mean, amplitude square, root mean square, root amplitude, standard deviation, peak, kurtosis, and waveform factor, which are the first eight sensitive features for identifying rolling bearing defect selected on the basis of the above analysis result. In order to avoid the orders of magnitude difference of different features, normalized eigenvector is processed before inputting SVM. The sensors t_1 to t_8 are analyzed one by one. The diagnostic results of rolling bearing by using different single sensor are listed in Table 5.

Comparing with Tables 4 and 5, it can be found that there is higher diagnostic accuracy by using multisensors information fusion method than using single sensor method as a whole.

3.4. Fault Diagnostic Case of Rotor Crack. Vibration signals of rotor crack with three fault models including normal, crack depth of 3 mm, and crack depth of 5 mm are taken for analysis. A certain time-domain feature is calculated from four sensors (t_1 to t_4) to constitute a four-dimensional vector as a fault sample. One hundred fault samples from each model, a total of three hundred samples, are used to constitute the fault sample sets. Fifty fault samples from each model, total of one hundred and fifty samples, are selected randomly as training samples and the others are used as testing samples. Twelve time-domain statistics are analyzed one by one.

LibSVM-mat-2.9 is chosen for SVM calculation. Gaussian kernel function is chosen as kernel function. The cross-validation combination with network search method is used to search the parameters C and g. One-against-one multiclassification is chosen for pattern recognition. The diagnostic

Table 6: Diagnostic results of rotor crack by using different features for fusion.

Feature	The best parameter		Diagnostic accuracy (%)			
	C	g	Normal	Crack depth of 3 mm	Crack depth of 5 mm	All testing samples
Mean	$2^{4.5}$	2^{12}	98	94	100	98.67
Peak	2^{0}	$2^{9.5}$	72	86	88	85.33
Amplitude square	2^{7}	2^{2}	100	96	94	96.67
Root mean square	2^{6}	2^{4}	100	98	100	99.67
Root amplitude	$2^{5.5}$	2^{3}	100	92	100	97.33
Standard deviation	2^{4}	2^{8}	98	96	98	98.67
Skewness	2^{5}	2^{-2}	58	44	46	58.00
Kurtosis	$2^{3.5}$	2^{-1}	44	74	84	71.00
Waveform factor	2^{2}	2^{3}	34	80	84	72.33
Peak factor	$2^{2.5}$	$2^{-1.5}$	42	46	62	69.33
Pulse factor	2^{-3}	2^{-1}	28	74	76	64.00
Margin factor	2^{1}	2^{-3}	32	72	74	64.67

results of gear by using different time-domain features are listed in Table 6.

It can be found from Table 5 that the mean, amplitude square, root mean square, root amplitude, and standard deviation are the first five sensitive features for identifying rotor crack defect. The diagnostic accuracy is all 90% by using these features. The result is similar to fault diagnostic case of rolling bearing.

4. Conclusion

In this paper, a feature-level information fusion methodology is proposed that all the features are calculated using vibration data in time domain to constitute fusional vector and the SVM is used for classification. Only a vibration testing system is needed for raw signal collected in this method, so the process is simpler. The effectiveness of the proposed methodology is tested with examples of gear, rolling bearing, and rotor crack fault diagnosis. Sensitivities of the twelve time-domain features are discussed in each case study. The analyzed results indicate that the peak factor is the most sensitive feature in the twelve time-domain features for identifying gear defect, but it is not very sensitive for identifying rolling bearing and rotor crack defect. The mean, amplitude square, root mean square, root amplitude, and standard deviation are all sensitive for identifying gear, rolling bearing, and rotor crack defect comparatively.

The features used and discussed in this paper are all in time domain; however, features in frequency domain also can be used for fault diagnosis of rotating machinery and the sensibilities of the features for identifying rolling bearing, gear, and rotor defect are also worth studying in the future.

Conflict of Interests

The authors declare that there is no conflict of interests regarding the publication of this paper.

Acknowledgments

This work is supported by the National Natural Science Foundation of China (51105138 and 51175169), the National High Technology Research and Development Program Items (2012AA041805), the Pre-research Project (813040302), the CEEUSRO special plan of Hunan province (2010XK6066), and the Aid Program for Science and Technology Innovative Research Team in Higher Educational Institutions of Hunan province.

References

[1] V. T. Tran and B.-S. Yang, "An intelligent condition-based maintenance platform for rotating machinery," *Expert Systems with Applications*, vol. 39, no. 3, pp. 2977–2988, 2012.

[2] K. P. Kumar, K. V. N. S. Rao, K. R. Krishna, and B. Theja, "Neural network based vibration analysis with novelty in data detection for a large steam turbine," *Shock and Vibration*, vol. 19, no. 1, pp. 25–35, 2012.

[3] L. L. Jiang, Y. L. Liu, X. J. Li, and S. Tang, "Using bispectral distribution as a feature for rotating machinery fault diagnosis," *Measurement*, vol. 44, no. 7, pp. 1284–1292, 2011.

[4] C. Z. Han, H. Y. Zhu, and Z. S. Duan, *Multi-Source Information Fusion*, Tsinghua University Press, Beijing, China, 2006.

[5] G. F. Bin, J. J. Gao, X. J. Li, and B. S. Dhillon, "Early fault diagnosis of rotating machinery based on wavelet packets—empirical mode decomposition feature extraction and neural network," *Mechanical Systems and Signal Processing*, vol. 27, no. 1, pp. 696–711, 2012.

[6] T. H. Loutas, D. Roulias, E. Pauly, and V. Kostopoulos, "The combined use of vibration, acoustic emission and oil debris on-line monitoring towards a more effective condition monitoring of rotating machinery," *Mechanical Systems and Signal Processing*, vol. 25, no. 4, pp. 1339–1352, 2011.

[7] G. Niu, T. Han, B.-S. Yang, and A. C. C. Tan, "Multi-agent decision fusion for motor fault diagnosis," *Mechanical Systems and Signal Processing*, vol. 21, no. 3, pp. 1285–1299, 2007.

[8] S. G. Barad, P. V. Ramaiah, R. K. Giridhar, and G. Krishnaiah, "Neural network approach for a combined performance and

mechanical health monitoring of a gas turbine engine," *Mechanical Systems and Signal Processing*, vol. 27, no. 1, pp. 729–742, 2012.

[9] Q. Tan and Y.-H. Xiang, "Application of weighted evidential theory and its information fusion method in fault diagnosis," *Journal of Vibration and Shock*, vol. 27, no. 4, pp. 112–116, 2008.

[10] Y.-Y. Liu, Y.-F. Ju, C.-D. Duan, and X.-F. Zhao, "Structure damage diagnosis using neural network and feature fusion," *Engineering Applications of Artificial Intelligence*, vol. 24, no. 1, pp. 87–92, 2011.

[11] O. Basir and X. Yuan, "Engine fault diagnosis based on multi-sensor information fusion using Dempster-Shafer evidence theory," *Information Fusion*, vol. 8, no. 4, pp. 379–386, 2007.

[12] G. Niu and B.-S. Yang, "Intelligent condition monitoring and prognostics system based on data-fusion strategy," *Expert Systems with Applications*, vol. 37, no. 12, pp. 8831–8840, 2010.

[13] A. Ghasemloonia and S. Esmaeel Zadeh Khadem, "Gear tooth failure detection by the resonance demodulation technique and the instantaneous power spectrum method—a comparative study," *Shock and Vibration*, vol. 18, no. 3, pp. 503–523, 2011.

[14] Z. S. Chen and Y. M. Yang, "Fault diagnostics of helicopter gearboxes based on multi-sensor mixtured hidden Markov models," *Journal of Vibration and Acoustics, Transactions of the ASME*, vol. 134, no. 3, Article ID 031010, 2012.

[15] A. Widodo and B.-S. Yang, "Support vector machine in machine condition monitoring and fault diagnosis," *Mechanical Systems and Signal Processing*, vol. 21, no. 6, pp. 2560–2574, 2007.

[16] B.-S. Yang, T. Han, and W.-W. Hwang, "Fault diagnosis of rotating machinery based on multi-class support vector machines," *Journal of Mechanical Science and Technology*, vol. 19, no. 3, pp. 846–859, 2005.

[17] J. Y. Yang, Y. Y. Zhu, Y. S. Zhang, and Q. Wang, "Intelligent fault diagnosis of rolling element bearing based on SVMS and statistical characteristics," in *Proceedings of the ASME International Conference on Manufacturing Science and Engineering*, pp. 525–536, Atlanta, Ga, USA, October 2007.

[18] C.-W. Hsu and C.-J. Lin, "A comparison of methods for multiclass support vector machines," *IEEE Transactions on Neural Networks*, vol. 13, no. 2, pp. 415–425, 2002.

[19] C. Hsu, C. C. Chang, and C. J. Lin, "A practical guide to support vector classification[EB/OL]," 2009, http://www.csie.ntu.edu.tw/~cjlin/.

Hindawi Publishing Corporation
Shock and Vibration
Volume 2014, Article ID 807489, 7 pages
http://dx.doi.org/10.1155/2014/807489

Research Article

Dynamic Study of a Capacitive MEMS Switch with Double Clamped-Clamped Microbeams

Hatem Samaali,[1] Fehmi Najar,[1] and Slim Choura[2]

[1] *Applied Mechanics and Systems Research Laboratory, Tunisia Polytechnic School, University of Carthage, BP 743, 2078 La Marsa, Tunisia*
[2] *Research Group on Intelligent Machines, National Engineering School of Sfax, University of Sfax, BP 1173, 3038 Sfax, Tunisia*

Correspondence should be addressed to Fehmi Najar; fehmi.najar@gmail.com

Received 5 July 2012; Accepted 2 November 2012; Published 27 March 2014

Academic Editor: Sami El-Borgi

We study a capacitive MEMS switch composed of two clamped-clamped exible microbeams. We first develop a mathematical model for the MEMS switch where the upper microbeam represents the ground transmission line and the lower one represents the central transmission line. An electrostatic force is applied between the two microbeams to yield the switch to its ON and OFF states. We derive the equations of motion of the system and associated boundary conditions and solve the static and dynamic problems using the differential quadratic method. We show that using only nine grid points gives relatively accurate results when compared to those obtained using FEM. We also examine the transient behavior of the microswitch and obtain results indicating that subsequent reduction in actuation voltage, switching time, and power consumption are expected along with relatively good RF performances. ANSYS HFSS simulator is used in this paper to extract the RF characteristics of the microswitch. HFSS simulation results show that the insertion loss is as low as −0.31 dB and that the return loss is better than −12.41 dB at 10 GHz in the ON state. At the OFF state, the isolation is lower than −23 dB in the range of 10 to 50 GHz.

1. Introduction

In telecommunication, MEMS devices offer a multitude of components to replace the classical semiconductor circuits elements. Microswitches and microresonators are used in a series of applications extending from the mobile phone and wireless networks to fiber-optic communication and multiplexed networks [1–3]. The major tasks of these devices are switching, filtering, and tuning. The equivalent circuit elements to these devices (PIN diode and Field-Effect Transistors FET) are generally characterized by high power consumption, low reliability, and high-manufacturing costs. In addition, they present unsatisfactory performance for high signal frequencies [4]; they give a high insertion loss and inadequate isolation at ON and OFF switching state.

Radio frequency MEMS (RF-MEMS) components have been recently widely developed and used in several applications. In particular, RF-MEMS microswitches are used in telecommunication applications to replace the traditional microelectronic switches (diodes and transistors). These microswitches present an improved insertion loss and good isolation during the "ON/OFF" switching states [4]. However, they are limited by the high actuation voltage (up to 30 volts) and slow switching time (nearly 300 microseconds). As a result, several researchers want to ameliorate the switching time, minimize the actuation voltage, and integrate RF-MEMS switches with IC [5]. To satisfy this integration, RF MEMS switches must satisfy the following conditions: (a) have very small size, (b) have low actuation voltage, and (c) present low power consumption.

Several mechanisms of actuation have been used to actuate RF-MEMS switches such as electromagnetic [6], electrostatic [7], thermal [8], and piezoelectric [9]. Due to its simplicity of integration, electrostatic actuation represents the most used actuation technique at the present time [10]. This is also due to its low power consumption, as well as small electrode size, in addition it is easy to be integrated with

IC circuits and it provides short switching time compared with the other mechanisms. However, it requires relatively high DC voltage, and thus, requires an additional CMOS integrated upconverter to raise the typical 5 V control voltage to the required level.

Electrostatically actuated structures present several nonlinearities and can become unstable. These nonlinearities are mainly due to the nature of the electrostatic force which is inversely proportional to the square of the distance between the two electrodes. A sudden collapse of the moving part can be observed at critical voltage (pull-in) of the microswitch achieving its ON or OFF state. In the literature the pull-in instability is classified into static and dynamic pull-in. Static pull-in occurs when the DC voltage exceeds a threshold value with maximum displacements varying from 33% to 41% of the original electrode gap distance. On the other hand, dynamic pull-in takes place when the system is excited using a combination of AC and DC voltages. In this case, the dynamic pull-in instability occurs before static pull-in [11, 12]. Nayfeh et al. [13] showed that dynamic pull-in occurs at voltages as low as 25% of the static pull-in voltage around the resonant frequency. Recently Khater et al. [14] validated experimentally this approach; they developed dynamic actuation methods based on frequency sweep to shunt a capacitive microswitch. The proposed technique lead to 60% reduction of the actuation voltage of the microswitch.

The decrease of actuation voltage of electrostatic RF-MEMS switches can be accomplished by (i) using different mechanical properties which reduce the microbeam rigidity, (ii) increasing the electrostatic surface, and/or (iii) decreasing the electrostatic gap. These variations degrade the principal parameters of the RF-MEMS switches, such as isolation. Abbaspour-Sani and Afrang proposed the decrease of the equivalent rigidity of the microswitch whose structure is composed of two displaceable microplates [15]; this preserves the microswitch parameters while increasing its lifetime. Similarly, Chaffey and Austin [16] decreased the equivalent rigidity of the microsystem and concluded that the use of a double cantilever microbeam structure, compared to a single microbeam structure, reduces significantly the pull-in voltage. Recently Samaali et al. [17] demonstrated that when we use a double cantilever microbeam to design an RF microswitch, a reduction of the pull-in voltage, the switching time and the power consumption are observed.

The present paper examines the static and dynamic behaviors of an electrostatically actuated capacitive contact RF microswitch. The proposed design consists of a pair of bridge microbeams with clamped ends. An electrostatic force is applied between the two microbeams (electrodes) causing their deflections and the collapse of the upper microbeam onto the lower one when the pull-in voltage is reached. We investigate the static and transient responses of the RF microswitch as we vary the applied DC voltage and study its ON-OFF cycle. The power requirement of the actuation cycle is also studied and compared with the classical single beam design.

2. Model Description and Reduced-Order Model

2.1. Problem Formulation. The schematic view of the capacitive microswitch is given in Figure 1. It consists of double suspended bridges that represent the ground and the central transmission lines. Both upper and lower beams are clamped at their ends to the substrate. A dielectric layer is used to separate the electrodes and prevent electrical short circuit. The microbeams are modeled using Euler-Bernoulli beam theory using the following nondimensional coupled-integral-partial-differential equations and their associated boundary conditions [18]:

$$\begin{aligned}
&\ddot{w}_i + c_i \dot{w}_i + w_i'''' \\
&\qquad = \left[F_i + \alpha_1 \int_0^1 \left(w_i\left(x_i, t\right)\right)^2 dx_i\right] w_i'' \\
&\qquad\quad + \alpha_2 \frac{V_{\mathrm{DC}}^2}{\left(1 - d_w\right)^2}, \quad i = 1, 2 \\
&w_i\left(0, t\right) = 0, \qquad w_i\left(1, t\right) = 0, \\
&w_i'\left(0, t\right) = 0, \qquad w_i'\left(1, t\right) = 0,
\end{aligned} \tag{1}$$

where $w_i(x_i, t)$ is the nondimensional deflection of each microbeam at the nondimensional time t and at nondimensional locations x_i and $d_w = w_1(x_1, t) + w_2(x_2, t)$. The dot denotes the derivative with respect to t and the prime derivatives with respect to x_i. c_i represents the beam's nondimensional damping related to the quality factor by $Q = \omega/c_i$, ω is the nondimensional natural frequency, F_i is the nondimensional axial force generated by residual stresses, V_{DC} is the DC voltage, and L is the length of both microbeams. The variables are nondimensionalized using the following form:

$$\begin{aligned}
&w_i = \frac{\widehat{w}_i}{d}, \qquad x_i = \frac{\widehat{x}_i}{L}, \qquad t = \frac{\widehat{t}}{\tau}, \qquad \alpha_1 = 6\left(\frac{d}{h}\right)^2, \\
&\alpha_2 = 6\left(\frac{\epsilon L^4}{E d^3 h^3}\right), \qquad F_i = \widehat{F}_i \frac{L^2}{EI}, \qquad \tau = \sqrt{\frac{L^4 \rho A}{E_f I}},
\end{aligned} \tag{2}$$

where the hats denote the corresponding dimensional quantities. Here ρ is the density, E is the modulus of elasticity, b, h, $A = bh$, and $I = bh^3/12$ are beam's width, thickness, cross-section area, and second moment of area, respectively. d is the initial gap distance between both microbeams and h_d is the dielectric layer thickness. The geometric and physical parameters of the microswitch are given in Table 1.

2.2. Discretization and Reduced-Order Model. DQM transforms a PDE into a set of ODEs describing the motion of a set of prespecified discrete points (a grid) corresponding to discrete values of the continuous space variable. This is accomplished by expressing, at each grid point, the derivative of the deflection function with respect to the space variable

Table 1: Geometric and physical parameters of the beam.

L	b	h	d	ρ	E	ε	h_d
510 μm	100 μm	1.5 μm	1.18 μm	2300 Kg/m^3	166 GPa	8.851 10^{-12} F/m	0.236 μm

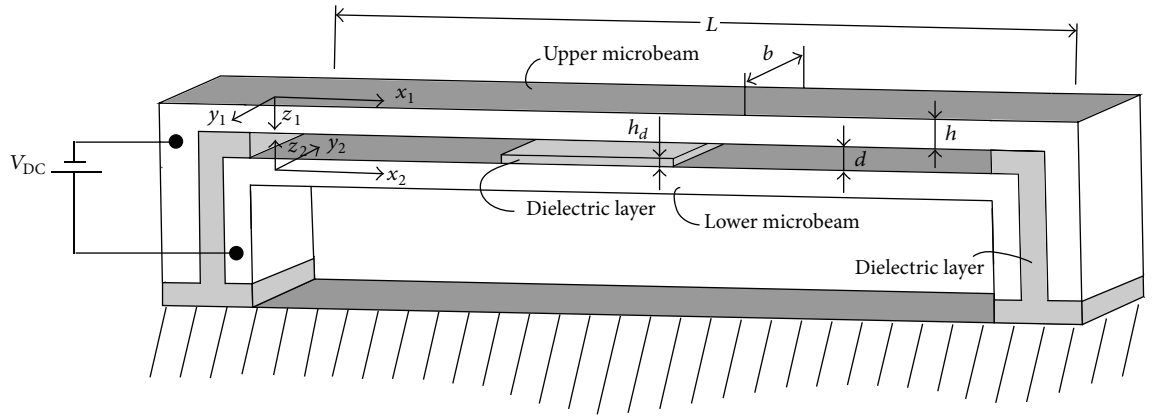

Figure 1: Capacitive contact RF-MEMS switch.

as a weighted linear sum of the values of this function at all n grid points [19]. That is,

$$\left[\frac{\partial f^r(x)}{\partial x^r}\right]_{x=x_i} = \sum_{j=1}^{n} A_{ij}^{(r)} f_j, \tag{3}$$

where $f_j = f(x_j)$, the x_j are the Chebyshev-Gauss-Lobatto grid points defined by [19] $x_i = (1/2)[1 - \cos((i-1)/(n-1))\pi]$, and $A_{ij}^{(r)}$ is the weighting coefficient of the rth-order derivative. These coefficients are determined using the Lagrange interpolation polynomials as test functions in (3). They are given by [20, 21]

$$A_{ij}^{(1)} = \left(\frac{\prod_{v=1;v\neq i}^{n}(x_i - x_v)}{(x_i - x_j)\prod_{v=1;v\neq j}^{n}(x_j - x_v)}\right), \quad i, j = 1, 2, \ldots, n, \quad j \neq i,$$

$$A_{ij}^{(r)} = r\left(A_{ii}^{r-1}A_{ij}^{1} - \frac{A_{ij}^{(r-1)}}{(x_i - x_j)}\right), \quad i, j = 1, 2, \ldots, n, \quad j \neq i, \tag{4}$$

$$A_{ii}^{(r)} = -\sum_{v=1;v\neq i}^{n} A_{iv}^{(r)}, \quad i = 1, 2, \ldots, n,$$

where $[A^{(r)}]$ is the matrix corresponding to the rth-order derivative. These matrices are *centrosymmetric* when r is even and *skew-centrosymmetric* when r is odd.

According to the previously published works [18, 22], the DQM is a suitable method to produce reduced-order models (ROM) in the case of clamped-clamped microbeam with nonlinear electrostatic force. We use n grid points to discretize the space and obtain a ROM given by the following $n - 3$ coupled second-order ordinary differential equations (ODEs) and associated boundary conditions, describing the motion of the microswitch:

$$\ddot{w}_{ik} + c_i\dot{w}_{ik} + \sum_{j=1}^{n} A_{jk}^{(4)} w_{ij} = \left[F_i - \alpha_1 \sum_{j=1}^{n}\sum_{l=1}^{n} C_j w_{ij} A_{jk}^{(2)} w_{il}\right] \times \sum_{j=1}^{n} A_{jk}^{(2)} w_{ij} + \alpha_2 \frac{V_{\mathrm{DC}}^2}{(1 - d_w)^2}, \quad k = 3, \ldots, \frac{n+1}{2}, \quad i = 1, 2,$$

$$w_{i1} = 0, \qquad w_{in} = 0, \qquad \sum_{j=1}^{n} A_{1j}^{(1)} w_{ij} = 0, \qquad \sum_{j=1}^{n} A_{nj}^{(1)} w_{ij} = 0, \tag{5}$$

where $d_w = w_{1k} + w_{2k}$, $w_{ik} = w_i(x_k, t)$. The associated static algebraic nonlinear system is solved using the Newton-Raphson in *Mathematica*. The transient analysis is obtained using Long Time Integration (LTI) obtained by the Runge-Kutta method.

3. Response of the Microswitch under DC Voltage

3.1. Static Response under DC Voltage. Figure 2 shows the variation of the static deflections at the center of the microbeams as the applied DC voltage is increased. Here due to symmetry of the problem only the deflection of one microbeam will be shown. The static response is obtained using the DQM (9 grid points) and validated with finite element (FE) analysis of the static responses obtained using

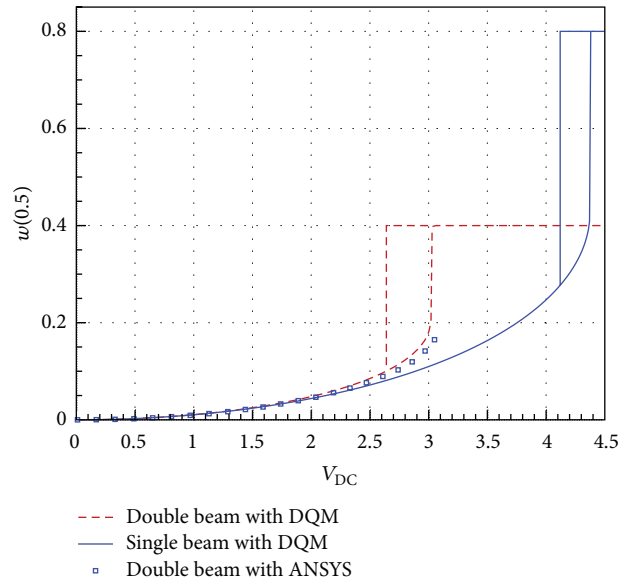

FIGURE 2: Microbeams deflection under an applied DC voltage and validation with ANSYS results.

the commercial software ANSYS. A comparison of the static response of the proposed system with a classical microswitch using one microbeam is shown in Figure 2. The computed static pull-in voltages associated with the single and double microbeams are 3.01 V and 4.38 V, respectively. Consequently for the static analysis a 32% reduction of the actuation voltage is observed. However, the pull-out voltage, also shown in Figure 2, requires more voltage reduction than the single beam case. In fact, the required voltage reduction is 0.37 V for the double beam case, while it requires only 0.26 V reduction for the single case to pull-out. This difference is due to the overall stiffness reduction of the system.

3.2. Transient Response under DC Voltage. The transient analysis of the microswitch under different applied DC voltages are shown in Figure 3. Long time integration is used here with the Runge-Kutta discretization technique to calculate the transient response of one of the two microbeams to a step DC voltage. In Figure 3 we show variation of the transient response as we vary the applied DC voltage. As shown the solution diverges as the applied voltage reaches 2.75 V and the microbeam pulls-in. Here we observe a difference between the *static pull-in* value (3.01 V) and the *transient pull-in* value (2.75 V), this mismatch is essentially due to the inertial effects of the microbeam, not taking into account the static analysis.

4. Pull-In Time and Power Requirement Using Transient Pull-In

Switching time and power consumption (switching power) are important parameters in RF MEMS Switches, and they constitute the main limitation for microswitches [23]. When the applied voltage increases the electrostatic force becomes higher than the elastic restoring force of the microbeam and the upper beam touches the lower beam causing pull-in. The time taken by the switch to pull-in is called the switching time or the pull-in time. Here in the proposed design each microbeam travels only 50% of the gap distance to reach the OFF state of the microswitch. Therefore, the switching time is shorter when compared to the single beam design.

The mean value of the electrostatic power P is defined by (6). This power corresponds to the mean value of the sum of instantaneous electrostatic power over the pull-in time T_s, given by the approximated parallel capacitances shown in Figure 4. The chosen capacitances are related to the selected DQM grid points to discretize the equation of motion. Equation (6) is then solved numerically at each time instant for the instantaneous power then integrated over the pull-in time period. C_k is the discretized capacitance for a given applied voltage.

$$P = \sum_{i=2}^{n-1} P_i = P_2 + \frac{1}{T_s} \sum_{k=3}^{n-2} \int_0^{T_s} C_i d V_{DC}^2 \, \dot{w}_k \, d\hat{t} + P_{n-1}, \tag{6}$$

where

$$P_2 = \frac{1}{2T_s} \int_0^{T_s} \frac{\varepsilon b L}{(1 - w_2)} (x_3 + x_2) V_{DC}^2 \dot{w}_2 \, d\hat{t},$$

$$P_{n-1} = \frac{1}{T_s} \int_0^{T_s} \frac{\varepsilon b L}{(1 - w_{n-1})} \left(x_n - \frac{x_{n-1} + x_{n-2}}{2} \right) V_{DC}^2 \dot{w}_{n-1} \, d\hat{t},$$

$$C_i = \frac{\varepsilon b L}{d(1 - w_i)} \left(\frac{x_{i+1} - x_{i-1}}{2} \right). \tag{7}$$

In Figure 5 we study the influence of the applied DC voltage on the pull-in time. In this figure, we show that this latter is reduced significantly by increasing the applied voltage in both single and double beam configurations. It is clear that using DC voltage to actuate the microswitch offers significantly improved performances for the double beam design.

We examine also the electrostatic power requirement of both designs. We note, in Figure 6, that the double beam switch requires lower actuated power when compared to the single beam design. Also we remark in Figure 6 that the minimum electrostatic power is obtained at 4.22 V for the single beam design and 2.92 V for the double beam design which is higher than the transient pull-in voltage in both cases. In Figure 7 we show the variation of the electrostatic power versus the pull-in time, as observed for the minimum used power in the single and double beam designs; almost the same transient pull-in time is obtained. However, the power used in this case is lower for the double beam designs.

5. Electromagnetic Model Analysis

In this section, we focus on the shunt capacitive MEMS switch behavior described above. The full wave electromagnetic simulation of the switch is done using Ansys HFSS. S-parameters are extracted in the frequency range going from 0.1 GHz to 50 GHz for different positions of the microswitch.

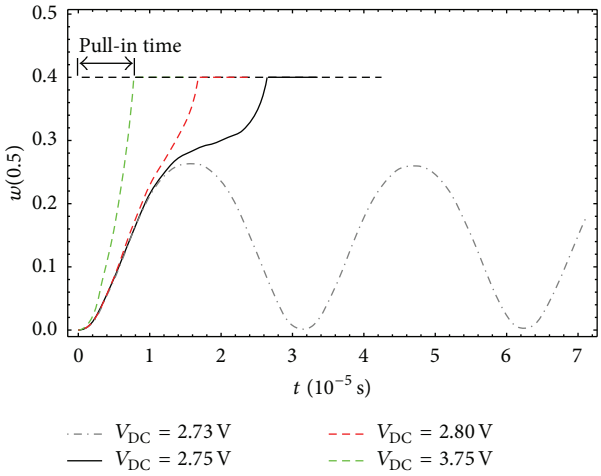

Figure 3: Transient response of the microswitch for different applied DC voltages.

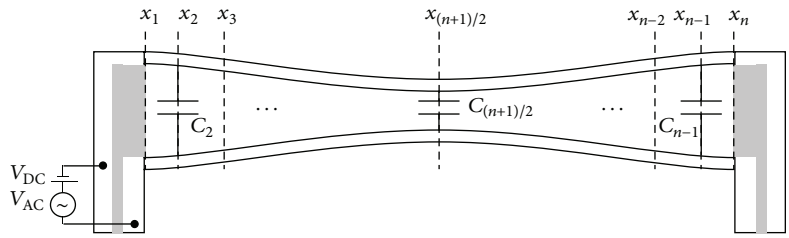

Figure 4: The equivalent parallel capacitances model of the capacitive microswitch.

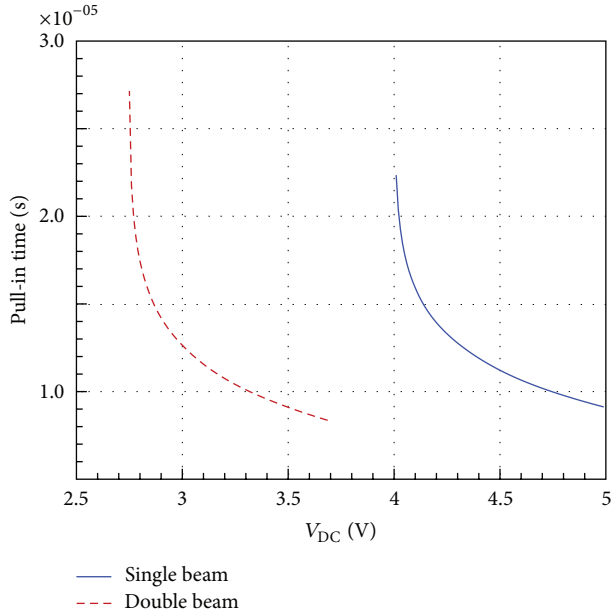

Figure 5: Influence of DC voltage on the pull-in time for simple and double beam microswitch designs.

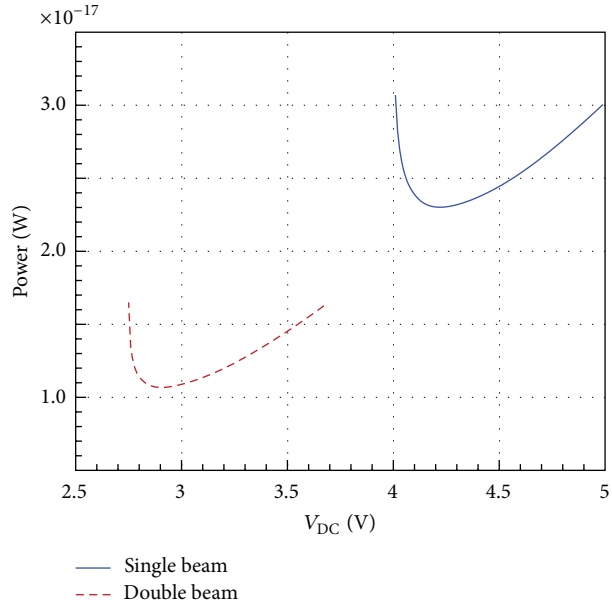

Figure 6: Influence of DC voltage on the electrostatic energy for simple and double beam microswitch designs.

In the simulation an air box size of 710 × 1000 × 900 μm is used and boundary radiation conditions are imposed on the four sides of the box, two waves ports are placed in the two other sides of the box. The wave ports are the boundary condition that permits energy to flow into and from the microswitch's structure.

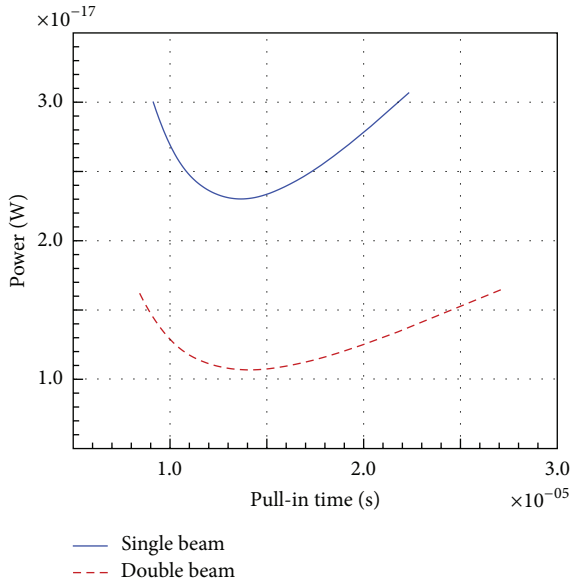

Figure 7: Variation of the electrostatic energy versus the pull-in time by varying the DC voltage for simple and double beam microswitch designs.

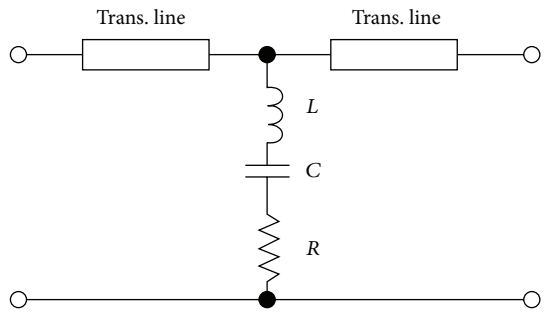

Figure 8: The equivalent circuit of the microswitch.

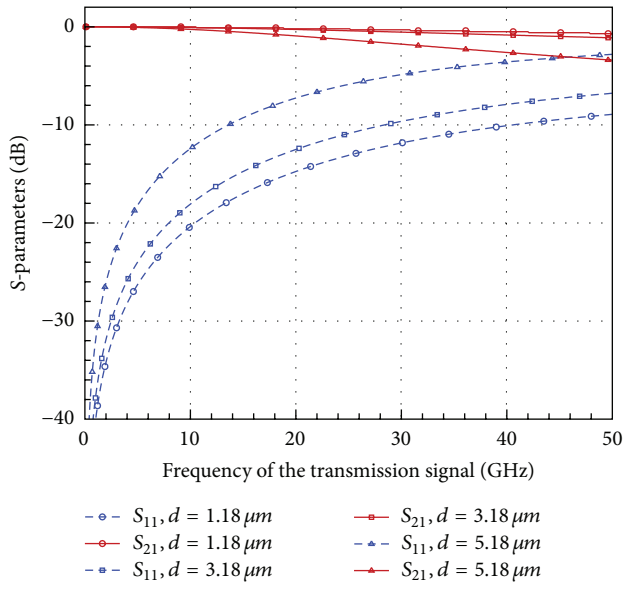

Figure 9: HFSS simulations results of the switch in ON state.

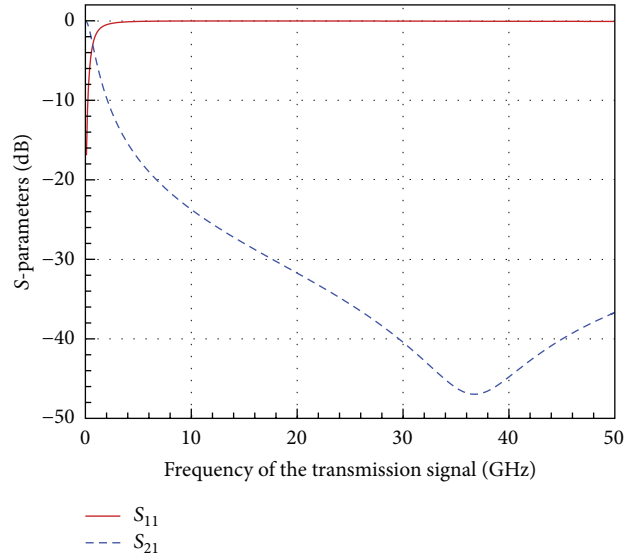

Figure 10: HFSS Simulation results of the switch in OFF state.

The used substrate has a relative dielectric constant correspondent to Silicon. The thickness of the substrate is 100 μm. The CPW conductors (ground and center transmission lines) are supposed to be perfect conductors. The central transmission line conductor of the CPW is assumed to be coated with silicon nitrate (Si_3 N_4) having relative dielectric constant of 7 and thickness of 0.236 μm. The microswitch is modeled by two short sections of transmission lines with characteristic impedance Z_0, and a lumped resistance-inductance-capacitance (RLC) model of the bridge with capacitance having an upstate or downstate value. The equivalent circuit of the switch is shown in Figure 8. In the upstate, the switch behaves as a capacitor when the frequency is below the inductance-capacitance (LC) series resonant frequency and as an inductor when the frequency is above the LC series resonant frequency, and at resonance, it reduces to pure resistance [24]. The transmission coefficients (S_{12} and S_{21}) are commonly called gain or attenuation, and the reflection coefficients (S_{11} and S_{22}) are directly related to impedance [25]. In the ON state the value of the coupling capacitance is very small due to the large separation between upper and lower beams. The S-parameters (S_{21} and S_{11}) were extracted in the range 0.1 to 50 GHz.

In Figure 9 the insertion loss (S_{21}) of the microswitch in the ON state is varied from −0.31 dB to −0.1 dB at 10 GHz with gap distance d varying from 1.18 to 5.18 μm. The return loss (S_{11}) varies from −12.41 to −20.36 dB at 10 GHz for the same range of the gap d. We conclude that as we increase the distance that separates upper and lower beams, we minimize the coupling capacitance and we increase and decrease, respectively, the return loss and the insertion loss. With a sufficient applied voltage, the ground transmission line and central transmission line of the microswitch deflect and create a large coupling capacitance; the microswitch is in the OFF state. The isolation (S_{21}) is lower than −23 dB in the range of 10 to 50 GHz, as shown in Figure 10.

6. Conclusion

We propose a design of a capacitive RF microswitch with two flexible microbeams. The new design allows a 32% reduction in the actuation voltage compared to a classical single beam design. A mathematical model was developed to analyze the static and transient behavior under different applied DC voltages. We observe that transient pull-in occurs before static pull-in at voltage as low as 8.6%. Then we studied and compared the switching times and switching power for both single and double beam designs under different DC actuations. We showed that the new double beam design gives significant improvement in switching time and power requirement. Finally, the Ansys HFSS simulator is used to extract the RF characteristics of the switch. Simulations results showed that an insertion loss of −0.31 dB and a return loss of −12.41 dB at 10 GHz for gap distance of 1.18 μm have been achieved in the ON state. These results can be ameliorated by increasing the gap distance. At the OFF state isolation lower than −23 dB in the range of 10 to 50 GHz is extracted by the Ansys HFSS simulator.

Conflict of Interests

The authors declare that there is no conflict of interests regarding the publication of this paper.

References

[1] J. J. Yao, "RF MEMS from a device perspective," *Journal of Micromechanics and Microengineering*, vol. 10, no. 4, pp. R9–R38, 2000.

[2] S. Lucyszyn, "Review of radio frequency microelectromechanical systems technology," *IEE Proceedings: Science, Measurement and Technology*, vol. 151, no. 2, pp. 93–103, 2004.

[3] J. A. Walker, "Future of MEMS in telecommunications networks," *Journal of Micromechanics and Microengineering*, vol. 10, no. 3, pp. R1–R7, 2000.

[4] G. M. Rebeiz, *RF MEMS: Theory, Design, and Technology*, Wiley-Interscience, Hoboken, NJ, USA, 2003.

[5] J. Y. Park, G. H. Kim, K. W. Chung, and J. U. Bu, "Monolithically integrated micromachined RF MEMS capacitive switches," *Sensors and Actuators A: Physical*, vol. 89, no. 1-2, pp. 88–94, 2001.

[6] J. A. Wrigth and Y. C. Tai, "Micro-miniature electromagnetic switches fabricated using MEMS technology," in *Proceeding of the 46th Annual International Relay Confrence (NARM '98)*, pp. 13-1–13-4, Oak Brook, Ill, USA, 1998.

[7] P. M. Zavracky, S. Majumder, and N. E. McGruer, "Micromechanical switches fabricated using nickel surface micromachining," *Journal of Microelectromechanical Systems*, vol. 6, no. 1, pp. 3–9, 1997.

[8] D. Girbau, A. Lazaro, and L. Pradell, "RF-MEMS switches based on the buckle-beam thermal actuator," in *Proceedings of the 3rd European Microwave Conference*, vol. 2, pp. 651–654, 2003.

[9] S. J. Gross, Q. Q. Zhang, S. Trolier-McKinstry, S. Tadigadapa, and T. N. Jackson, "RF-MEMS piezoelectric switch," in *Proceedings of the Device Research Conference*, pp. 99–100, 2003.

[10] H. Samaali, F. Najar, S. Choura, A. H. Nayfeh, and M. Masmoudi, "Novel design of MEMS ohmic RF switch with low voltage actuation," in *Proceedings of IEEE 3rd the International Conference on Signals, Circuits and Systems (SCS '09)*, Jerba, Tunisia, November 2009.

[11] R. K. Gupta, E. S. Hung, Y. J. Yang, G. K. Ananthasuresh, and S. D. Sentura, "Pullin dynamics of electrostatically actuated beams," in *Proceedings of the Technical DigestSolid State Sensor and Actuator Workshop*, pp. 1–2, 1996.

[12] G. N. Nielson and G. Barbastathis, "Dynamic pull-in of parallel-plate and torsional electrostatic MEMS actuators," *Journal of Microelectromechanical Systems*, vol. 15, no. 4, pp. 811–821, 2006.

[13] A. H. Nayfeh, M. I. Younis, and E. M. Abdel-Rahman, "Dynamic pull-in phenomenon in MEMS resonators," *Nonlinear Dynamics*, vol. 48, no. 1-2, pp. 153–163, 2007.

[14] M. E. Khater, K. Vummidi, E. M. Abdel-Rahman, A. H. Nayfeh, and S. Raman, "Dynamic actuation methods for capacitive MEMS shunt switches," *Journal of Micromechanics and Microengineering*, vol. 21, no. 3, Article ID 035009, 2011.

[15] E. Abbaspour-Sani and S. Afrang, "A low voltage MEMS structure for RF capacitive switches," *Progress in Electromagnetics Research*, vol. 65, pp. 157–167, 2006.

[16] J. Chaffey and M. Austin, "Analytical modelling of the electromechanical coupling of cantilever beams," in *Smart Structures, Devices, and Systems*, vol. 4935 of *Proceedings of SPIE*, pp. 86–93, 2002.

[17] H. Samaali, F. Najar, S. Choura, A. H. Nayfeh, and M. Masmoudi, "A double microbeam MEMS ohmic switch for RF-applications with low actuation voltage," *Nonlinear Dynamics*, vol. 63, no. 4, pp. 719–734, 2011.

[18] F. Najar, A. H. Nayfeh, E. M. Abdel-Rahman, S. Choura, and S. El-Borgi, "Nonlinear analysis of MEMS electrostatic microactuators: primary and secondary resonances of the first mode," *Journal of Vibration and Control*, vol. 16, no. 9, pp. 1321–1349, 2010.

[19] C. W. Bert and M. Malik, "Semianalytical differential quadrature solution for free vibration analysis of rectangular plates," *Journal of the American Institute of Aeronautics and Astronautics*, vol. 34, no. 3, pp. 601–606, 1996.

[20] C. W. Bert and M. Malik, "Free vibration analysis of tapered rectangular plates by differential quadrature method: a semi-analytical approach," *Journal of Sound and Vibration*, vol. 190, no. 1, pp. 41–63, 1996.

[21] S. Tomasiello, "Differential quadrature method: application to initial-boundary-value problems," *Journal of Sound and Vibration*, vol. 218, no. 4, pp. 573–585, 1998.

[22] F. Najar, S. Choura, S. El-Borgi, E. M. Abdel-Rahman, and A. H. Nayfeh, "Modeling and design of variable-geometry electrostatic microactuators," *Journal of Micromechanics and Microengineering*, vol. 15, no. 3, pp. 419–429, 2005.

[23] S. K. De and N. R. Aluru, "Full-Lagrangian schemes for dynamic analysis of electrostatic MEMS," *Journal of Microelectromechanical Systems*, vol. 13, no. 5, pp. 737–758, 2004.

[24] A. B. Yu, A. Q. Liu, Q. X. Zhang, A. Alphones, L. Zhu, and A. P. Shacklock, "Improvement of isolation for MEMS capacitive switch via membrane planarization," *Sensors and Actuators A: Physical*, vol. 119, no. 1, pp. 206–213, 2005.

[25] C.-L. Dai, H.-J. Peng, M.-C. Liu, C.-C. Wu, and L.-J. Yang, "Design and fabrication of RF MEMS switch by the CMOS process," *Tamkang Journal of Science and Engineering*, vol. 8, no. 3, pp. 197–202, 2005.

Hindawi Publishing Corporation
Shock and Vibration
Volume 2014, Article ID 409298, 8 pages
http://dx.doi.org/10.1155/2014/409298

Research Article

A New Criterion for the Stabilization Diagram Used with Stochastic Subspace Identification Methods: An Application to an Aircraft Skeleton

E. Mrabet,[1] M. Abdelghani,[2] and N. Ben Kahla[2]

[1] *High Institute of Technological Studies of Kairouan, Campus Universitaire Raccada, 3100 Kairouan, Tunisia*
[2] *High Institute of Applied Sciences and Technologies of Sousse, University of Sousse, Cité Taffala (Ibn Khaldoun), 4003 Sousse, Tunisia*

Correspondence should be addressed to N. Ben Kahla; nabil.benkahla@enig.rnu.tn

Received 5 July 2012; Accepted 20 November 2012; Published 17 March 2014

Academic Editor: Sami El-Borgi

The modal parameters of a structure that is estimated from ambient vibration measurements are always subject to bias and variance errors. Accordingly the concept of the stabilization diagram is introduced to help users identify the correct model. One of the most important problems using this diagram is the appearance of spurious modes that should be discriminated to simplify modes selections. This study presents a new stabilization criterion obtained through a novel numerical implementation of the stabilization diagram and the discussion of model validation employing the power spectral density. As an application, an aircraft skeleton is used.

1. Introduction

The vibration and acoustical behaviors of a mechanical structure are determined by its dynamic characteristics.

This dynamic behavior is typically described with a linear system model. The procedure for the estimation of modal parameters of structures from measured data can be split into three distinct steps [1]: data collection, system identification, and determination of modal parameters from the identified system description.

Stochastic identification methods for systems with unknown input have been introduced decades ago. Among the most robust and accurate system identification methods for output-only modal analysis of mechanical structures is the stochastic subspace identification method. Two types of implementation are available: the covariance-driven (SSI-cov) [2] implementation and the data-driven (SSI-data) [3] implementation. For the first one (SSI-cov), three methods can be implemented: the balanced realization (BR), the principal component (PC), and the canonical variate analysis (CVA).

For dynamic structures such as the aircraft skeleton studied in this paper, the major setback in applying system identification for large-scale structures is the selection of the model order and the corresponding system poles.

To address this problem, the concept of the "stabilization diagram" is introduced, overestimating the structure model order. Therefore, spurious modes are going to surface out and we have to discriminate them. For this matter, many stabilization criteria have been implemented. The most recent one was the modal transform norm [4]. In this paper, a new stabilization criterion is implemented and a validation method is discussed. The stochastic subspace identification method used is the balanced realization.

2. Stochastic State Space Models for Vibrating Structures

The finite element method [4] is one of the most common tools for modeling mechanical structures. In the case of a linear dynamical model, one has the following system of ordinary differential equations:

$$\begin{aligned} M\ddot{u} + D\dot{u} + Ku &= f(t), \\ Y(t) &= Lu(t), \end{aligned} \tag{1}$$

where $M, D, K \in \mathbf{R}^{n\times n}$, and L are the mass, damping, stiffness, and selection matrices, respectively; f is the stochastic vector of nodal forces; $u(t)$ is the vector of nodal displacement; Y is the sensors measurements vector; "n" is the number of degree of freedom. In the case of nonproportional damping, (1) is written into a continuous time state space model. The classical form of this model is

$$\begin{aligned} \dot{x}(t) &= A_c x(t) + B_c f(t), \\ y(t) &= C_c x(t), \end{aligned} \tag{2}$$

where $A_c = \begin{bmatrix} 0 & I \\ -M^{-1}K & -M^{-1}D \end{bmatrix}$, $B_c = \begin{bmatrix} 0 \\ M^{-1} \end{bmatrix}$, $C_c = [L \;\; 0]$ and $x(t) = \begin{pmatrix} u \\ \dot{u} \end{pmatrix}$.

The vector $x(t)$ is called the state of the structure; $y(t)$ is the measurements vector. The discrete time state model of the mechanical system is expressed as

$$\begin{aligned} x_{k+1} &= Ax_k + Bf_k, \\ y_k &= Cx_k, \end{aligned} \tag{3}$$

where $A = e^{A_c T}$, $B = (A-I)A_c^{-1}B_c$ and T is the time sampling. For simplicity, the model given by (3) can be also written, when the output vector is noised, as follows:

$$\begin{aligned} x_{k+1} &= Ax_k + w_k \\ y_k &= Cx_k + v_k, \end{aligned} \tag{4}$$

where A and C are, respectively, the state transition and the output matrices; x_k is the discrete state vector; y_k is the discrete measured output vector; w_k and v_k are, respectively, the process and measurement noises.

These stochastic terms are unknown but it is assumed that they have a discrete white noise nature with an expected value equal to zero and that they have covariance matrices equal to

$$E\left\{\begin{pmatrix} w_p \\ v_p \end{pmatrix}\begin{pmatrix} w_q \\ v_q \end{pmatrix}^T\right\} = \begin{pmatrix} Q & S \\ S^T & R \end{pmatrix}\delta_{pq}; \quad \forall p, q \in \mathbf{Z}, \tag{5}$$

where δ_{pq} denotes the Kronecker delta.

3. Identification of the System Matrices (A, C) and Balanced Realization Algorithm

The starting point of the identification of the system matrices is based on the covariance matrices of the measured structural responses time series y_k which are assumed to be realization of a stationary stochastic process. The covariance matrices are given by the following formula [2]:

$$R_m = E\left\{y_{k+m}y_k^T\right\}. \tag{6}$$

An estimate of the covariance matrices is given [2] as follows:

$$\widehat{R}_m = \frac{1}{N-m}\sum_{k=1}^{N-m}\left(y_{k+m}y_k^T\right) = CA^mG, \tag{7}$$

where N is the number of points of the time series, $G = E\{x_k y_k^T\}$, and superscript T means transpose. These covariance matrices can be organized in a Hankel matrix $\widehat{H}(p,q)$ that can be factorized as follows:

$$\widehat{H}(p,q) = \begin{bmatrix} C \\ CA \\ \vdots \\ CA^{p-1} \end{bmatrix} \cdot \begin{bmatrix} G & AG & A^2G & \cdots & A^{q-1}G \end{bmatrix}, \tag{8}$$

where p and q denote the number of rows and columns, respectively, of the Hankel matrix. The first bloc matrix is called the observability matrix $\widetilde{O}$; the second one is the controllability matrix $\widetilde{C}$. For all covariance-driven stochastic subspace identification, the estimation of A and C is based on the singular values decomposition of the Hankel matrix [5, 6].

For the balanced realization method, the decomposition gives

$$\begin{aligned} \widehat{H}(p,q) &= U \cdot S \cdot V^T = [U_1 \;\; U_2]\begin{bmatrix} S_1 & 0 \\ 0 & S_2 \end{bmatrix}\begin{bmatrix} V_1^T \\ V_2^T \end{bmatrix} \\ &\cong U_1 \cdot S_1 \cdot V_1^T = \left(U_1 \cdot S_1^{1/2}\right)\left(S_1^{1/2} \cdot V_1^T\right) = \widetilde{O} \cdot \widetilde{C}, \end{aligned} \tag{9}$$

where U, S, and V^T are the left singular vector, the singular values matrix, and the right singular vector, respectively; S_1 is the dominant singular bloc matrix $S_2 \prec\prec S_1$. Afterwards, the observability and controllability matrices can be written as the following formulas:

$$\widetilde{O} = \left(U_1 \cdot S_1^{1/2}\right), \qquad \widetilde{C} = \left(S_1^{1/2} \cdot V_1^T\right). \tag{10}$$

The system matrix C is immediately extracted from the observability matrix by taking the "r" first rows; "r" denotes the numbers of sensors used in the structure:

$$C = \widetilde{O}(1:r,:). \tag{11}$$

The system matrix A is extracted from the observability matrix as follows:

$$A = \left(\widetilde{O}_{\downarrow}\right)^{+}\left(\widetilde{O}_{\uparrow}\right), \tag{12}$$

where $\widetilde{O}_{\downarrow} = \left[C \;\; CA \;\; CA^2 \;\; \cdots \;\; CA^{q-2}\right]^T$, $\widetilde{O}_{\uparrow} = \left[CA \;\; CA^2 \;\; \cdots \;\; CA^{q-1}\right]^T$, and the superscript (+) means the generalized inverse.

The system matrix G is immediately extracted from the controllability matrix by taking the "r" first columns:

$$G = \widetilde{C}(:, 1:r). \tag{13}$$

4. Modal Analysis

With the assumption of low damping ratios and distinct eigenvalues, natural frequencies are obtained from A as follows:

$$f_p = \frac{1}{2\pi}\sqrt{\left(\frac{\ln\left(\left|\mu_p\right|\right)}{T}\right)^2 + \left(\frac{\arg(\mu_p)}{T}\right)^2}. \tag{14}$$

The damping ratios are also obtained from A as follows:

$$\xi_p = \frac{-\ln\left(\left|\mu_p\right|\right)}{\sqrt{\left(\ln\left(\left|\mu_p\right|\right)\right)^2 + \left(\arg(\mu_p)\right)^2}}. \quad (15)$$

From C, the modes shapes are expressed as

$$\phi_p = C\psi_p, \quad (16)$$

where μ_p and ψ_p are the eigenvalues and eigenvectors of A and $\arg(\cdot)$ denotes the phase angle.

5. The Stabilization Diagram

The SSI-cov, as it happens with the balanced realization method, does not yield exact values for the parameters but only estimates with uncertainties. The origins of these uncertainties [4] can be described from two points of view:

(i) *From the Operational/Experimental Point of View*: the number of data samples is finite, the input might not be white noise and real structure can't always be modeled into stationary linear system.

(ii) *From a Statistical Point of View*: uncertainties can be induced either by the bias of the model or by the bias of the mode and the variance of the mode.

These uncertainties are responsible for the appearance of spurious modes. One of the primary challenges related to modal analysis is to remove these spurious modes. For this purpose, the concept of stabilization diagram is introduced.

The stabilization diagram is a graphical tool used to help in the manual selection of the modes that are more likely to represent the structure physical modes. The quality of a stabilization diagram [2] depends on the algorithm used in the identification, on the values of the input parameters of the algorithm, and also on noise ratio of the time series under analysis. The basic idea is that several runs of the complete pole identification process are made, by using models of increasing order. The stabilization diagram has frequencies in the horizontal axis and orders on the vertical one. Physical poles should readily appear into alignments. However, not only physical modes will come into view in this diagram but also spurious modes. Most of spurious modes can be removed by using the so-called stabilization criteria. These criteria can be split into two types.

(i) *Preliminary Criteria*. The frequencies f_i and damping ξ_i ratios are expected to be obtained in certain ranges $f_{\min} \le f_i \le f_{\max}$ and $\xi_{\min} \le \xi_i \le \xi_{\max}$; all modes having frequencies f_i and damping ratios ξ_i out of these ranges will be discriminated. Only modes verifying these criteria are plotted in the stabilization diagram.

(ii) *Stabilization Criteria*. Modes, for which the differences in modal parameters between two consecutive model orders [4] are higher than certain threshold values, are not in the diagram.

In the classical implementation of the stabilization diagram, the typical stability criteria values [3] are as follows: $\varepsilon_f = 1\%$ for frequency, $\varepsilon_\xi = 5\%$ for damping, and the modal assurance criterion (MAC) $\mathrm{MAC}_\phi = 98\%$ for eigenvectors. Two modes identified in certain two orders, "i" and "$i+1$," will be plotted in the stabilization diagram if

$$\left|\frac{f_i - f_{i+1}}{f_i}\right| \le \varepsilon_f,$$

$$\left|\frac{\xi_i - \xi_{i+1}}{\xi_i}\right| \le \varepsilon_\xi, \quad (17)$$

$$\mathrm{MAC}\left(\phi_i, \phi_{i+1}\right) = \frac{\left|\phi_i^* \cdot \phi_{i+1}\right|^2}{\phi_i^* \cdot \phi_i \cdot \phi_{i+1}^* \cdot \phi_{i+1}} \ge \mathrm{MAC}_\phi,$$

where subscript $(*)$ denotes complex conjugate transpose.

This manner of plotting the stabilization diagram is not the only one. In [7], the authors present a new approach to establish the diagram. The method estimates model order in terms of component energy index (CEI); then the diagram is plotted in increasing Hankel matrix rows.

6. An Alternative Numerical Implementation for the Stabilization Diagram

When working with the stabilization diagram, the perfect situation is an utter disappearance of all spurious modes and only the alignments (corresponding to physical system modes) are plotted in the diagram. Using the classical numerical implementation and taking into account the bias and variance modes, if we minimize the thresholds values ε_f, ε_ξ, and $(1 - \mathrm{MAC}_\phi)$, most of the spurious modes will disappear; nonetheless, the diagram is likely to lose some alignments.

This present study suggests an alternative numerical implementation of the stabilization diagram that intends not to calculate the difference between consecutive modal order parameters but to compare every modal order parameter with all the other modal orders (see Figure 1).

For a certain model orders "m" and "n", $m \ne n$, having "p_m" and "p_n" identified modes, the criteria will be transformed for all $i \in \{1, \ldots, p_m\}$, $j \in \{1, \ldots, p_n\}$ as

$$\left|\frac{f_i - f_j}{f_i}\right| \le \varepsilon_f,$$

$$\left|\frac{\xi_i - \xi_j}{\xi_i}\right| \le \varepsilon_\xi, \quad (18)$$

$$\mathrm{MAC}\left(\phi_i, \phi_j\right) = \frac{\left|\phi_i^* \cdot \phi_j\right|^2}{\phi_i^* \cdot \phi_i \cdot \phi_j^* \cdot \phi_{j1}} \ge \mathrm{MAC}_\phi.$$

The basic idea behind this algorithm is that in the simulated cases when the output is not noised, if a mode appears into an order of the diagram, it should show up for all the following orders too.

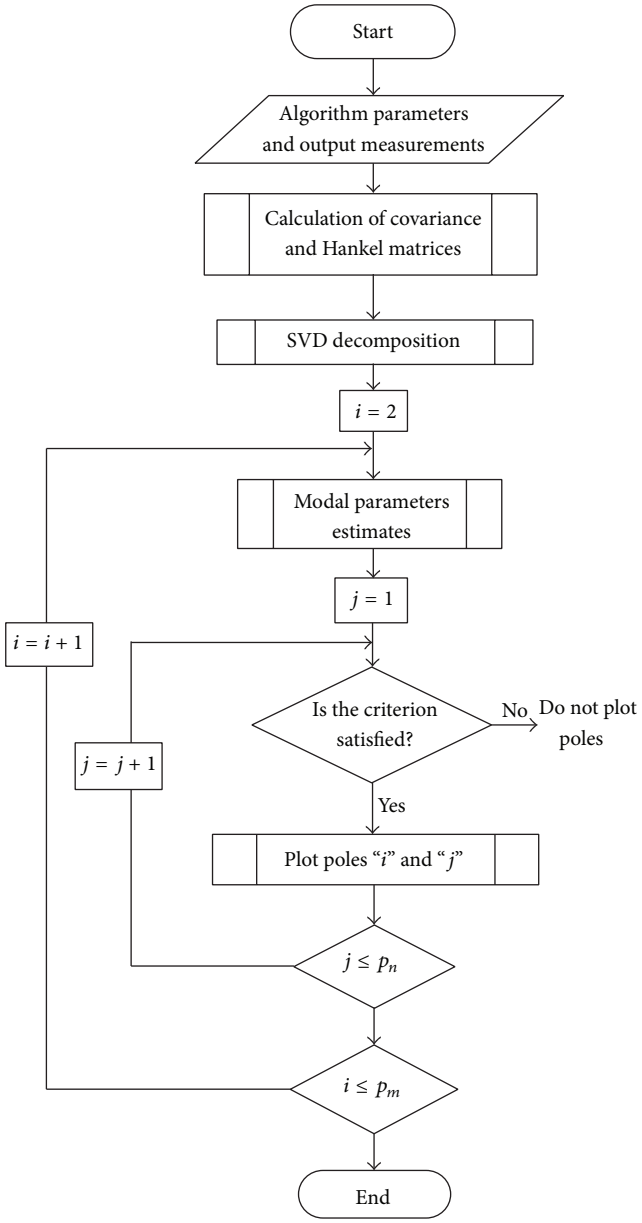

Figure 1: Flow chart, stabilization diagram implementation.

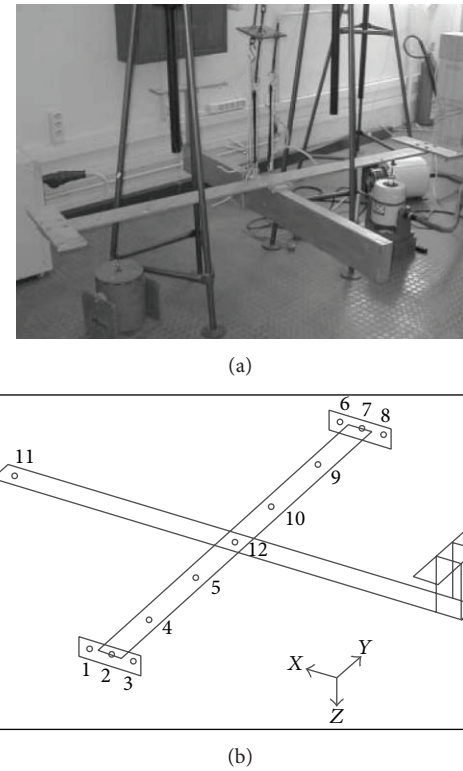

Figure 2: (a) The test rig; (b) the schema of the aircraft skeleton structure [8].

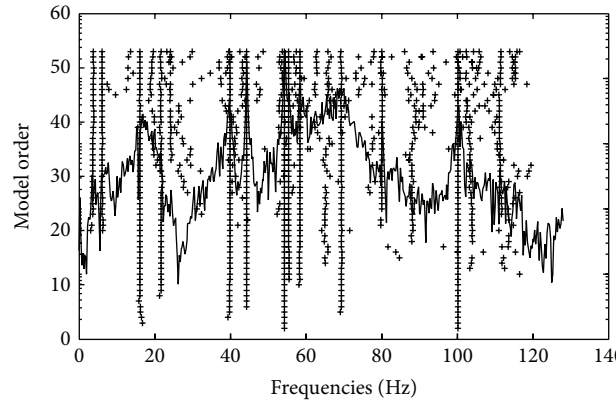

Figure 3: The aircraft stabilization diagram with only preliminaries criteria.

7. Application: The Aircraft Skeleton

To put this numerical implementation with the BR method into operation, an aircraft Skeleton is considered. The test rig and the model of the aircraft skeleton structure [8] are shown in Figure 2. The structure is excited by a white noise. Only seven sensors measurements and a sampling frequency f_s = 256 Hz are available for the identification.

Figure 3 shows the aircraft stabilization diagram with only preliminaries stabilization criteria. The diagram is plotted with frequencies and damping ranges (0, 120 Hz) and (0, 15%), respectively. The numbers of rows and columns of the Hankel matrix are $p = q = 25$, the maximal model order is taken as $O_{\max} = 53$, and the time lags used are $N_{\text{lag}} = 128$. In this diagram, 14 alignments are seen and seeming to be the physical system modes.

Figure 4 shows the stabilization diagram plotted with the following criteria: $\varepsilon_f = 1\%$ for frequencies, $\varepsilon_\xi = 5\%$ for damping, and $\text{MAC}_\phi = 98\%$ for eigenvectors. The diagram is plotted by using the classical numerical implementation. The inspection of this diagram shows that there is discrimination of several spurious modes, certain alignments are affected (frequencies close to 3 and 80 Hz), and the modes selections become difficult. Using the suggested numerical implementation with the same values for the criteria, the stabilization

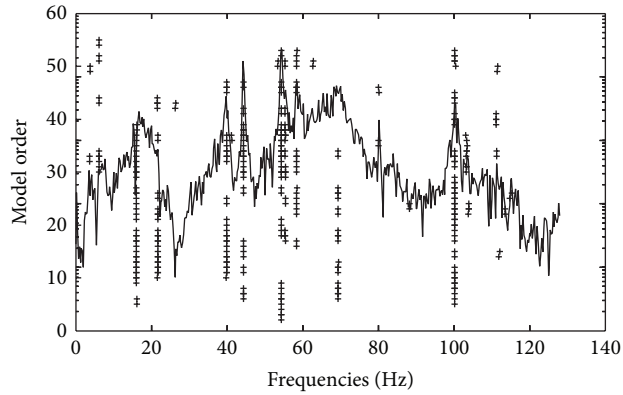

Figure 4: The aircraft stabilization diagram with classical implementation.

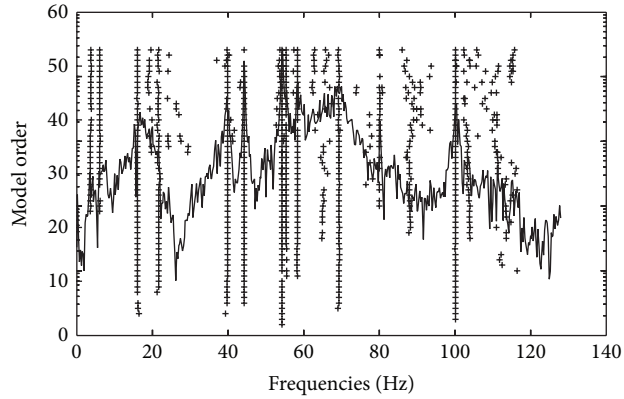

Figure 5: The stabilization diagram with new implementation.

diagram is shown in Figure 5. The alignments are already existent in spite of the fact that certain spurious modes are already there.

8. How to Improve the Stabilization Diagram Quality?

In order to make the stabilization diagram cleaner, a criterion is introduced in this study. It is based on the expression of the covariance matrix $R_m = CA^mG$ that can be written in the identified base as follows:

$$R_m = CA^mG = (C\Psi)\,\Lambda^m\left(\Psi^{-1}G\right) = \Phi\Lambda^m\widetilde{G} = \begin{bmatrix}\Phi_1 & \overline{\Phi_1}\end{bmatrix}\begin{bmatrix}\Lambda_1 & 0\\ 0 & \overline{\Lambda_1}\end{bmatrix}\begin{bmatrix}G_1^T\\ \overline{G_1}^T\end{bmatrix}, \tag{19}$$

where $C\Psi = \Phi$ are the modes shapes expressed in the identified base and $\Psi^{-1}G = \widetilde{G}$ is the covariance matrix between the state and the system output expressed also in the same base; it takes the form

$$\widetilde{G} = \begin{bmatrix}G_1^T\\ \overline{G_1}^T\end{bmatrix} = \begin{bmatrix}g_1^T & g_2^T & \cdots & g_n^T & \overline{g}_1^T & \overline{g}_2^T & \cdots & \overline{g}_n^T\end{bmatrix}^T. \tag{20}$$

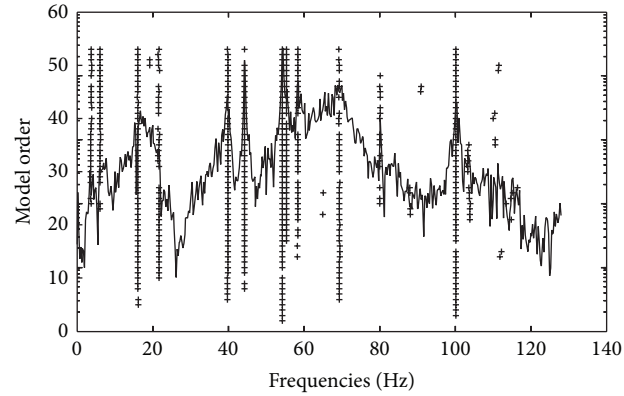

Figure 6: The stabilization diagram with the new stabilization criterion.

The stabilization criteria described up to now are derived from the vectors Φ if the MAC_Φ is used and from the eigenvalue matrix Λ if frequencies and damping criteria are employed.

The new criterion is based on the calculation of the MAC (modal assurance criterion) between two identified covariance vectors (g_i, g_j):

$$\frac{\left|g_i^* \cdot g_j\right|^2}{g_i{}^* \cdot g_i \cdot g_j^* \cdot g_j} \leq 1 - \mathrm{MAC}_g. \tag{21}$$

For all $i \in \{1, \ldots, p_m\}$, $j \in \{1, \ldots, p_n\}$, these covariance vectors g should be the same, at least theoretically, for every identified mode onto an alignment in the stabilization diagram. For the aircraft diagram shown in Figure 6, the criteria were $\varepsilon_f = 1\%$, $\varepsilon_\xi = 3\%$, $\mathrm{MAC}_\phi = 99\%$, and $\mathrm{MAC}_g = 99.95\%$.

In Figure 6, it is clear that 12 alignments are already stable in spite of the fact that the criteria are considered severe and most of the spurious modes have been discriminated. The structure has likely 12 vibration modes.

9. Balanced Realization (BR) Results and Comparison with Other Stochastic Subspace Identification Algorithms

For the model order 24, stable modes, belonging to alignments, are taken and the identification is presented in Table 1. In order to validate this system identification, the balanced realization results are compared with others obtained by two different algorithms implemented into a commercial modal analysis software, the ARTeMIS Extractor pro 2009 [9]. The algorithms are the canonical variate analysis (CVA) and the unweighted principal component (UPC), which are two data-SSI methods. Table 1 shows that both BR and CVA methods present the same identified parameters. Among the 12 modes identified by these two algorithms, 9 are also identified in frequencies by the UPC method in which 7 are also identified in damping.

Table 1: The identified frequencies and damping using several algorithms.

Modes	Frequencies: f (Hz)			Damping: ξ (%)			BR/UPC (%)		BR/CVA (%)	
	BR	CVA	UPC	BR	CVA	UPC	f	ξ	f	ξ
1	**3.71**	3.69	* * *	**4.90**	6.57	* * *	* * *	* * *	0.54	34.08
2	**6.13**	6.18	* * *	**3.60**	3.17	* * *	* * *	* * *	0.82	11.94
3	**16.06**	16.02	16.07	**4.05**	4.07	3.94	0.06	2.54	0.25	0.49
4	**21.71**	21.77	* * *	**5.73**	5.40	* * *	* * *	* * *	0.28	5.76
5	**39.87**	39.87	39.86	**0.38**	0.38	0.40	0.02	5.26	0.00	0.00
6	**44.33**	44.34	44.37	**0.03**	0.02	0.06	0.09	106.66	0.02	33.33
7	**54.35**	54.36	54.37	**0.11**	0.10	0.09	0.03	16.36	0.02	9.09
8	**55.42**	55.42	55.39	**0.22**	0.20	0.31	0.05	40.90	0.00	9.09
9	**58.44**	58.47	58.49	**0.38**	0.39	0.47	0.08	23.68	0.05	2.63
10	* * *	* * *	63.83	* * *	* * *	3.93	* * *	* * *	* * *	* * *
11	**69.41**	69.37	69.42	**1.12**	1.18	1.25	0.01	11.60	0.06	5.36
12	**80.06**	80.15	79.8	**0.09**	0.09	0.72	0.32	700	0.11	0.00
13	* * *	* * *	86.18	* * *	* * *	3.00	* * *	* * *	* * *	* * *
14	**100.25**	100.3	100.3	**0.11**	0.11	0.12	0.04	9.09	0.05	0.00
15	* * *	* * *	107.6	* * *	* * *	4.51	* * *	* * *	* * *	* * *
16	* * *	* * *	114.5	* * *	* * *	1.63	* * *	* * *	* * *	* * *

* * * Unidentified mode.

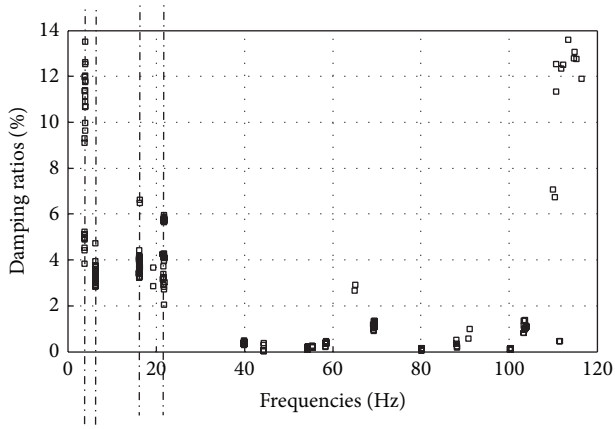

Figure 7: Repartition of damping ratios.

These differences between the first two algorithms and the third are understood given the fact that all of them can generate uncertainties. Moreover, it is known that the identification of the damping ratio is difficult even in simulated cases.

Figure 7 shows the repartition of the damping ratios corresponding to the stabilization diagram of Figure 6 and the dashed lines represent the first four identified modes. The inspection of Figure 7 shows that the damping identification presents a large dispersion along the model order range, mainly, for the first identified mode (3.71 Hz), in which the damping ratio varies between, about, 4% and 14% which is considered as large dispersion. These facts justify the relative damping error (BR/CVA) for the first mode (34.08%) which is considered as acceptable.

Consequently, the results comparison of the BR algorithm identification with the others confirms that our results are satisfactory.

10. Spectral Analysis

10.1. Expression of the Power Spectral Densities Matrix. Once a state space is identified, it is possible to compute the power spectral densities $G(z)$ which are written into the identified base for $z = \exp(j\omega T)$ as follows:

$$G(z) = \sum_{-\infty}^{+\infty} R_i z^{-i} = \frac{1}{2}\Phi g + \Phi(zI - \Lambda)^{-1}\Lambda g + \left(\frac{1}{2}\Phi g + \Phi\left(\frac{1}{z}I - \Lambda\right)^{-1}\Lambda g\right)^{T}. \tag{22}$$

Proof. Consider

$$G(z) = \sum_{-\infty}^{+\infty} R_i z^{-i} = \sum_{-\infty}^{0} R_i z^{-i} + \sum_{0}^{+\infty} R_i z^{-i} = \left(\frac{1}{2}R_0 + \sum_{-\infty}^{1} R_i z^{-i}\right) + \left(\frac{1}{2}R_0 + \sum_{1}^{+\infty} R_i z^{-i}\right). \tag{23}$$

Let the half PSD $G_+(z) = ((1/2)R_0 + \sum_{-\infty}^{1} R_i z^{-i})$, $G(z) = G_+(z) + (G_+(1/z))^T$;

$$\sum_{1}^{+\infty} R_i z^{-i} = \sum_{1}^{+\infty} C \cdot A^i \cdot G \cdot z^{-i} = C\left\{\sum_{1}^{+\infty} \frac{A^{i-1}}{z^{i-1}} z^{-1}\right\} A \cdot G = C\left\{\sum_{1}^{+\infty} \left(\frac{A}{z}\right)^{i-1}\right\} z^{-1} \cdot A \cdot G. \tag{24}$$

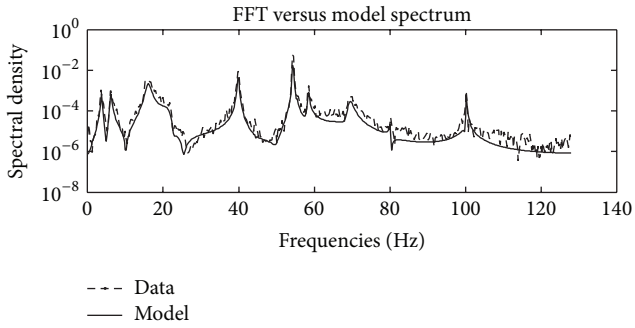

Figure 8: Cross spectrum between sensors 3 and 4.

The matrix A is stochastic, so for all eigenvalue, $|\lambda| \leq 1$; therefore, we have

$$\sum_{1}^{+\infty}\left(\frac{A}{z}\right)^{i-1} = \left(I - \left(\frac{A}{z}\right)\right)^{-1},$$
$$G_{+}(z) = \frac{1}{2}R_0 + C(zI - A)^{-1} \cdot A \cdot G. \tag{25}$$

Finally, after substitution of the expression of the matrices into the identified base, we have

$$G_{+}(z) = \frac{1}{2}\Phi g + \Phi(zI - \Lambda)^{-1}\Lambda g. \tag{26}$$

□

10.2. The Positive Real Sequences Conditions. A sequence R_i cannot be always considered as a valid output covariance sequence [3]. The sequence has to satisfy the positive real sequence condition. The following statements are equivalent:

(i) R_i is a positive real sequence.

(ii) The double infinite matrix L_∞ is positive definite:

$$L_\infty = \begin{pmatrix} R_0 & R_{-1} & R_{-2} & \cdots \\ R_1 & R_0 & R_{-1} & \cdots \\ R_2 & R_1 & R_0 & \cdots \\ \cdots & \cdots & \cdots & \ddots \end{pmatrix} \succ 0. \tag{27}$$

(iii) The power spectral densities $G(z)$ are positive definite matrix for all $z = \exp(j\omega T)$:

$$G(z) = \left(\frac{1}{2}\Phi g + \Phi(zI - \Lambda)^{-1}\Lambda g\right) + \left(\frac{1}{2}\Phi g + \Phi\left(\frac{1}{z}I - \Lambda\right)^{-1}\Lambda g\right)^{T} \succ 0. \tag{28}$$

11. Validation of the Identification by Spectral Analysis

A second procedure to validate the system identification is the spectral analysis. Four spectra are presented in Figures 8, 9, 10, and 11. They are compared with those obtained by applying FFT to measurements.

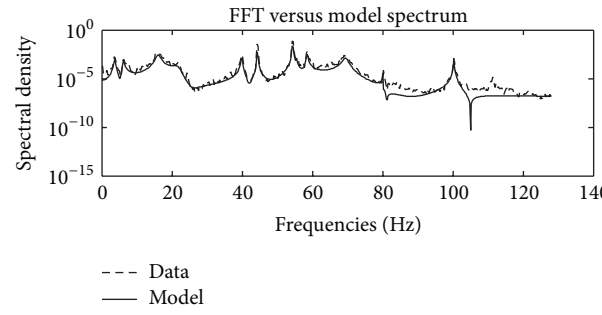

Figure 9: Autospectrum sensor 5.

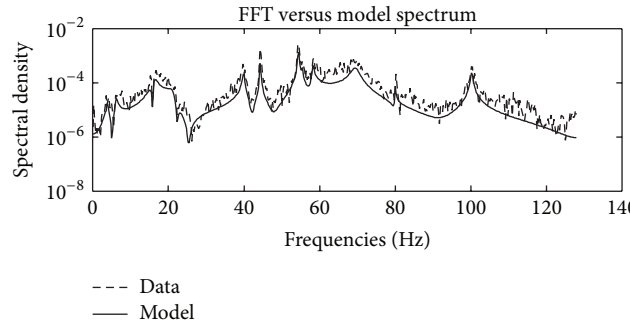

Figure 10: Cross spectrum between sensors 1 and 5.

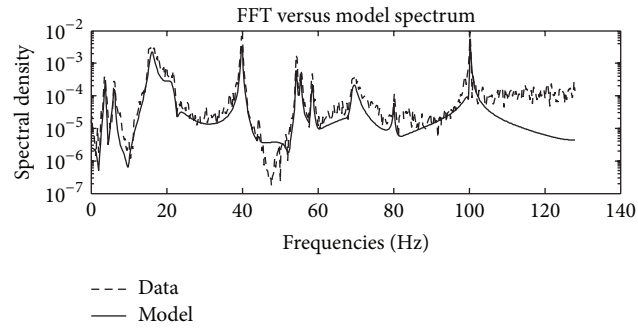

Figure 11: Cross spectrum between sensors 3 and 7.

From these comparisons, it is clear that the structure model parameters are well identified because the model and data spectra fit in spite of the divergence in the autospectrum of sensor 5 and the cross spectrum between sensors 3 and 7. Figures 8 and 10 show that both peaks and valleys are well superposed which implies a perfect identification of the model. The inspection of Figure 9 shows that all peaks and valleys are well superposed except the valley close to the Nyquist frequency (120 Hz). The same remark can be done for Figure 11 where model and data peaks are well superposed but not all the valleys over the frequencies range. In effect, model valleys on the frequencies range [40 Hz, 55 Hz] and close to the Nyquist frequency do not fit the data spectrum valley.

From these facts, we can conclude that peaks in all data and model spectra are better identified than the valleys. This can be understood from the implementation of the SSI-cov method that does not guarantee the positive real sequence

condition [3], in case, the inequality (28). Therefore, the extended covariance matrices [10] might not be positive. Thus, the spectrum divergences are well justified.

12. Conclusions

A new stabilization criterion associated with a new numerical implementation of the stabilization diagram has been presented using the BR (SSI-cov) method.

The new stabilization implementation makes the alignments in the diagram more robust and only spurious modes were removed. However, some other spurious modes are not removed and modes selection is still difficult. To remedy to this fact, the new stabilization criterion, based on the calculation of the modal assurance criterion (MAC) between the identified covariance vectors, was associated with the new numerical implementation. The obtained diagram is cleaner, most of the spurious modes were removed, and only alignments corresponding to physical modes are already there; then the modes selections are easier.

The validation by comparison with other results derived through the CVA and UPC algorithms gave satisfactory results in spite of some large errors in the damping identification. This fact has been justified in the previous section and we can conclude that the BR algorithm was a robust identification method when used with the new numerical implementation associated with the new criterion.

The validation by spectral analysis also confirms the quality of the model identification and the divergences into some spectra have been well justified.

Conflict of Interests

The authors declare that there is no conflict of interests regarding the publication of this paper.

Acknowledgment

The authors are grateful to S. D. Fassois of the Stochastic Mechanical Systems (SMS) Group of the University of Patras (Greece) for providing the experimental measurements.

References

[1] E. Reynders and G. D. Roeck, "Reference-based combined deterministic-stochastic subspace identification for experimental and operational modal analysis," *Mechanical Systems and Signal Processing*, vol. 22, no. 3, pp. 617–637, 2008.

[2] F. Magalhães, Á. Cunha, and E. Caetano, "Online automatic identification of the modal parameters of a long span arch bridge," *Mechanical Systems and Signal Processing*, vol. 23, no. 2, pp. 316–329, 2009.

[3] P. Van Overschee and B. De Moor, *Subspace Identification for Linear Systems: Theory, Implementation and Applications*, Kluwer Academic Publishers, 1996.

[4] E. Reynders, R. Pintelon, and G. De Roeck, "Uncertainty bounds on modal parameters obtained from stochastic subspace identification," *Mechanical Systems and Signal Processing*, vol. 22, no. 4, pp. 948–969, 2008.

[5] F. Magalhães, E. Caetano, and Á. Cunha, "Operational modal analysis and finite element model correlation of the Braga Stadium suspended roof," *Engineering Structures*, vol. 30, no. 6, pp. 1688–1698, 2008.

[6] D. Montalvão, N. M. M. Maia, and A. M. R. Ribeiro, "A review of vibration-based structural health monitoring with special emphasis on composite materials," *Shock and Vibration Digest*, vol. 38, no. 4, pp. 295–324, 2006.

[7] Y. Zhang, Z. Zhang, X. Xu, and H. Hua, "Modal parameter identification using response data only," *Journal of Sound and Vibration*, vol. 282, no. 1-2, pp. 367–380, 2005.

[8] V. Papakos and S. D. Fassois, "Multichannel identification of aircraft skeleton structures under unobservable excitation: a vector AR/ARMA framework," *Mechanical Systems and Signal Processing*, vol. 17, no. 6, pp. 1271–1290, 2003.

[9] ARTeMIS, "ARTeMIS Extractor pro 2009. s.l.," Denmark, SVIBS, 2009, http://www.svibs.com/.

[10] A. Lindquist and G. Picci, "Canonical correlation analysis, approximate covariance extension, and identification of stationary time series," *Automatica*, vol. 32, no. 5, pp. 709–733, 1996.